Lifetime Investigation of PEM Electrolyzers under Realistic Load Profiles

Frensch, Steffen Henrik

DOI (link to publication from Publisher):
10.54337/aau300037423

Publication date:
2018

Document Version
Publisher's PDF, also known as Version of record

LIFETIME INVESTIGATION OF PEM ELECTROLYZERS UNDER REALISTIC LOAD PROFILES

BY
STEFFEN FRENSCH

DISSERTATION SUBMITTED 2018

AALBORG UNIVERSITY
DENMARK

Lifetime Investigation of PEM Electrolyzers under Realistic Load Profiles

Ph.D. Dissertation
Steffen Frensch

Dissertation submitted November, 2018

Dissertation submitted: 08. November 2018

PhD supervisors: Prof. Søren Knudsen Kær
Aalborg Universitet

Assoc. Prof. Samuel Simon Araya
Aalborg Universitet

PhD committee: Associate Professor Thomas Condra (chairman)
Aalborg University

PhD Marcelo Carmo
Forschungszentrum Juelich

Professor Jens Oluf Jensen
Technical University of Denmark

PhD Series: Faculty of Engineering and Science, Aalborg University

Department: Department of Energy Technology

ISSN (online): 2446-1636
ISBN (online): 978-87-7210-354-9

Published by:
Aalborg University Press
Langagervej 2
DK – 9220 Aalborg Ø
Phone: +45 99407140
aauf@forlag.aau.dk
forlag.aau.dk

Printed in Denmark by Rosendahls, 2018

Thesis Outline

This dissertation is written as a paper-based thesis, where the attached publications are part of the work. The main body is therefore the frame of the topic, which summarizes the outcomes, puts them into perspective, and gives new insights into the analysis. For a more detailed discourse, the reader is referred to the attachment, which consists of the following papers:

[A] Model-supported Characterization of a PEM Water Electrolysis Cell for the Effect of Compression. Steffen Henrik Frensch, Anders Christian Olesen, Samuel Simon Araya, Søren Knudsen Kær. Electrochimica Acta, Vol. 263, pp. 228–236, 02/2018.

[B] Model-supported Analysis of Degradation Phenomena of a PEM Water Electrolysis Cell under Dynamic Operation. Steffen Henrik Frensch, Anders Christian Olesen, Samuel Simon Araya, Søren Knudsen Kær. ECS Transactions, Vol. 85 (11), pp. 37–45, 05/2018.

[C] Influence of the Operation Mode on PEM Water Electrolysis Degradation. Steffen Henrik Frensch, Frédéric Fouda-Onana, Guillaume Serre, Dominique Thoby, Samuel Simon Araya, Søren Knudsen Kær. Submitted to the International Journal of Hydrogen Energy, 11/2018.

[D] Impact of Iron and Hydrogen Peroxide on Membrane Degradation for PEM Water Electrolysis: Computational and Experimental Investigation on Fluoride Emission. Steffen Henrik Frensch, Guillaume Serre, Frédéric Fouda-Onana, Henriette Casper Jensen, Morten Lykkegaard Christensen, Samuel Simon Araya, Søren Knudsen Kær. Submitted to the Journal of Power Sources, 10/2018.

Additionally, the following papers were published during the PhD project, but not included in the discussion:

[X1] On the Experimental Investigation of the Clamping Pressure Effects on the Proton Exchange Membrane Water Electrolyser Cell Performance.

Saher Al Shakhshir, Steffen Henrik Frensch, Søren Knudsen Kær. ECS Transactions, Vol. 77 (11), pp. 1409–1421, 07/2017.

[X2] In-situ Experimental Characterization of the Clamping Pressure Effects on Low Temperature Polymer Electrolyte Membrane Electrolysis. Saher Al Shakhshir, Xiaoti Cui, Steffen Henrik Frensch, Søren Knudsen Kær. International Journal of Hydrogen Energy, Vol. 42, pp. 21597–21606, 08/2017.

[X3] Towards Uniformly Distributed Heat, Mass and Charge: A Flow Field Design Study for High Pressure and High Current Density Operation of PEM Electrolysis Cells. Anders Christian Olesen, Steffen Henrik Frensch, Søren Knudsen Kær. Electrochimica Acta, Vol. 293, pp. 476–495, 10/2018.

Lastly, the following conference contributions have been conducted:

[C1] Analysis of Impedance Spectra of PEMEC under Various Operation Parameters. Steffen Henrik Frensch, Samuel Simon Araya, Søren Knudsen Kær. 7^{th} International Conference on Fundamentals & Development of Fuel Cells (FDFC2017), oral presentation, 01/2017.

[C2] Conceptual Degradation Model for a PEM Water Electrolyzer. Steffen Henrik Frensch, Samuel Simon Araya, Søren Knudsen Kær. 1^{st} International Conference on Electrolysis (ICE2017), poster, 06/2017.

[C3] Model-supported Analysis of Degradation Phenomena of a PEM Water Electrolysis Cell under Dynamic Operation. Steffen Henrik Frensch, Anders Christian Olesen, Samuel Simon Araya, Søren Knudsen Kær. 233^{rd} Meeting of the Electrochemical Society (ECS233), oral presentation, 05/2018.

Abstract

In order to increase the share of renewable energy sources connected to the grid further, the most crucial obstacles to solve are long-term energy storage and grid stability. Energy storage is needed to tackle the mismatch between energy production and demand that comes naturally with unpredictable energy sources such as wind and solar. Grid stability on the other hand is challenged by their fluctuation, but has to be maintained at all times to ensure security of supply. One technology that may address both issues is hydrogen production through polymer electrolyte membrane water electrolysis (PEM WE). Hydrogen produced by PEM WE can act as an energy carrier for long-term storage, and when directly coupled to the grid, electrolyzers can provide grid stabilization services. One example of such an installation is the HyBalance project, which was inaugurated in September 2018 in Hobro, Denmark. The major obstacle for the technology at the moment is the high cost, which is mostly due to expensive materials and uncertain lifetime under dynamic operation. This work investigates degradation of PEM WE to evaluate their potential under the presented conditions.

Firstly, the performance as a function of compression was investigated. The main outcomes of the experimental study supported by a computational analysis are that an increase in compression increases the overall performance within the whole investigated range between 0.77 and 3.45 MPa. This is mostly due to improved contacts, which reduce the ohmic resistance. However, excessive compression may not be favorable electrochemically and in terms of transport of species. It furthermore is suspected to increase the risk of membrane perforation and therefore sudden failure.

Secondly, long term tests have shown that the ohmic resistance is the main contributor to voltage degradation. The processes can be separated into membrane thinning and structural adjustments, which decrease the ohmic resistance, and titanium passivation, which increases the ohmic resistance. For all tests at constant current operation, titanium passivation was found dominant. This is specifically the case for operation above 80 °C, which eliminates the benefit of increased efficiency at elevated temperatures and should therefore be avoided as the degradation rate increases significantly.

Dynamic operation of 10 s current cycles and direct coupling to a simulated solar profile on the other hand are in fact favorable in terms of voltage degradation. This is due to a decrease of total ohmic cell resistance over time, where membrane thinning together with a positive effect of structural adjustments within the catalyst layer dominates over titanium passivation. Dynamic operation furthermore reduced the impact of reversible voltage increase. This has been connected to a reverse of temporary blockage of active sites by oxygen bubbles by sudden current/potential shifts.

Lastly, membrane degradation was investigated in more detail through experiments and a computational model. Fluoride emission has been used as an indicator for membrane degradation as it results from a chemical attack of the ionomer. The fluoride emission revealed that high temperature operation is unfavorable, since it enhances hydroxyl radical generation from hydrogen peroxide, which is the driving force behind the attack mechanism. Furthermore, metallic impurities such as iron ions highly enhance fluoride emission and therefore membrane degradation as they catalyze the chemical attack reaction. The effect was visible experimentally and through simulations. Membrane thinning represents a lifetime limiting factor for both constant and dynamic operation due its promotion of gas crossover, which may create explosive mixtures.

However, dynamic operation was found to increase fluoride emission compared to constant operation, but no evidence of more severe membrane thinning was observed that could explain the decrease in total ohmic cell resistance. The fluoride loss is therefore connected to the ionomer within the catalyst layer, which improves the performance for dynamic operation due to structural adjustments.

Dansk Resumé

To af de væsentligste udfordringer ved integration af yderligere fluktuerende grøn energi i elnettet, er energilagring og opretholdelse af netstabiliteten. Energilagring er nødvendig for at håndtere den ubalance mellem energiproduktion og - forbrug, der naturligt kan komme med en stor andel af uforudsigelige energikilder som vind og sol i elnettet. Stabiliteten i elnettet skal opretholdes for at sikre forsyningssikkerheden. Hydrogenproduktion gennem polymer elektrolyt membran vandelektrolyse (PEM WE) er en teknologi der kan adressere begge problemer. Hydrogen produceret gennem PEM WE kan fungere som energibærer til langvarig opbevaring, og når det er direkte koblet til elektricitetsforsyningsnet, kan et elektrolyse-system sørge for netstabilitet. Den største hindring for denne teknologi er i øjeblikket den høje pris, som hovedsagelig skyldes dyre materialer og usikker levetid under dynamisk drift. Dette arbejde undersøger degraderingsmekanismer af PEM WE og deres omfang under de nævnte betingelser.

For det første, er ydeevne som en funktion af elektrolyse stak kompression blev undersøgt. Resultaterne af det eksperimentelle studie er understøttet af en beregningsanalyse og viser at højere kompression forbedrer den samlede præstation inden for hele det undersøgte interval mellem 0.77 og 3.45 MPa. Det skyldes især forbedret kontakt mellem de elektrisk ledende lag og der med reduceret ohmiske modstand. En for høj kompression er dog ikke nødvendigvis en fordel elektrokemisk og til i forhold til massetransport. Det formodes endvidere at kompression kan øge risikoen for membranperforering og derfor pludselige fejl.

For det andet, har længerevarende forsøg vist, at drift med dynamisk drift af perioder på 10 s og direkte kobling til en simuleret sol-profil faktisk er gunstig med hensyn til spændingsdegradering, da cellens totale ohmiske modstand er faldet over tid, mens drift med konstant strøm viste en stigning. Dynamisk drift reducerer endvidere effekten af reversibel spændingsforøgelse.

Høje temperature på over 80 °C skal på den anden side undgås, da nedbrydning øges markant.

Til sidst blev membran-nedbrydning som en levetidsbegrænsende faktor

undersøgt gennem eksperimenter og ved hjælp af en beregningsmodel. Fluoridemission er en indikator for membran-nedbrydning, da den kommer fra et kemisk angreb af ionomeren. Eksperimenter viste at en høj temperatur er ugunstig for fluoridemissionen. Eksperimenterne viste også at dynamisk drift øger fluoridemissionen, men der blev ikke fundet tegn på øget membranfortynding, som kunne forklare faldet i total ohmisk modstand. Fluoridtabet forbindes derfor med ionomeren i katalysatorlaget, hvilket forbedrer ydeevnen på grund af strukturelle forandringer. Ydermere påvirker jern urenheder og hydrogenperoxid stærkt fluoridemission og dermed membranfortynding, da de udløser den kemiske angrebsreaktion. Effekten blev simuleret gennem en model af et reaktionssystem, der beregner membranfortynding.

Contents

Preface

The here presented work has been carried out at the Department of Energy Technology at Aalborg University and was financially supported by Innovation Fund Denmark through the e-STORE project, who I would like to acknowledge therefore.

My most honest thank-you goes to my supervisor Prof. Søren Knudsen Kær and my co-supervisor Assoc. Prof. Samuel Simon Araya for their ongoing support throughout the whole period. Thank you for trusting in me, for the guidance and discussions, and for the environment you created that made the project a successful experience. Thank you for giving me the freedom to explore my own paths, and the honest feedback if that path was a one-way road.

Thank-you to Anders, Sobi, Jakob, Saher, Laila, Morten, Henriette, the laboratory staff, and my other colleagues at the energy department for the help in many ways over the time, may it be academically or not. For the latter, I would like to especially acknowledge the foosball crew for keeping my mind clear.

I would like to express a more than special thank-you to Frédéric Fouda-Onana and Guillaume Serre who made my stay at CEA Grenoble possible and spent uncountable hours of discussion, even after my return to Aalborg, and the rest of the CEA team that made me feel home for six months.

The biggest thank-you goes to my parents, LMS, and my whole family, who ground me and who I can always count on as my safety net. I will end with Catarina: You are not just one part of my life, but the basis.

Steffen Frensch
Aalborg University, 08. November, 2018

Chapter 1

Introduction

Fossil fuels such as oil, gas, and coal form the backbone of nowadays energy infrastructure. When looking at primary energy production, less than 10% of the 160 trillion kWh (13 647 Mt oil equivalent) were produced by renewable energy sources in 2015 [48]. Reasons against this dependence on fossil energy carriers are manifold and range from political dependence towards producing countries to economical considerations. However, the most discussed aspect in the public is the ecological impact on the planet. Proof for a human-caused climate change due to greenhouse gas emissions is widely accepted throughout the scientific community and many countries have therefore committed themselves to limit the global impact on the climate. For example, the Danish Government set itself the goal to be independent from fossil fuels by 2050 [24]. The sector that experiences the most notable changes is the electrical energy production. Worldwide, an estimated total of 6.30 billion kW electricity generating capacity was connected to an electrical grid in 2015, producing 23.14 trillion kWh of electrical energy [23]. The share of renewable sources such as hydro-electric, geothermal, solar, and wind was up to 20% worldwide, where some countries rely almost entirely on renewable energy [23]. However, that is mostly hydro-electrical, as it is the case for example in Norway and Lesotho, or geothermal energy, as it can be widely found for example in Kenya [21, 22]. Both are usually highly controllable and therefore represent ideal energy sources for a reliable electricity grid. However, they require certain geographical conditions that cannot be found everywhere. Therefore, the strategy in other regions of the world is to utilize wind and solar energy, as for example in Denmark and Germany.

An electrical grid should provide enough power at all times and ensure grid stability at an affordable cost, which is met fairly well by the fossil fuel-based energy systems in place, but at the expense of long-term livability of the planet. As solar and wind energy both represent a highly fluctuating

source that cannot be controlled, new challenges arise by increasing their share within the electricity grid. Firstly, consumption and production may generate a mismatch as production is dictated by the local weather conditions. This means, a long-term time shift has to be managed, where surplus energy can be stored for a later time when needed. Surplus energy may also be utilized outside the electrical sector, for example for fuel production such as methanol for the transportation sector. Secondly, the grid frequency in AC-grids (50 Hz in Denmark) is a highly sensitive parameter that has to be maintained within certain limits at all times. Automatic step-wise frequency stabilization is in action, where in Denmark for example the load is shedded in 10% steps, starting when the frequency falls below 49.0 Hz and 48.5 Hz in the western and eastern part of the country, respectively [28]. A short-term mismatch between consumption and production may affect the grid frequency, which has to be overcome. The European Network of Transmission System Operators for Electricity (ENTSO-E) is a European association that plays a key role in harmonizing grid standards. One of their objectives is to tackle issues connected to the integration of more renewable energy [30].

One technology that may address both issues at the same time is polymer electrolyte membrane water electrolysis (PEM WE). During the electrolysis of water, hydrogen gas is produced that may be stored and utilized again to be converted back into electrical energy. This represents the long-term shift of production/consumption mismatch. The PEM technology specifically exhibits certain features that also make it interesting for grid-stabilizing applications as detailed in section 1.1). Additionally, hydrogen produced by renewable energy powered electrolysis can be considered CO_2 neutral and therefore replace the state of the art process of natural gas reforming. The hydrogen gas may also serve as a substitute for natural gas in certain applications and therefore play an important role in all non-electrical applications such as transportation, heating, and many other industrial uses. Figure 1.1 illustrates an energy system that is based on hydrogen.

1.1 PEM WE Working Principle

The fundamentals of water electrolysis as well as the specifics of the PEM technology are describes in more detail in this section. Water electrolysis is a well known process that dates back to 1866 with the invention of the Hofmann voltameter [47]. It describes the process of electrochemically splitting water into its components hydrogen and oxygen as seen in equation 1.1:

$$2\,H_2O \longrightarrow 2\,H_2 + O_2 \tag{1.1}$$

Although the main principle remains the same, modern electrolysis plants

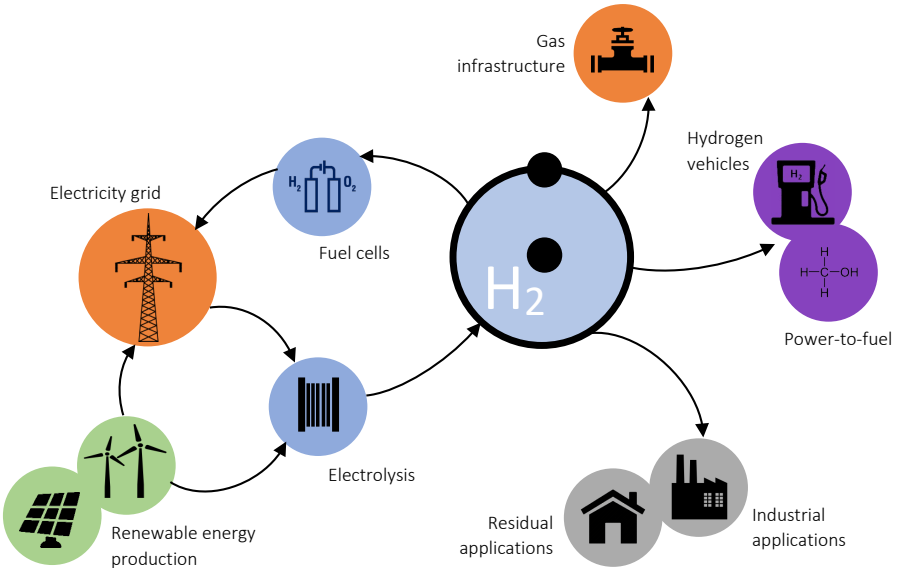

Fig. 1.1: Energy system based on hydrogen as an energy carrier including generation, distribution/storage, and application

are far more complex. Figure 1.2 illustrates a single cell with all major components including the involved reactions. Real life applications require high hydrogen flow rates or respectively high input power. This can practically only be achieved by connecting multiple cells in series, which is called a stack.

The most crucial components are the two electrodes and the electrolyte, which in the case of PEM is a solid polymer membrane that creates an acidic environment. The three components together make up the membrane-electrode-assembly (MEA). Purified water is typically fed on the anode side through small channels within the bipolar plate (BPP). The water crosses the porous transport layer (PTL) to reach the catalyst layer (CL), where the anodic oxygen evolution reaction (OER) takes place according to equation 1.2. The generated oxygen gas leaves the anode outlet together with excess water, while the humidified membrane allows only protons to cross. Together with the electrons that travelled through the external circuit, the protons reach the cathodic CL to form hydrogen gas through the hydrogen evolution reaction (HER) according to equation 1.3. The humidified gas leaves the cathode outlet through the PTL and the channels within the BPP.

$$2\,H_2O\,(l) \longrightarrow O_2\,(g) + 4\,H^+ + 4\,e^- \tag{1.2}$$

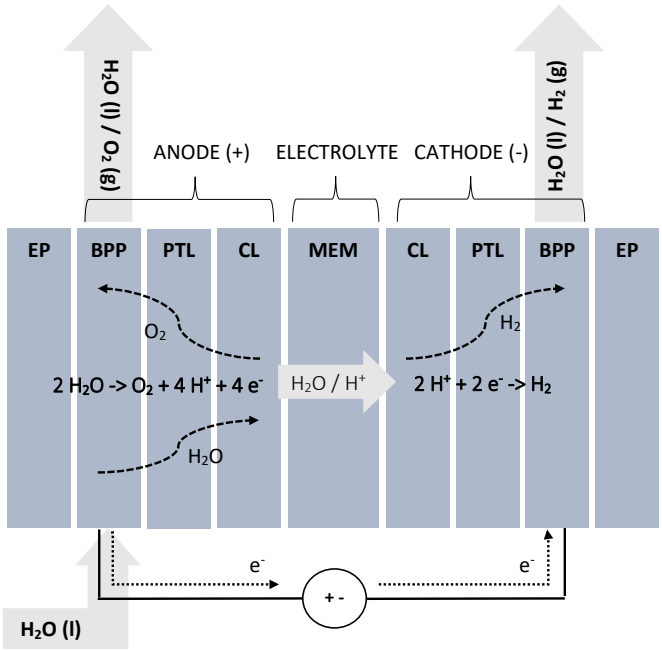

Fig. 1.2: Schematic of a typical PEM WE cell design. All components are sandwiched between two end-plates (EP) and may be repeated to form a stack. BPP = bipolar plate, PTL = porous transport layer, CL = catalyst layer, MEM = membrane

$$2\,H^+ + 2\,e^- \longrightarrow H_2\,(g) \tag{1.3}$$

One of the biggest drawbacks of the PEM technology is the high cost compared to the competing alkaline based technology. Alkaline electrolysis plants have been in operation since the early 20^{th} century [79]. The lack of expensive noble metals and the high maturity of the technology lower the investment cost considerably. Solid oxide electrolysis cells (SOEC) have to be mentioned as the third major electrolysis technology. SOEC based hydrogen production is an emerging technology that has a potential for many applications. Their main advantage is their high efficiency due to an operating temperature of more than 500 °C. However, this high temperature also comes with long start up times, which are generally less suitable for dynamic operation. Furthermore, the technology is not fully commercialized yet.

On the advantage side, PEM electrolysis exhibits some unique features that make the technology interesting, especially for grid-balancing applications [13]. On one hand, they can be operated at considerably higher current density, on the other hand, fast start-up and response times make them a

potent option for dynamic operation. However, sufficient lifetime at such dynamic operation has yet to be proven. Due to its solid membrane, another unique feature of the PEM technology is the possibility to internally pressurize the gases. When it comes to hydrogen gas storage, pressurized gas bottles of up to 700 bar are the most widely used option. A world-wide infrastructure for bottle refilling and distribution is in place, which may be reviewed when it comes to up-scaling of the technology in the GW-range. Underground caverns holding the gas at around 20 to 200 bar could present a feasible option for gas storage of that magnitude [33]. In both cases, hydrogen has to be pressurized in order to achieve acceptable volume-to-mass ratios. Also direct utilization in industrial applications such as methanol production requires hydrogen at a certain pressure. This can be done by external compressors, which are readily available on the market. However, their energy consumption would lower the overall system efficiency.

Internal pressurization within the stack can be done symmetrically, i.e. with both oxygen and hydrogen at the same output pressure, or asymmetrically, where only the hydrogen side is pressurized. Systems with internal pressurization of up to 50 bar are available, while demonstrations of up to 100 bar have been shown [50, 92]. This reduces the external compression demand or even makes it completely redundant, which lowers balance of plant (BoP) complexity.

Besides the stack, which is the heart of any water electrolysis plant, and possibly the discussed compression system, some other components are required for operation that make up the BoP. Figure 1.3 shows a typical installation.

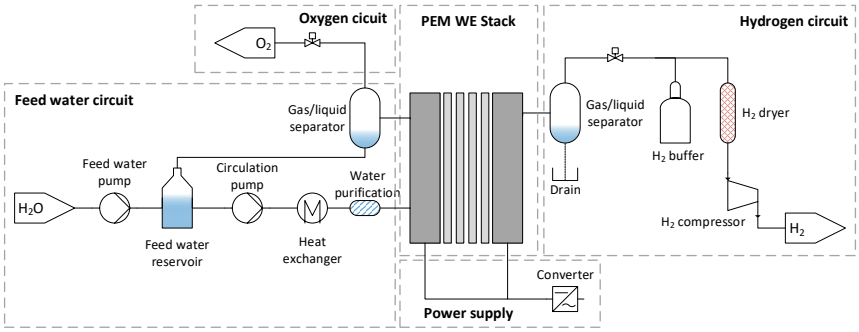

Fig. 1.3: Schematic of a typical PEM WE system including the balance of plant. If required, hydrogen gas may be delivered compressed through internal compression as described in the text. Feed water with a low conductivity is mandatory, which may require prior treatment

The power supply is a crucial component and may appear in different fashion depending on the application, which is discussed further in sec-

tion 1.2. Furthermore, the feed water may or may not be recirculated. In both cases it has to be highly purified, which may make further components such as ion exchange filters necessary. The feed water circuit may also be utilized for heat management, where the water itself represents the cooling liquid. However, in real systems, external cooling is usually required. Both gases can be stored in gas reservoirs or pressurized gas bottles, which makes it necessary to dry them beforehand. This is done in a gas/liquid separator, while the oxygen is sometimes just vented into the atmosphere instead of being utilized further. However, there is a potential market for oxygen utilization for example in medical applications [51].

1.2 Realistic Operation Scenarios

As discussed before, PEM electrolysis may serve different purposes. Besides hydrogen production, they are able to offer long-term energy storage and provide grid services. Depending on the application, the operation scenario may change and therefore impact performance and degradation significantly. Figure 1.4 illustrates three possible profiles that the electrolyzer has to follow.

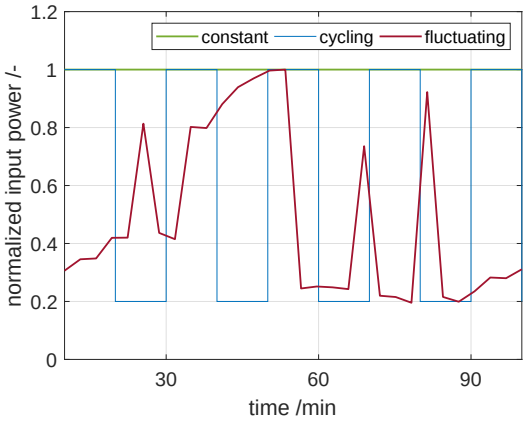

Fig. 1.4: Possible operation scenarios. The fluctuating input power case is based on real data from Denmark's offshore wind turbines from September 2018 (5 min resolution)

In the figure, the *constant* baseline would represent solely hydrogen production, for example for industrial purposes. The operation is steady or adjusted according to the demand over long periods. This mode can be optimized fairly easy, where cost and value generation are predictable to a high extent. When looking at the case of participation in grid services as it has been proposed in several discussions [37, 46], the scenario becomes far more complicated. If the system should be utilized to match long-term production

and demand through hydrogen storage, the *cycling* case in figure 1.4 represents a typical operation mode. In times of high production and low demand (e.g. strong winds during nighttime), the input power is very high in order to absorb excess energy. At other times, the system runs on lower power or may be switched off completely. This case is less predictable, but follows certain patterns such as day/night cycles. The system operator continues to be able to sell hydrogen to industrial outlets or utilize it for feeding energy back to the grid during low production/high demand periods. Furthermore, the energy cost for the hydrogen production may be low due to the high excess. Last but not least, providing grid services for frequency stability pushes the operation scenario to a more extreme. Excess power is highly fluctuating and little predictable. The *fluctuating* case in figure 1.4 illustrates a possible profile. Although the hydrogen production may not be as high as in the two earlier cases, the major value generation in this scenario is to act as a grid service provider. An extension of that are micro combined heat and power (μCHP) plants, which can be operated with intermittent hydrogen production to create a business case. A combination of any of the presented cases may be considered when designing and optimizing a PEM WE system.

1.3 Motivation and Research Goals

The main motivation of this work is to investigate the possibilities of further increasing the share of renewable energy sources within an electrical grid. The installed capacity of wind power in Denmark was 5.5 GW in 2017, which represents a share of around 40% [20, 96]. In the past, the generated wind power exceeded the countries total consumption on several days as for example on the 9^{th} and 10^{th} of June 2015 [29]. Energy storage and ensuring a stable grid frequency are crucial for a further increase in fluctuating energy sources such as wind and solar energy. This work contributes by evaluating the possibility of utilizing PEM WE systems in an electrical grid for the presented purposes of energy storage and providing grid services, where one of the major issues is the lifetime under dynamic operation. The problem is addressed firstly by an experimental approach on single cells, and secondly by a lifetime simulation with the membrane being the restrictive component. The main objectives can be summarized as:

- Identify the most crucial operational parameters and their impact on PEM WE performance degradation
- Evaluate the suitability of PEM WE in highly dynamic operation scenarios
- Develop a model that predicts the lifetime under several operating conditions

Chapter 2

State of the Art PEM WE Degradation

This chapter introduces the state of the art of PEM WE while focusing on issues related to degradation. The discussion is separated into the main components membrane, catalyst, and others. Besides the given references, a good review of PEM WE performance and critical research gaps can be found in [7, 16]. To start with, the featured terminology as used in this work is clarified.

Quality is defined by the extent a product fulfills the advertised qualities at the beginning of life. In the case of PEM WE that may be an efficiency, gas purity, or alike. These parameters may suffer from *degradation* related to aging throughout its time of use, where degradation is separated into reversible and irreversible decrease in performance. The ability to maintain BoL performance to a certain degree is called *reliability*, with *durability* usually referring to irreversible processes, whereas *stability* describes the ability to recover from reversible losses [36]. When degradation or sudden catastrophic failure causes the product to not meet the requirements for the specific application anymore, the product can be said to have reached its end of life (EoL). To the author's best knowledge, no standards define the EoL for PEM WE further. However, for PEM WE as for PEM FC, the EoL can be caused by three main reasons: technical, safety-related, and economical [25]. A technical EoL could be to fail meeting the required gas production rate, while safety-related issues include the creation of explosive hydrogen-oxygen mixtures. Lastly, if the hydrogen production cost is getting too high due to an efficiency loss, an economical EoL is reached. It should be noted, that reaching one EoL criteria in one application does not automatically exclude the system from performing sufficiently well in another application.

2.1 Characterization Techniques

Due to the high similarity between PEM WE and FC, the most commonly applied characterization methods are virtually the same and therefore well established [58]. However, there are important differences in their practical application and analysis. The major methods used in this work are polarization curves (IV), electrochemical impedance spectroscopy (EIS), cyclic voltammetry (CV), and scanning electron microscopy (SEM) and are shortly introduced in this section.

Polarization curves are the most straight forward method to quickly evaluate the overall cell performance. In potentiostatic mode, the curve is constructed by imposing a voltage and measuring the current, the galvanostatic mode describes the other way round. Sensitive parameters are the resolution of data points, the dwell time at each operation point, and accuracy of the measuring device. If all are chosen appropriately, the data may already reveal in-depth information about the cell. This includes information about involved voltage losses which may be connected to the different reaction mechanisms and components (see also section 2.4). The data may be presented in IV curves, where the voltage is typically plotted against the current density, or in Tafel plots, where usually the overpotential is plotted against the logarithmic current density. However, to draw more confident and meaningful conclusions, polarization data cannot serve as the sole characterization method. Furthermore, the technique can be disruptive when studying degradation since the recording of the curve involves changing the operation to a high extend.

Electrochemical impedance spectroscopy is a non-disruptive alternative to IV curves to characterize a cell. It should be noted that these two methods can co-exist, but not replace each other. EIS has far more potential to gain insight into electrochemical systems compared to simple polarization measurements, at the cost of much higher complexity for the equipment as well as the analysis. Generally, an AC disturbance signal is super-imposed on a DC bias signal, while the response is recorded. As IV curves, the method can be applied potentio- or galvanostatically, where in both cases the main parameter for optimization is the magnitude of the disturbance signal, that balances between noise reduction (achieved through high disturbance signal magnitude) and ensuring steady state operation (achieved through low disturbance signal magnitude). The signal is imposed at various frequencies, which makes it possible to connect the response to certain components or electrochemical processes. For that purpose, a helpful tool for the analysis is to fit the data to an electrical equivalent circuit (EEC). However, EIS is a

highly complex technique, and the fitting process has to be done with caution, since it is prone to wrong conclusions.

Cyclic voltammetry is a versatile tool that plays an important role in many branches of fundamental and applied electrochemical research, where the data is shown in a cyclic voltammogram. A potentiostat records the current while an imposed voltage is swept between two limits. Attention has to be paid not only to the upper and lower voltage limit, but also to the scan rate. Typical applications in PEM WE research are for example investigations on catalyst performance.

Scanning electron microscopy is a destructive and therefore post-mortem characterization method. In SEM, images of high resolution can be obtained by means of an electron beam. The major application within PEM research is to examine the MEA's cross section. The captured images reveal insight into the different layers in terms of their thickness and geometrical structure. When compared to a fresh sample, SEM presents an effective way to qualitatively and quantitatively evaluate degradation processes.

2.2 Degradation Mechanisms

Figure 2.1 shows an overview of possible degradation mechanisms grouped into the main components. The classification was done within the European NOVEL project and presented at the *Second International Workshop on Durability and Degradation Issues in PEM Electrolysis Cells and its Components* in Freiburg in 2016 [68, 87]. The main effects (marked red in the figure) and some other effects will be discussed in the following literature review. A comprehensive review of PEM WE degradation can be found in [32].

2.2.1 Membrane

As seen in figure 2.1, membrane degradation can be classified into three main groups: mechanical, thermal, and chemical. The analysis here focuses on the state of the art perfluorosulfonicacid (PFSA) membranes such as Nafion® or Aquivion® with thicknesses between 100 µm and 200 µm [7]. As the material is the same, the mechanisms are equally valid for the ionomer within the catalyst layers. Their implication will be discussed in section 2.2.2, whereas this section focuses only on the impact on the membrane directly.

As long as the operating point remains below the melting point of the materials, thermal degradation is usually more a result and a trigger rather than a mechanism. Inhomogeneities in thickness, catalyst activity, or the like within the layers may cause hot spots (result), which in turn accelerate

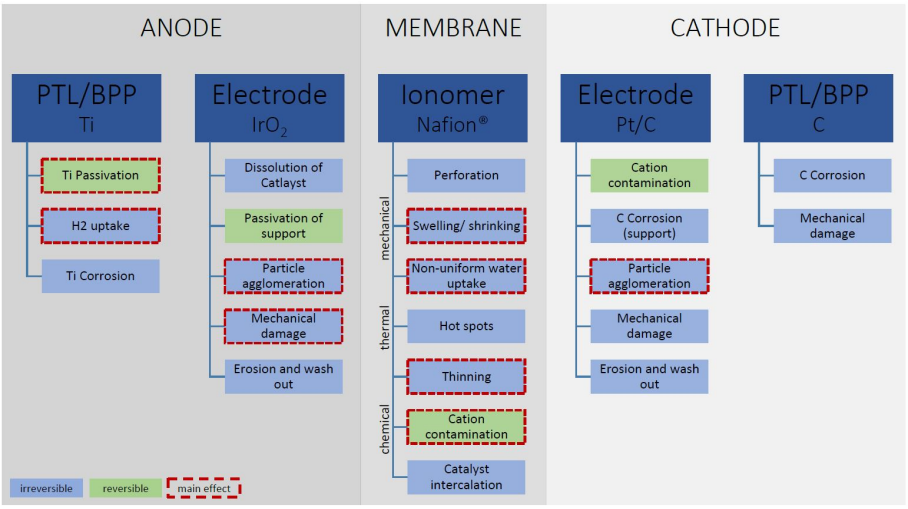

Fig. 2.1: Overview of PEM WE degradation mechanisms separated by components. All main effects (marked red) are described in more detail in the text. Adjusted from [87]

chemical degradation (trigger). However, a study on the effect of elevated temperature and pressure found that both factors have a significant effect on membrane degradation under PEM WE conditions [63]. The authors report the conductivity over time at 110 °C, 130 °C, and 150 °C at 0.5 MPa and 0.7 MPa. Both parameters lead to increased rates of conductivity loss, which they attribute to internal structural changes caused by swelling of the Nafion® rather than chemical degradation.

This membrane swelling and shrinking may also be connected to non-ideal water supply [32] and results in local mechanical stress. Local mechanical stress on the other hand leads to non-uniform changes in the membrane geometry and can be observed as a problem for membrane lifetime in the literature [15, 90]. The result is an inhomogeneous current distribution, leading to hot spot formation. Hot spots are characterized by a significant local increase in temperature. Causes and implications may vary, but it has been reported in the literature that pinholes and perforation are a direct cause [66], which may lead to an immediate safety EoL due to dangerous levels of gas crossover.

Gas crossover altogether represents one of the major safety issues for PEM WE. Catastrophic failure due to membrane perforation can be caused by the direct combustion of hydrogen and oxygen on a platinum catalyst as seen in [66]. Furthermore, an increase of hydrogen gas crossover over time may result in the formation of explosive hydrogen/oxygen mixtures at the anode [43, 44]. This becomes most relevant at low current or dynamic operation, where the oxygen generation at the anode is low. The hydrogen permeation

at low currents [94] can create an environment above the lower explosion limit (LEL) of around 4vol-% hydrogen in air at 80 °C [65]. Operation at asymmetric pressure condition ($p_{cathode} > p_{anode}$) aggravates the issue due to increased hydrogen permeation [95]. Oxygen crossover on the other hand may facilitate the formation of hydrogen peroxide, which in turn accelerates membrane degradation even more. Lastly, it decreases gas purity, resulting in a possible technical-EoL depending on the application [8]. Pinholes may also be the result of the PTL fibres piercing the membrane, which is directly coupled to the applied compression on the MEA [26, 32]. Additionally, high gas pressure operation enhances mechanical stress, where the main issue again becomes gas crossover.

Finally, chemical membrane degradation is a lifetime limiting factor [32]. The major mechanisms are based on metallic impurities that stem from the BoP, the feed water, or the MEA. One understanding is that cations such as Fe^{2+} dissolve into the membrane, where they occupy ion exchange sites [85, 93]. This lowers the proton conductivity and therefore increases the ohmic overpotential, since protons cannot be transported effectively anymore. This process is shown to be reversible in the literature [93]; however, it requires a complete disassembly of the cell or stack in order to access the MEA and immerse it in sulfuric acid. Another source of metallic impurities are the catalyst layers, where platinum particles have been observed to migrate into the membrane [41]. However, the particles most likely originated from the anode side, where platinum is not a suitable catalyst material due to its high instability within the voltage range. A much lower dissolution of the respective material is observed when switching to iridium or ruthenium based oxides [4].

Apart from the described metal cation contamination, iron and other metallic ions may also catalyze a reaction known as the Fenton reaction. It is well known to cause membrane thinning in PEM FC and proven to also occur in PEM WE. As it is detailed in chapter 5, the reader is also referred there. In principle, radicals such as hydroxyl ($HO^{\bullet}$) and hydroperoxyl ($HOO^{\bullet}$) are generated in the presence of hydrogen peroxide (H_2O_2. Some of these radicals in turn attack the membrane, which can be observed through fluoride (F^-) release and thinning. The most common way to report fluoride release is through area-normalized emission rates (FER). This is done by determining the F^- concentration in the effluent water. The reported order of magnitude is between $1 \cdot 10^{-1}$ and $1 \cdot 10^{1} \mu g\,cm^{-2}\,h^{-1}$, where one of the most comprehensive datasets for PEM WE can be found in [34]. The authors found an impact of temperature, where the release rate roughly triples with an increase from 60 °C to 80 °C. This is qualitatively and quantitatively in line with previous findings [53]. More interestingly, they also found an impact of current density which peaks between $0.2\,A\,cm^{-2}$ to $0.4\,A\,cm^{-2}$. The factor between the minimum and maximum FER is roughly two. At all times, the FER at the cathode

is by far higher compared to the anode. The authors furthermore found evidence through SEM that links the fluoride loss to membrane thinning. Membrane thinning through SEM without FER data was also identified by other researchers. The observed decrease was at times substantial and accounted for around 50% [85] and up to 75% of the initial thickness [41]. Among the first published evidence for membrane material loss in WE applications dates back to 1998, where a stack was found to degrade inhomogeneously [90].

Theoretically, a thinner membrane leads to a decrease in ohmic resistance. The total ohmic resistance of the cell can be measured by means of EIS, where a decrease of the high frequency intercept (HFR) in the Nyquist plane over time is in fact observed by some researchers [4, 55, 85]. However, the drop in HFR is lower than what the thinning would suggest [85], and an increase in HFR over time is also reported in the literature [55, 75, 93]. Since the HFR is equivalent to the total ohmic resistance and not only the membrane resistance, that may be explained by a coupling of other phenomena that increase ohmic resistance. Among others, that may be the evolution of a oxide layer on the PTL as further explained in section 2.2.3. The problem with membrane thinning through chemical attack is the above mentioned increase in gas crossover that may lead to a technical or safety-related EoL.

2.2.2 Catalyst Layers

The state of the art catalyst materials are iridium-oxide (IrO_2) at the anode and carbon-supported platinum (Pt/C) at the cathode. Both layers have a content of around 5% to 25% ionomer for binding purposes [10, 16]. Therefore, the binder may experience the same degradation phenomena as described in section 2.2.1 above. This may imply different mechanical issues such as a structural change within the CL, which may lead to a loss of performance [32]. Furthermore, ruthenium-based catalysts may be more efficient for the OER, but IrO_2 represents the best compromise between performance and stability [31]. The same conclusion was also drawn by a screening of different materials, which were evaluated for stability by means of a cycling voltage profile [88].

The noble-metal loading is usually between 0.5 and $2\,mg\,cm^{-2}$ for the anode and $\leq 1\,mg\,cm^{-2}$ for the cathode [7, 16], while lower loading may effect stability [19]. However, low catalyst loading was successfully demonstrated by other researchers [11, 91]. Their Pt loading as low as $0.025\,mg\,cm^{-2}$ achieved decent performance, while Ir loading was found to be optimal within 1 and $2\,mg\,cm^{-2}$ due to homogeneity issues at the lower and mass transport limitations at the upper end. However, promising results are reported by [77], who reduced the IrO_2 loading to $0.1\,mg\,cm^{-2}$ without compromising the performance. The authors claim that by adding a Ti-support, the ohmic resistance is decreased significantly and they achieved 1000 h with

decent durability. The reported degradation rates of $180\,\mu V\,h^{-1}$ with regular loading and $20\,\mu V\,h^{-1}$ with Ti-supported reduced loading, respectively, are contextualized to reported values in the literature in figure 2.2. TiC-supported Ir was also found to improve performance compared to unsupported Ir of up to one order of magnitude, which is connected to a lower polarization resistance due to improved deposition of particles [62]. However, any support is again prone to their unique degradation potential such as Ti-passivation is this case [89].

A general degradation issue connected to both the anode and cathode catalyst is the loss of electrochemical surface area (ECSA) [32], which is connected to the geometrical area by the roughness factor. The ECSA can decrease over time due to an agglomeration of catalyst particles and therefore an increase in mean particle size. In [76], the authors identified roughly a doubling in diameter at the cathode (Pt/C) through XRD and TEM analysis for constant and dynamic operation, while no change was observed at the anode (IrO_2). Although no reaction pathway for particle agglomeration has been reported, similar underlying mechanisms as known from FC research are generally conceivable [89]. This includes coalescence (for example through thermal sintering) and Ostwald ripening (through dissolution and redepositioning) [89]. Pt particle mobility has been found to be a function of the cathode potential [73], where a more negative potential leads to higher mobility. At the same time, [76] found no Pt migrated to the anode or Ir to the cathode at various long-term operation modes. At elevated voltages of $>2.05\,V$ vs. RHE as it may be the case for the PEM WE anode, the more volatile species IrO_3 can be formed and cause dissolution [89]. This can potentially also cause catalyst loss, which has been reported for Pt particles [41]. Lastly, reversible cation contamination may temporarily decrease ECSA as reported by [93].

2.2.3 Other Components

One of the most severe challenges in PEM WE degradation is the harsh environment especially at the anode. Low pH values of less than 4, elevated temperature of up to 80 °C, and voltages of up to more than 2 V and more at the presence of pure oxygen require materials with high resistance towards corrosion [16, 32, 52]. Therefore, the stable but costly Ti became the standard material for anode PTL and BPP [7], which makes the BPP the major contributor to the whole stack cost with around 50% (2010 and 2014 estimations) due to material and high machining cost for Ti [6, 12, 69]. However, even Ti is not immune towards aging and is reported to potentially contribute quite a share to the overall cell voltage increase over time. It is believed that titanium develops an oxide layer on its surface, which on one hand protects the material from further corrosion, but on the other hand increases the in-

terfacial contact resistance (ICR) [7]. This hypothesis has been validated in a long-term experiment, where the interfacial contact resistance (ICR) of the Ti-PTL before and after the test was compared. Since the ICR measurement was carried out ex-situ, the result is qualitative, but the increase is observable, and the theory is in line with the reported increase in HFR over time [75]. The authors repeated the experiment under the same conditions with a Pt-coated Ti-PTL that supposedly prevents the development of an oxide layer. The ICR remained almost constant, resulting in a much lower overall cell voltage increase. This underlines the impact of PTL-passivation in PEM WE degradation, and the possible mitigation through coatings, which has been reported before [5]. However, Pt coatings are expensive to apply and increase material cost [52]. The same applies for coatings on stainless steel BPP [38].

Another issue is the hydrogen uptake by titanium at elevated potentials and temperatures and the resulting embrittlement. However, the whole system is highly complex and the available literature lacks comprehensive studies. Theoretically, if the hydrogen uptake exceeds a certain threshold of solubility, a further uptake may result in cracks. However, the above described passivation layer should protect the Ti components against such, while humidity and pH value affect absorption abilities. On the other hand, fluoride ions from the previously described membrane attack have the ability to attack the oxide layer [32]. Therefore, hydrogen embrittlement in titanium components remains a topic of research, while at the same time alternative materials and coatings are also investigated [52, 57].

Finally, Ti particles probably originating from the anode PTL have been found at the cathode electrode, where they effectively lower the exchange current density over time [76].

2.3 Quantifying Voltage Degradation

Most of the previously discussed degradation phenomena have a direct impact on the cell voltage. Therefore, the evolution of the voltage at a certain current over time is a suitable parameter for capturing the overall degradation. It is potentially interesting for comparing different materials, cell designs, or operation modes. However, this voltage degradation rate has to be seen as a first figure and cannot serve as the sole indication for degradation and the end of life. One of the biggest problems connected to it is the lack of standardized protocols and clear definitions of how to calculate the parameter. Especially in the context of dynamic operation and variable applications, a time-based degradation rate has limited significance to describe the relevant degradation. For example, a PEM WE system for energy storage operates in a very different pattern and has a different added value than one that mainly operates for industrial hydrogen production (see section 1.2). A molar-based

degradation rate that takes the hydrogen production into account is already more flexible in order to asses performance loss and can be observed in the literature [76]. The two numbers are convertible into each other as long as the operation profile is known.

However, a review over the available literature that includes long-term voltage degradation is a useful overview and can be a good starting point to evaluate the most crucial parameters for degradation. An extraction of the most relevant literature can be found in table 4.2, where the outcomes of this work are put into context. Figure 2.2 shows the values of the complete considered dataset as a function of temperature and publication year. However, the dataset contains experiments with considerably different conditions such as catalyst loading or active area. Furthermore, the degradation rates are in most cases only reported for one current operation point. As it will be shown in chapter 4, the voltage degradation rate is dependent on the reference current point. Nevertheless, the lack of a clear relationship exemplifies the difficulties of comparing quantitative data due to different test conditions and the associated problems with reproducibility of data across the laboratories in the world. It does however indicate a trend, that voltage degradation rates rise with temperature. The vast majority of reported experiments was carried out at 80 °C, while only one was found above that. Although not claiming completeness, the figure also indicates a risen interest in PEM WE degradation as most data was collected within the past 5 years.

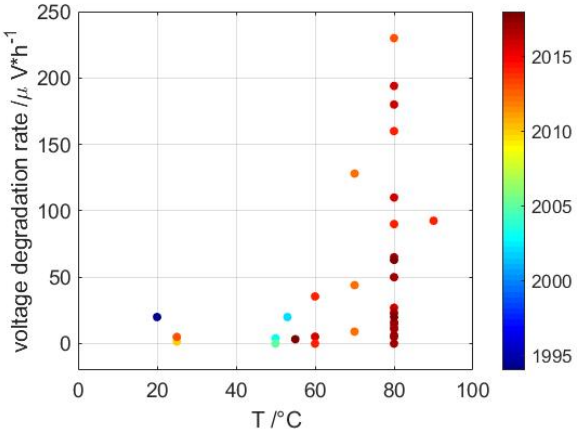

Fig. 2.2: Voltage degradation rates as a function of temperature and publication year as reported in the literature

2.4 Modelling Approaches

PEM WE degradation models are very rare and in fact, only one was found within the published literature in [17]. It addresses the issue of membrane degradation, where the authors present a 1D gas-crossover model and a set of ten electrochemical reactions, which simulate membrane attack and eventually thinning. Finally, a lifetime prediction is given based on the criteria that explosive gas mixtures cause a safety-related EoL. The approach is similar to what can be found for PEM FC degradation models, of which few can be found in the literature [40, 45, 82, 98]. Another FC membrane degradation model is based on empirical laws [18] and could be done similarly for WE. The authors investigated the effect of potential, pressure, and humidity on FER and turned the outcomes into empirical formulas. A system model that focuses on temperature-dependent degradation was developed throughout the LastEISys project at DLR [27], but further publicly available information was not found.

Additionally, several mathematical performance models are available [1, 64], which can be implemented into degradation models after some adjustments. A good overview of performance modelling can be found in several review papers [2, 16, 72]. Furthermore, some 3D models for two-phase flow and bubble transport, which is specific for PEM WE, can be found [3, 71]. Notably well investigated is high pressure operation including gas-crossover at asymmetrical condition from cell to system level [8, 9, 42, 80, 81, 94, 95]. This strongly supports the high relevance gas permeation plays in PEM WE.

Chapter 3

Investigations on PEM WE Performance

Before studying degradation phenomena, characterization methods and the BoL performance were investigated. This chapter introduces the methodology, EIS peculiarities for PEM WE, and summarizes the findings throughout this PhD project connected to cell compression. Some results were published in peer-reviewed outlets as shown in the outline (papers [A], [X1], and [X2]).

3.1 MEA Characteristics and Production

Throughout the project, two different types of cells were used for the experiments as described here. The MEA production protocol has been reported to have an effect on performance and degradation [85], which makes it a relevant parameter for comparison.

Cell type I Nafion® 117 served as the solid electrolyte for the small cells with 2.89 cm^2 active area. As the MEAs were provided by EWII Fuel Cells A/S, Denmark, no further information on the production method is known. However, the anode and cathode catalyst layers consisted of 0.3 $mg\,cm^{-2}$ IrO_2 and 0.5 $mg\,cm^{-2}$ Pt/C, respectively. Additionally, the anode exhibited a metallic Ir layer with a loading of 2.48 $mg\,cm^{-2}$. A Ti-felt of 350 µm and 81% porosity, and Sigracet® 35DC carbon-paper were used as PTLs. The MEAs were investigated in the setup seen in figure 3.1a. The feed water was recirculated at 270 $mL\,min^{-1}$ (around 93 $mL\,min^{-1}\,cm^{-2}$). This represents a high overstoichiometry to ensure decent temperature control, which is solely done by the pre-heated feed water itself.

Cell type II The 25 cm^2 MEAs were made in-house. The cathode ink is based on Pt/C (46.6%) with a catalyst-to-binder ratio of a bit more than 3:1. The anode ink is based on IrO_2 with 10% binder. Both inks were sonicated for 210 s and sprayed onto a PTFE decal on a 120 °C hot plate, while anode and cathode loadings were aimed at 1.0 $mg\,cm^{-2}$ and 2.2 $mg\,cm^{-2}$, respectively. Consequently, the electrodes were transferred onto a Nafion® 115 membrane in a hot press at 170 °C for 5 min at 300 kg followed by 2 min at 2000 kg. 1 mm thick Ti with 30% porosity and Sigracet® carbon-paper were used as PTLs for anode and cathode, respectively. The setup seen in figure 3.1b was utilized for this cell type. Pre-heated feed water together with electric heating pads on both sides established good temperature distribution. The water was fed at 500 $mL\,h^{-1}$ (0.33 $mL\,min^{-1}\,cm^{-2}$) without recirculation.

3.2 EIS for PEM WE: A Case Example

Although the technology and method are the same for PEM WE and FC, the application and analysis of EIS in PEM WE bears many distinct features and pitfalls. One of the differences in terms of hardware requirement is that fuel cells need a load for setting a DC bias, whereas electrolysis requires a power supply. Commercially available electrochemical workstations with around 30 A to 80 A [14, 39] are therefore usually limited to single cell operation at moderate current density and cell area. Furthermore, the involved electrochemical reactions are different and do not exhibit the same characteristics. However, the literature is by far more exhaustive for FC applications, which can be used as a foundation for implementing EIS as a tool for WE.

The example data shown in figure 3.2a (black circles) was measured on the previously described cell "type I" at 80 °C and 2.0 $A\,cm^{-2}$. The figure also shows two fits with a similar goodness of fit and similar residuals. However, the blue fit curve was fitted to the EEC with two $R//CPE$ circuits shown in figure 3.2b, while the red curve used one more $R//CPE$ circuit as shown in figure 3.2c.

The example illustrates the difficulties connected to fitting EIS data to an EEC. Without detailed knowledge of the investigated system EIS can lead to questionable or even incorrect conclusions, since the presence of an additional $R//CPE$ should be justified. A mechanistic process model has been presented in the PEM FC literature including an EEC based on the analytically determined impedance of the cell [67]. A similar approach may be followed for PEM WE. While the high-frequency series resistance R_{HF} may be connected to the total purely ohmic contribution of the cell fairly certain, the $R//CPE$ circuits are troublesome to explain and one has to be careful with connecting them to specific components of the investigated assembly. Generally, each $R//CPE$ circuit represents one process with a time constant

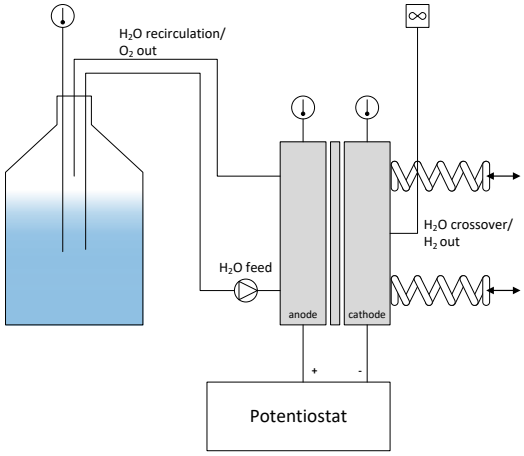

(a) Schematic of the test set-up used for cell "type I" (2.89 cm^2 active area). The potentiostat acted as a power supply for all tests

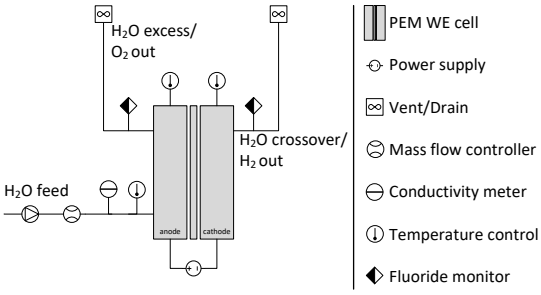

(b) Schematic of the test set-up used for cell "type II" (25 cm^2 active area). The power supply was replaced by a potentiostat during characterization

Fig. 3.1: Test set-ups for cell types "I" and "II"

connected to it, but as the example shows, the processes may merge and become inseparable. Therefore, EIS measurements can provide a powerful insight into the investigated system when relatively compared to each other, while only one parameter is changed.

Besides the total ohmic resistance R_{HR} represented by the HFR in the Nyquist plot, the LFR equals the total polarization resistance. It should therefore be equal to the slope of the polarization curve at the respective current operation point, which has been shown to be the case to an acceptable degree.

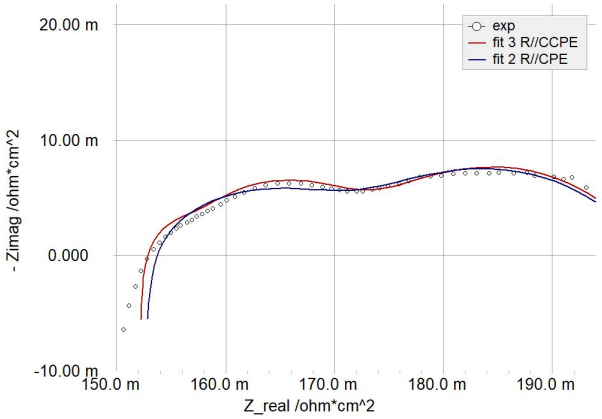

(a) EIS data fit based on the two EEC shown below. The similar fits may lead to different conclusions depending on the chosen EEC

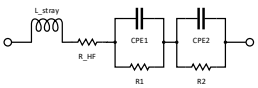

(b) EEC with a series resistance and two $R//CPE$ circuits

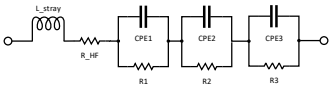

(c) EEC with a series resistance and three $R//CPE$ circuits

Fig. 3.2: Electrochemical impedance spectroscopy (EIS) based on electrical equivalent circuits (EEC)

3.3 Impact of MEA Compression on Cell Performance

The cell compression is a crucial parameter and impacts both performance and degradation. First and foremost, the BoL performance is a function of MEA compression and should therefore be reported to enable meaningful comparison throughout the literature. However, that is often not the case and moreover the literature lacks studies on the impact of PEM WE cell compression. Within this PhD project, the effect of compression was experimentally investigated on a single cell as shown in paper [A]. The 2.89 cm^2 state-of-the-art cell as described in section 3.1 ("type I") was electrochemically characterized at its BoL in the set-up shown in figure 3.1a.

The temperature was held constant at 60 °C and 80 °C through the feed water, whereas no other equipment than a potentiostat was used as a power supply. Four die springs were used to control the compression in eight steps

as shown in table 3.1.

step #	0	1	2	3	4	5	6	7
c /MPa	0.77	1.15	1.53	1.92	2.30	2.68	3.06	3.45

Table 3.1: Compression steps

The compression pressure P_c was calculated according to equation 3.1 and validated in an assembled cell through pressure-sensitive film.

$$P_c = \frac{F_s}{A} = \frac{R_s \cdot x}{A} \tag{3.1}$$

In the equation, A represents the compressed area, and F_s the compression force exerted by the springs which is given by the spring constant R_s and the displacement x.

At each compression step, an IV curve and EIS measurements at various current densities were carried out at both temperatures. Figure 3.3 shows the HFR and LFR at 1.0 A cm^{-2} as a function of compression.

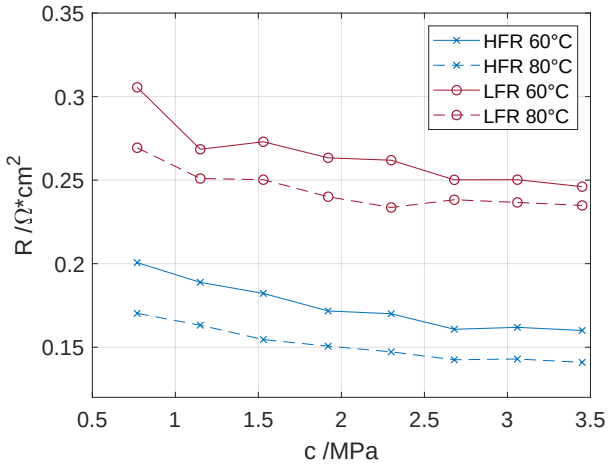

Fig. 3.3: High- and low-frequency intercepts at two temperatures as a function of cell compression. Source: [A]

While the total ohmic resistance represented by the HFR decreases with temperature is connected to higher Nafion® conductivity, the decrease with compression is related to improved contacts. The order of magnitude of the effect is similar for both parameters, where a temperature rise by 20 °C decreases the HFR by around 15% and an increase in compression by 2.68 MPa results in a 20% drop in HFR. To facilitate the analysis, the following results refer to the measurements at 60 °C.

To support the experimental results, a previously developed model [70] was slightly adjusted and utilized to fit the polarization data. Figure 3.4 shows two of the extracted parameters.

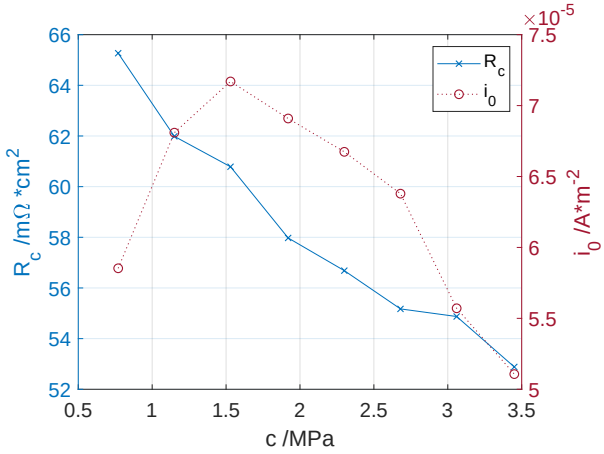

Fig. 3.4: Model fit values of contact resistance and exchange current density as a function of cell compression. Source: [A]

While the sum of all internal contact resistances R_c is decreasing, the apparent exchange current density i_0 seems to have an optimum value at around 1.53 MPa. The apparent exchange current density is an indication for the ECSA, which may be increased as voids are being filled and three phase boundaries are being formed with higher compression. At the turning point, the porous PTLs may crush, effectively smoothing the surface and therefore decreasing ECSA. At the same time, the membrane resistance is slightly increasing with compression. This is due to the lower water uptake of Nafion® at higher compression. However, the decrease in contact resistance is dominating and therefore the total ohmic resistance is decreasing. To further identify the major contributors to the total contact resistance, accessible components were investigated ex-situ as seen in figure 3.5.

The measurements reveal that the contact between the cathodic carbon BPP and the copper current connector is responsible for the major share, while the anodic BPP against the PTL (both titanium) is small. The difference between the experimental sum and the model prediction can partially be explained by the missing contacts that are not accessible for ex-situ measurements such as both CLs and the cathodic PTL.

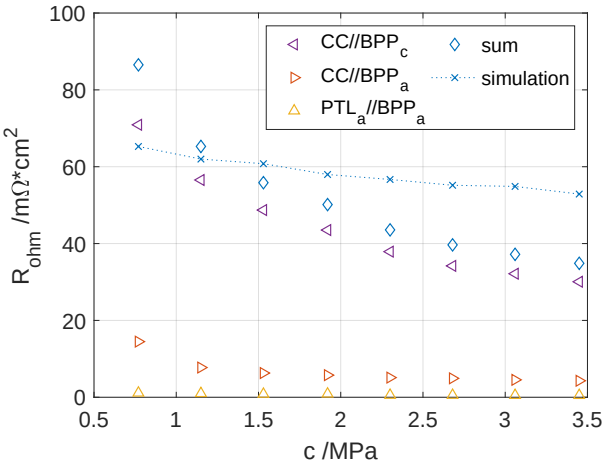

Fig. 3.5: Contact resistances as measured ex-situ (markers) and simulated (dotted line) as a function of cell compression (CC = current connector). Modified from [A]

3.3.1 Impact of MEA Compression on Cell Degradation

Cell compression is directly coupled to degradation and may affect it in several ways. Firstly, too high compressions exert a force on all components that may mechanically damage them immediately or gradually over time. One mechanism that was observed in this work for cell "type I" is the formation of a pinhole, where it is believed that a fibre of the PTL pierced the membrane as seen in figure 3.6a. The cell was run at current densities between 1.0 and 2.0 A cm^{-2}, 60 °C to 80 °C, and 2.30 MPa compression pressure. The pinhole formed after around 1816 h, which manifests itself with a sudden increase in voltage from 2.53 V to 12.48 V accompanied by a drop in current close to zero as seen in figure 3.6b. The suspicion that high compression may be responsible or at least facilitated the pinhole formation is supported by the formation of bulges in the MEA at the cathode channel areas.

Secondly, the compression is a function of time, be it due to loosened bolts, material expansion/shrinkage due to temperature variation, or the loss of ionomer and the resulting thinning of membrane and/or CL. To the best knowledge of the author, the impact has not been reported in the literature, but to completely disregard compression as a factor for performance change and to ensure comparability, it should be maintained constant. This may be achieved through an adjustable hydraulic compression system [97].

Lastly, the gas crossover was found to be dependent on the cell compression as shown in paper [X2]. Although the impact was found to not be as substantial as other factors such as temperature and current density, the cell compression may have an influence on lifetime when considering operation

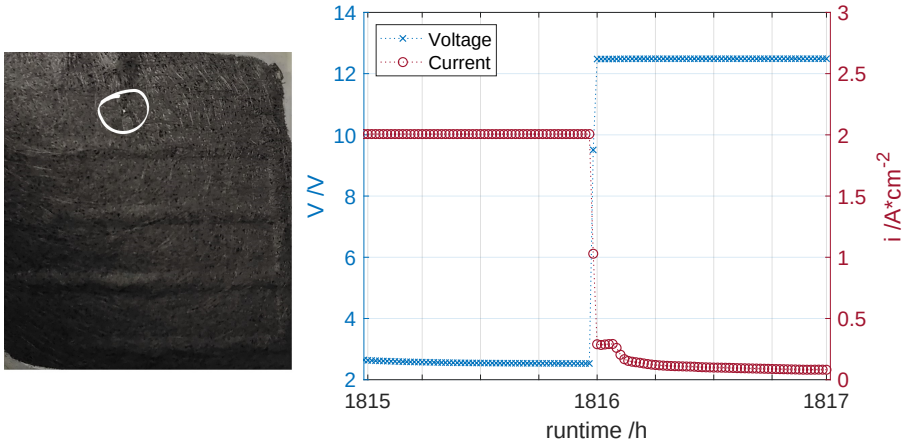

(a) Picture of the MEA after the test was terminated. A pinhole (circled) can be observed

(b) The data log reveals that the pinhole was formed after 1816 h. The voltage suddenly increases by 10 V, while the current drops to almost zero

Fig. 3.6: Pinhole formation

for tens of thousands of hours. Due to equipment limitations, only the hydrogen crossover from cathode to anode was investigated and found to decrease from 0.95% of the produced hydrogen at 60psi (0.62 MPa) to 0.87% at 150psi (1.03 MPa) at 0.1 A cm^{-2}. Qualitatively, a similar trend was observed within the NOVEL project [99], where the authors connected the decreased crossover to a decrease of uniformity. In this experiment, however, the effect was almost vanished at higher currents and is suspected to be connected to a lower water content of the Nafion® membrane at higher compression.

All the effects described here are specifically valid for inhomogeneous pressure distribution, since it highly facilitates hot spots as described in section 2.2.1.

Chapter 4

Long Term PEM WE Degradation

This chapter summarizes the findings of the experimental investigations on cell degradation. The analysis includes the effect of operating parameters, a possible link to break-in mechanisms, and reversible versus irreversible voltage increase. The results were partly published in peer-reviewed outlets or presented at conferences (see thesis outline publications [B], [C], [C3]).

4.1 Activation Phase Phenomena

An initial performance gain can be observed in many PEM WE cells. To shed some light onto the involved mechanisms, a 25 cm^2 cell of "type II" as previously described was assembled and monitored for the first 60 h of operation. For these tests, the profile shown in figure 4.1a was applied. The profile consisted of current steps of 120 s each between 0.0 and 2.0 $A\,cm^{-2}$, followed by 300 s at 1.0 $A\,cm^{-2}$, and eventually a fast cycling period with 10 s steps between 1.0 and 2.0 $A\,cm^{-2}$. The whole cycle is repeated 83 times, which is equivalent to around 60 h. EIS spectra were recorded in each cycle at the marked points at 0.2, 1.0, and 2.0 $A\,cm^{-2}$.

The potential at 2.0 $A\,cm^{-2}$ after each cycle of about 40 min is plotted in figure 4.1b. A steep drop in potential from around 2.07 to 1.88 V can be observed within the first 21 cycles. After that, the potential continues to decrease much slower down to 1.84 V after 83 cycles, which represented the end of the break-in phase. To get more insight into the cause of potential drop, figure 4.1c shows the Nyquist plot at the same operation point. The extracted LFR drops significantly within the first 30 cycles, after which it stabilize. While the LFR experiences a total decrease of around 230 $m\Omega\,cm^2$,

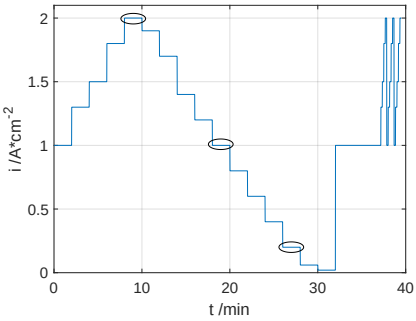

(a) Activation profile that each cell went through prior to the experiment. For the monitoring experiment, EIS measurements were taken at the marked points

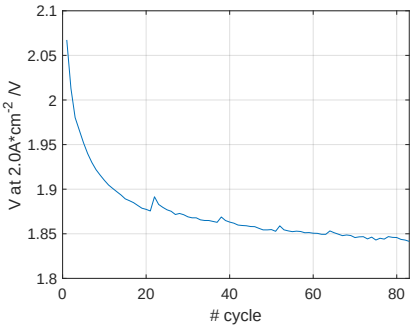

(b) Evolution of the potential at $2.0\,\mathrm{A\,cm^{-2}}$ including the reversible share during break-in

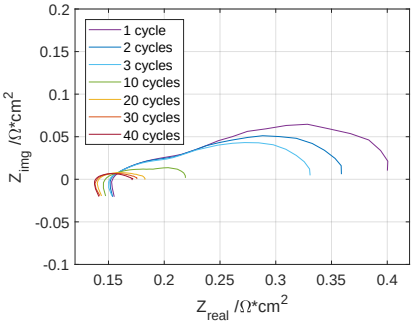

(c) Evolution of the Nyquist diagram at $2.0\,\mathrm{A\,cm^{-2}}$ during break-in

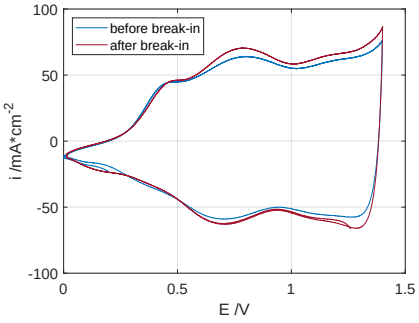

(d) Cyclic voltammogram of the anode at $50\,\mathrm{mV\,s^{-1}}$ before and after break-in

Fig. 4.1: Activation phase monitoring. Source: [C]

the HFR only decreases by around $20\,\mathrm{m\Omega\,cm^2}$. However, half of that can also be observed within the first 30 cycles. Finally, the analysis of the anode side CVs at $50\,\mathrm{mV\,s^{-1}}$ as seen in figure 4.1d indicate an increase in charge of around 6%, which is connected to CL activation.

Although a decrease in HFR has been observed in PEM FC as well [83], the there stated full humidification of the membrane as a reason is assumed to be finished before the break-in phase in the presence of liquid water. The dominant decrease in LFR together with only a moderate increase in CL activity indicates enhanced mass transport, which might be connected to a homogenization within the layers leading to more three-phase boundaries and an improved contact between MEA and PTL. This leads to the conclusion that the major processes involved in PEM WE break-in phase can be found within the MEA and its interface with the PTL.

4.2 Reversible Voltage Increase

A long-term test of around 1800 h has been carried out on the small single cell with 2.89 cm^2 active area design as previously described (section 3.1, "type I"). The cell was run at different currents and temperatures at a compression pressure of 2.30 MPa, where the feed water was recirculated at 270 mL min^{-1}. One of the main differences to most cells described in the literature is the interdigitated anodic flow field design, which was implemented to enhance performance.

In the first 504 h of operation, where the cell was held constant at 1.5 A cm^{-2} and 60 °C, the only interruption was a characterization phase every 24 h. Each characterization phase included an IV curve from 0.01 A cm^{-2} to 3.0 A cm^{-2} and EIS measurements at several operation points. During the 24 h periods the monitored cell voltage at 1.5 A cm^{-2} increased. A considerable share of that increase was recovered during the following characterization phase as shown in figure 4.2a.

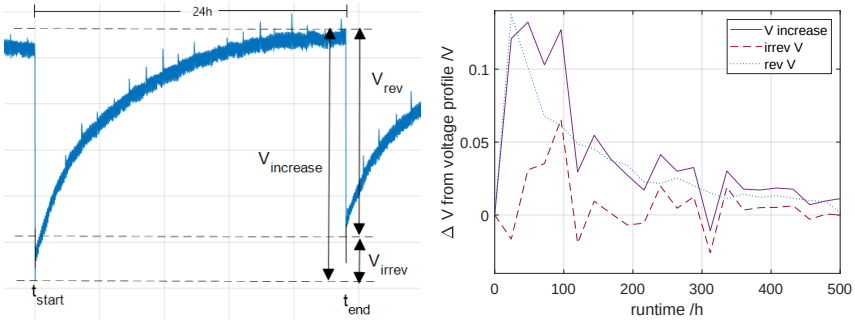

(a) Explanation of reversible (rev) and irreversible (irrev) voltage increase over 24 h

(b) Total voltage increase and the respective reversible and irreversible shares over time

Fig. 4.2: Reversible voltage increase. Source: [B]

It can be observed that the reversible voltage increase is recovered immediately when changing to a considerably different current and potential, while the voltage increase itself appears to happen slowly over time. A temporary decrease in ECSA is suspected to play a role in the observed phenomena, where oxygen bubbles block the access to the CL. This could be due to the interdigitated flow field design, where bubbles may get trapped at the end of the inlet channels instead of leaving the cell through the respective outlet channels together with the excess water. This phenomena was also observed in an experiment on a transparent cell and a CFD simulation of a circular cell with interdigitated channels [X3]. The initiation of an IV mea-

surement at low current and therefore low oxygen production may act as a flush for these bubbles, leaving a fully accessible CL behind again, which leads to a voltage drop down to the initial potential plus irreversible losses. Although the share of the reversible increase does not follow any obvious trend, the total gain during 24 h in absolute numbers is decreasing over time as shown in figure 4.2b.

4.3 Irreversible Degradation under Different Operation Modes

Two major sets of experiments were carried out on irreversible cell degradation throughout this project. Since the analysis of each can be found in detail in the attached papers [B] and [C], this chapter provides a summary of the results and includes the comparison among them. Although they both are related to PEM WE degradation, they are based on different MEAs and different setups (see section 3.1). Therefore, the results have to compared with caution. The here discussed experiments are summarized in table 4.1.

cell	#	operation mode	operation point	temperature
type I	*cc*60	constant	1.5 A cm^{-2}	60 °C
	*cyc*60	cycling	1.0 – 2.0 A cm^{-2}, 1 h hold	60 °C
	*cc*80	constant	1.5 A cm^{-2}	80 °C
type II	*cc*	constant	2.0 A cm^{-2}	80 °C
	*T*60	constant	2 V	60 °C
	*T*80	constant	2 V	80 °C
	*T*90	constant	2 V	90 °C
	cyc_{100s}	cycling	0.0 – 2.0 A cm^{-2}, 100 s hold	80 °C
	cyc_{10s}	cycling	0.0 – 2.0 A cm^{-2}, 10 s hold	80 °C
	solar	dynamic	0.0 – 2.0 A cm^{-2}, 60 s hold, solar profile	80 °C

Table 4.1: Overview of the investigated operation modes

Voltage degradation

To get a first overview, the overall voltage degradation rate at 2.0 A cm^{-2} after 500 h of operation time is illustrated in figure 4.3 for all experiments. "Type I" cells are plotted in pink, while "type II" cells are presented in blue. A selection of the most relevant values found in the literature can be seen in table 4.2 in order to contextualize this work, while a more comprehensive but

less detailed overview of reported voltage degradation rates can be found in figure 2.2.

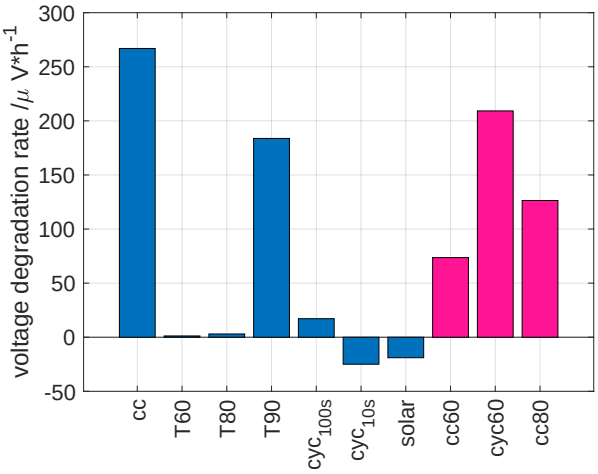

Fig. 4.3: Comparison of the mean voltage degradation rates at 2.0 A cm^{-2} after 500 h

Within the data of this work, the rates do not only differ in magnitude, but also in sign. This means, the cells operated under fast dynamics, cyc_{10s} and *solar*, actually increase in performance (i.e. decrease in voltage). Furthermore, "type I" cells generally show a higher degradation rate than "type II" cells with the exception of *cc* on "type II", which is explained later. Both types are negatively affected by an increase in temperature. However, the experiments with "type II" cells only show a moderate increase from 1.2 to 3.0 µV h^{-1} when going from 60 °C to 80 °C, while stepping to 90 °C represents a major rise to 183.8 µV h^{-1}. The numbers for 60 °C and 80 °C and the trend are similar to the literature with 5.2 and 6.2 µV h^{-1}, respectively, for a similar experiment, but dynamically operated [34]. The only voltage degradation rate found in the literature at 90 °C is also quite high with 92.5 µV h^{-1} but has very different conditions (cycling operation, Pt CL at the anode) [41]. At the same time, "type I" already shows a big increase from 74 to 126 µV h^{-1} when changing the temperature from 60 °C to 80 °C (no experiment was carried out at 90 °C). These numbers also show a difference between the cell types in this work, where the voltage degradation rate for "type II" cells is by a multiple higher. However, it should be born in mind that the operation conditions and characterization protocol were different as the figures compare constant voltage operation for "type II" with constant current operation for "type I".

Additionally, one important difference that effects degradation rates is the quality of the feed water. Although a filter was implemented into the "type I" test-stand, the nature of recirculation cannot fully ensure the quality of

18.2 MΩ · cm of the "type II" test stand feed water, where the cell was directly connected to the source, and excess water was drained after the outlet.

However, lower degradation rates of 5 and 11 µV h^{-1} for operation at 1.0 and 3.0 A cm^{-2}, respectively, were demonstrated even with water recirculation [86]. These numbers also show a negative effect of operation at elevated current of 3.0 A cm^{-2}. A similar result was obtained within another set of experiments, where cycling between 1.0 and 2.0 A cm^{-2} led to a moderate value of 6 µV h^{-1}, while cycling between 1.0 and 2.5-3.0A cm^{-2} increased the voltage degradation rate to 63 µV h^{-1} [74]. In both cases, a dwell time of 6 h was applied for each current step.

In fact, the authors in [74] observed the exact same rate for constant current operation at 2.5-3.0A cm^{-2}. This leads to the conclusion that current cycling with 6 h dwell time has no negative impact on the figure. In this work, all cycling experiments had a much lower dwell time of 10 s to 1 h. Furthermore, the anode PTL in [74] was Pt-coated, where the PTL in this work consisted of pure Ti. The effectiveness of such a coating was validated previously, where the voltage degradation rate dropped from 194 to 12 µV h^{-1} at constant operation [75]. Cycling as in experiment cyc_{100s} has an average current of 1.0 A cm^{-2}. The voltage degradation rate significantly decreases compared to constant current operation at 2.0 A cm^{-2} (*cc*). However, the test is suspected to be affected by a different degradation mechanism as explained below, and compared to *T*80, slower cycling (cyc_{100s}) has an approximately five times higher value. This indicates that cycling at 100 s has a negative effect compared to constant operation. Due to the significantly higher current for *T*80, which was operated at 2 V, and the resulting higher hydrogen output over time, the effect is specifically remarkable when comparing molar-based degradation rates. A similar trend can be observed for the "type II" cells, where the cycling period was also slow and led to an increase in rate by a factor of three compared to constant operation. However, experiment *cyc*60 was a prolongation of *cc*60 on the same MEA. Therefore, the reason behind the elevated voltage degradation rate in this case may not be exclusively connected to the operation mode, but a result of the already increased cell lifetime of 504 h at the beginning of the test. A study on the effect of cycling at moderate current densities of $\leq$2.0 A cm^{-2} found that 1000 h cycling between 0.0 and 2.0 A cm^{-2} with 6 h dwell time led to a moderate voltage degradation rate of 16 µV h^{-1}, while a shorter dwell time of 10 min increased this to 50 µV h^{-1} [76]. Although all experiments in this work have faster dynamics, the rate of the slower cycling experiment cyc_{100s} of 17 µV h^{-1} is well in line with these results. However, the trend of increasing voltage degradation with faster cycling was found opposite, as cyc_{10s} shows much less degradation and in fact has a negative rate of -25 µV h^{-1} after 500 h. The *solar* profile with a dwell time of 60 s for each current step exhibits -19 µV h^{-1} and is therefore in line with the two other dynamic operation modes.

ref	OP mode (dwell time)	i /A cm^{-2}	T /°C	feed water /mL min^{-1} (/MΩ × cm)	t /h	MEM	anode CL, PTL	cathode CL, PTL	active area /cm^2	year	/µV h^{-1}	comments
[35]	dyn	0.2…1.0	60	3.33 (18.2)	1000	N117	1.99mg cm^{-2} IrO_2, Ti	1.31mg cm^{-2} Pt black, SGL-24BC	25	2016	5.2	average 1 A cm^{-2}
	dyn	0.2…1.0	80	3.33 (18.2)	1000	N117	1.94mg cm^{-2} IrO_2, Ti	1.19mg cm^{-2} Pt black, SGL-24BC	25	2016	6.2	— ″ —
[41]	cyc (10h)	0.0…1.0	90		4000	N115	2.5mg cm^{-2} Pt unsupported, 0.58 mm Ti	2.5 mg cm^{-2} Pt/Vulcan, 0.95 mm Ti	7	2014	92.5	incl. 100h break-in, p=?
[75]	cc	2.0	80	25 (18.2)	1009	N117	2.25mg cm^{-2} IrO_2, 1.3mm Ti	0.8mg cm^{-2} Pt/C, 2 x TGP-H 120	17.64	2016	194	water supply both an and cath
	cc	2.0	80	25 (18.2)	380	N117	2.25mg cm^{-2} IrO_2, 1.3mm Pt-coated Ti	— ″ —	17.64	2016	12	— ″ —
[76]	cc	1.0	80	25 (18.2)	1009	N117	2.25mg cm^{-2} IrO_2, 1.3mm Ti	0.8mg cm^{-2} Pt/C, 2 x TGP-H 120	17.64	2017	0	water supply both an and cath
	cyc (6h)	1.0…2.0	80	25 (18.2)	1009	N117	— ″ —	— ″ —	17.64	2017	65	— ″ —
	cyc (6h)	0.0…2.0	80	25 (18.2)	1009	N117	— ″ —	— ″ —	17.64	2017	16	— ″ —
	cyc (10min)	0.0…2.0	80	25 (18.2)	1009	N117	— ″ —	— ″ —	17.64	2017	50	— ″ —
[74]	cc	≥2.5	80	25 (18.2)	2000	N117	2.2mg cm^{-2} IrO_2, 1.5mm Pt-coated Ti	0.8mg*cm.2 Pt/C, TGP-H 120 350um	17.64	2018	63	at 2.0A
	cyc (6h)	1.0…2.0	80	25 (18.2)	2000	N117	— ″ —	— ″ —	17.64	2018	6	— ″ —
	cyc (6h)	1.0…≥2.5	80	25 (18.2)	2000	N117	— ″ —	— ″ —	17.64	2018	63	— ″ —
[84]	cc	1.0	80	4, rc (18.2)	1000	E98-09S	0.4mg cm^{-2} Ir as IrO_2, Pt-coated Ti	0.1mg cm^{-2} Pt/C, C-paper	5	2017	23	excl. 200h break-in (with 23 µV h^{-1})
[86]	cc	1.0	80	4, rc (18.2)	1000	E100-09S	1.27mg cm^{-2} IrRuOx, Ti	0.1mg cm^{-2} Pt/C, C-paper	5	2017	5	excl. break-in
	cc	3.0	80	4, rc (18.2)	1000	E100-09S	— ″ —	— ″ —	5	2017	11	— ″ —
this work ("type I")	cc	1.5	60	270, rc (DI)	500	N117	2.78mg cm^{-2} Ir, IrO_2, 350um Ti	0.5mg cm^{-2} Pt/C, SGL-35DC	2.89	2017	73.6	at 2.0A
	cc	1.5	80	270, rc (DI)	500	N117	— ″ —	— ″ —	2.89	2017	126	— ″ —
	cyc (1h)	1.0…2.0	60	270, rc (DI)	500	N117	— ″ —	— ″ —	2.89	2017	209	— ″ —
this work ("type II")	cc	2.0	80	8.33 (18.2)	500	N115	2.39mg cm^{-2} IrO_2, 1mm Ti	0.86mg cm^{-2} Pt/C, SGL-28BC	25	2018	267	at 2.0A
	cv	at 2V	60	8.33 (18.2)	500	N115	2.40mg cm^{-2} IrO_2, 1mm Ti	1.18mg cm^{-2} Pt/C, SGL-28BC	25	2018	1.2	— ″ —
	cv	at 2V	80	8.33 (18.2)	500	N115	2.63mg cm^{-2} IrO_2, 1mm Ti	1.0mg cm^{-2} Pt/C, SGL-28BC	25	2018	3	— ″ —
	cv	at 2V	90	8.33 (18.2)	500	N117	2.9mg cm^{-2} IrO_2, 1mm Ti	0.96mg cm^{-2} Pt/C, SGL-28BC	25	2018	184	— ″ —
	cyc (100s)	0.0…2.0	80	8.33 (18.2)	500	N115	2.57mg cm^{-2} IrO_2, 1mm Ti	1.08mg cm^{-2} Pt/C, SGL-28BC	25	2018	17	— ″ —
	cyc (10s)	0.0…2.0	80	8.33 (18.2)	500	N115	1.29mg cm^{-2} IrO_2, 1mm Ti	2.27mg cm^{-2} Pt/C, SGL-28BC	25	2018	-25	— ″ —
	dyn	0.0…2.0	80	8.33 (18.2)	500	N115	2.57mg cm^{-2} IrO_2, 1mm Ti	1.11mg cm^{-2} Pt/C, SGL-28BC	25	2018	-19	— ″ —

Table 4.2: Extract of the voltage increase rates literature review. If not otherwise annotated, gas and liquid pressure was atmospheric. OP = operation, cc = constant current, cv = constant voltage, cyc = cycling, dyn = dynamic, rc = recirculated

The constant current experiment *cc* ("type II") seems to be an outlier in the set of experiments with a significantly higher voltage degradation rate of $266.9\,\mu V\,h^{-1}$. Although a similar result can be found in the literature [76], where constant operation at $2.0\,A\,cm^{-2}$ exhibits the by far highest degradation of $194\,\mu V\,h^{-1}$ compared to cycling operation, the reason behind the extreme difference to experiment *T*80 at the same temperature in this work can only be speculated. While the potentials are of similar magnitude, *T*80 even exhibits a higher current, and the other settings are exactly the same. The only difference lies in the assembly of the cell, since the cell for the constant current test was attempted to be used for an investigation of the evolution of the internal contact resistance. For that, two thin gold strips were inserted into the assembly as shown in figure 4.4. Eventually, the internal resistance could not be certainly measured with the method, but the experiment was continued. The inserted gold strips may have affected pressure distribution, gas leakage, or spread impurities. Therefore, experiment *cc* at constant current may be exposed to other parameters than the operation mode that increased the degradation rate.

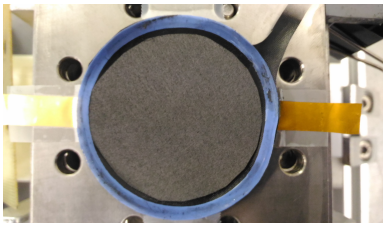

Fig. 4.4: Cell design to experimentally monitor contact resistances ("type II" cell)

To put the obtained numbers into a financial perspective, the hydrogen production cost due to electricity consumption can be calculated. A simplified calculation shows that the *T*80 cell uses $48.24\,kW\,kg^{-1}$ for hydrogen production at its beginning of life. With the measured voltage degradation rate, the specific electricity consumption increases by roughly $0.8\,kW\,kg^{-1}$ or 1.7% after 10 000 h of operation. Therefore, an economical EoL seems to not be the most severe issue.

Impedance measurements

To shed more light on the causes of degradation, the evolution of HFR normalized to its initial value is shown in figure 4.5. The evolution of the HFR reveals that fast dynamic operation as in experiments cyc_{10s} and *solar* decreases ohmic resistance. This explains the overall performance gain as seen from the voltage degradation rates at $2.0\,A\,cm^{-2}$, since ohmic contributions are most pronounced at elevated currents. The decrease may be connected to

a prolonged break-in phase due to the similar nature of the operation mode (fast switch between currents and potentials), which enhances the formation of three-phase boundaries and improves the contact between MEA and PTL. The positive effect of dynamic operation on HFR evolution is not seen when cycling with lower frequency as in cyc_{100s}, as it exhibits a similar increase as operation at 2 V ($T80$).

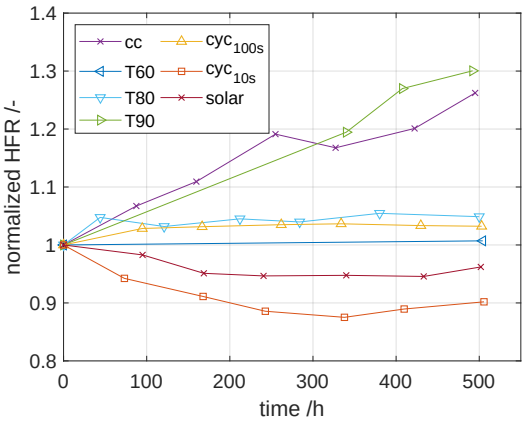

Fig. 4.5: Evolution of HFR relative to its initial value as extracted from EIS measurements over time. The legends refer to the experiments as presented in 4.1. Source: [C]

Furthermore, figure 4.5 shows the negative impact of temperature on the HFR increase, where the highest increase can be observed at the highest temperature in experiment $T90$. While almost no change can be observed for $T60$, $T80$ shows a moderate gain. The increase in general is connected to a passivation layer that forms on the anode Ti-PTL, which is enhanced at elevated temperature [61].

While Ti passivation may increase the ohmic resistance, other processes such as membrane thinning decrease it. Each cell is objected to different processes, which may be dominant over each other depending on the operation mode. In order to separate these processes, figure 4.6 shows their impact on voltage degradation. It is assumed that three previously observed mechanisms compete against each other: Membrane thinning and structural adjustments between MEA and PTL (positive impact), and Ti passivation (negative impact) [34, 75]. The figure reveals many general trends and furthermore gives insight into the dominant degradation phenomena.

By comparing the total voltage degradation rate as extracted from the IV curves to the share of purely ohmic contributions, the nature of the dominant mechanism can be identified. In all experiments, ohmic processes are by far dominating, in some cases exceeding the measured voltage degradation rate as for example observed for $T90$. That implies an improvement in non-ohmic

phenomena such as catalyst activity over time or the presence of reversible processes and is conformed by the evolution of LFR as described below.

Furthermore, positive values for the ohmic degradation rate indicate that Ti passivation is dominant over the two others. This is the case for all experiments except fast dynamic operation (cyc_{10s} and *solar*). Membrane thinning was quantified through SEM images and its impact on the voltage degradation rate calculated assuming a linear thinning trend over time. When correcting the ohmic degradation rate by this factor, the joint impact of Ti passivation and structural adjustments can be seen. Ti passivation is found to be dominant over structural adjustments in all experiments except for fast cycling as in cyc_{10s}, while the *solar* profile was not terminated at the point of writing and therefore no data on membrane thinning was available.

As suspected from the evolution of the HFR, the results confirm that passivation is highly accelerated by temperature. The step from 80 °C to 90 °C induces an increase of the voltage degradation rate due to non-membrane related ohmic processes by a factor of 4, where the step from 60 °C to 80 °C roughly doubles the rate.

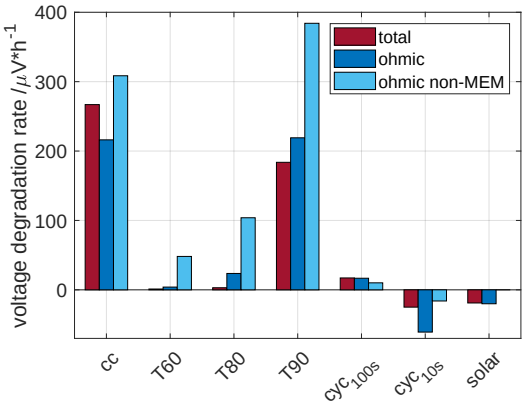

Fig. 4.6: Voltage degradation rates at 2.0 A cm^{-2} as calculated from the IV curves (total), from the HFR (ohmic), and corrected for membrane thinning (ohmic non-MEM)

While the ohmic resistance (HFR) is mostly connected to the membrane and contacts, the polarization resistance (LFR) may provide insight into other components and phenomena. Therefore, figure 4.7 shows the difference between LFR and HFR normalized to its initial value. The difference is taken in order to correct for the purely ohmic contribution to the polarization resistance. It can be seen that fast cycling and dynamic operation have a positive impact on the CL or mass transport related phenomena as the two experiments cyc_{10s} and *solar* have a decrease in resistance. As shown later, it is related to a fluoride loss within the catalyst layer. Additionally, cycling at

100 s as in experiment cyc_{100s} also shows a decrease of up to 20%, implying a positive effect of cycling operation, while constant operation during experiment *cc* leads to a 20% increase.

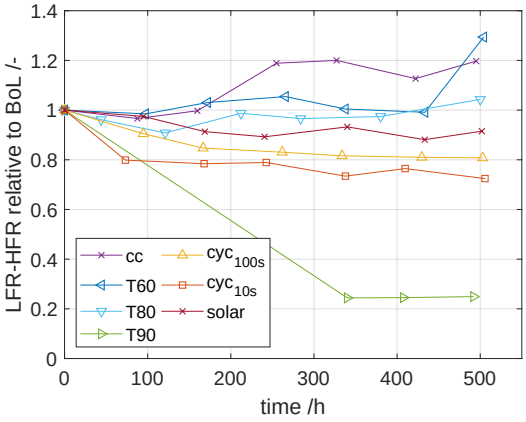

Fig. 4.7: Evolution of the difference between HFR and LFR relative to its initial value as extracted from EIS measurements

However, most remarkable is the effect of temperature, where a sharp drop by almost 80% can be observed for experiment *T*90. On the other hand, experiments *T*60 and *T*80 remain almost constant. An increase in polarization resistance has been connected to deactivation of the anode CL [56, 86]. The general trend here to not observe severe CL degradation can be explained by the high anode catalyst loading, which supposedly increases CL durability [19]. The considerable decrease in LFR as seen for *T*90 however indicates that another phenomenon is involved, as no significant improvement in CL performance can be observed from the voltammograms. Possibly, a reversible mechanism has built up up the long first period of 340 h, which was recovered during the second characterization. The first period was much longer than for all other tests (<100 h) due to laboratory availability, which may explain the difference.

4.3.1 Cell Degradation under Dynamic Operation

As it represents a dynamic operation scenario, the degradation phenomena of experiment cyc_{10s} are presented here in more detail. Firstly, the change in resistances as extracted from EIS in absolute numbers over time is shown in figure 4.8a.

The agreement of LFR and IV curve slope supports the integrity of data. Furthermore, the non-linear shape of the decrease of both HFR and the difference between LFR and HFR can be seen more clearly. Both reach a more or

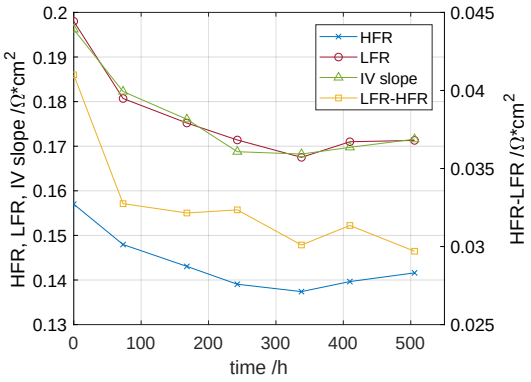

(a) Evolution of resistances over time for experiment cyc_{10s}. HFR, LFR, and their difference from EIS measurements, IV slope from polarization curves

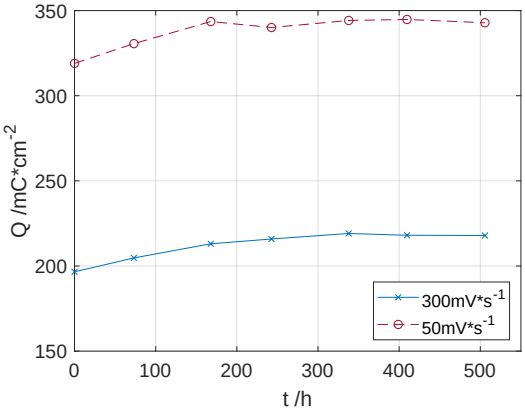

(b) Evolution of charge at the anode CL as extracted from CV diagrams at 50 mV s^{-1} and 300 mV s^{-1} over time for experiment cyc_{10s}

Fig. 4.8: Degradation of the cell exposed to high frequency cycling (experiment cyc_{10s}). Source: [C]

less steady value after around 338 h. The decreasing ohmic-corrected polarization resistance implies an increase in catalytic activity, or improved mass transport characteristics. In fact, when looking at the anodic CV in figure 4.8b, a gain in charge can be observed. A degradation of the CL is therefore assumed to cause an improvement instead of contributing to overall cell degradation.

To see the evolution of the voltage over time, figure 4.9 shows the voltage degradation rates with respect to the previous period and the BoL. This means, the last point in figure 4.9a refers to the period between 410 h and 506 h, where the last point in figure 4.9b includes the whole operation be-

tween 0 h and 506 h. It can be seen, that the performance at a current density of 2.0 A cm^{-2} increases until 338 h, after which it decreases, while lower currents of <1 A cm^{-2} experience a decrease in performance throughout the whole experiment. This is in line with the previously described decrease of HFR, which is connected to the ohmic overpotential and therefore more pronounced at higher currents. Also the non-linear shape of the change in HFR over time can be found when looking at figure 4.9b. The data suggests that the dominant degradation mechanism for this operation mode changes from being adjustments within the CL and membrane thinning, to Ti passivation at around 338 h. However, the overall change in performance after 500 h is still positive. Finally, the steady voltage degradation of around 50 µV h^{-1} at current densities <0.5 A cm^{-2} indicates that thermodynamic processes degrade constantly.

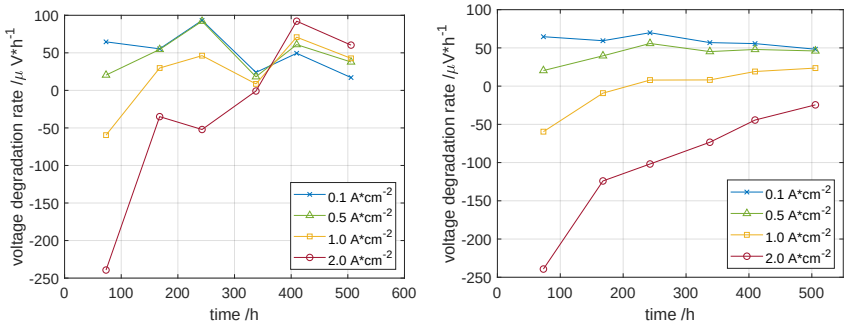

(a) voltage degradation rates relative to the last period

(b) voltage degradation rates relative to the beginning of life. Source: [C]

Fig. 4.9: Evolution of voltage degradation rates at various current densities over time for fast cycling operation (experiment cyc_{10s})

Chapter 5

Membrane Degradation Through Fluoride Emission

With respect to the research objective to develop a lifetime model, this chapter summarizes the work on membrane degradation. Although all components may degrade over time, irreversible membrane thinning through radical attack is the most severe mechanism and has been identified to be lifetime limiting [32]. The major issue is an increased gas crossover due to a lower thickness, which may create hazardous gas mixtures within the explosion limits. The outcomes are published in [C], [D], and [C2] (see thesis outline).

5.1 Experimental Investigation on Fluoride Emission

State of the art ionomers for PEM WE membranes are based on perfluorosulfonic acid (PFSA) and are for example known under the brand names Nafion® (DuPont) or Aquivion® (Solvay). Commonly, one of their main components is fluorine (F). Except for the binder within the catalyst layers, fluorine can usually not be found in other components of a PEM WE cell. Therefore, traces of fluoride (the negatively charged ion of fluorine) leaving the cell outlets are an indication of ionomer degradation. This approach is widely applied within PEM FC research [49, 60] and can also be observed for PEM WE [34, 59].

In this experiment, the fluoride concentration within the effluent water at the anode and cathode outlets was monitored over time for all seven experiments on "type II" cells as shown in table 4.1. On average, the anode showed less than 40% of the fluoride emission at the cathode, which is in line with previous findings in the literature [34]. The FER at the cathode outlet for all

experiments over time can be seen in figure 5.1a, where figure 5.1b shows their average values. While experiment *cc* under constant current shows a constant FER over time, fast cycling as in experiment cyc_{10s} has a high peak between 200 and 300 h, *T*90 follows an increasing trend and all other experiments show a decline in FER over time. To see the overall influence of the operation mode more clearly, average values over the whole test period of 500 h are calculated.

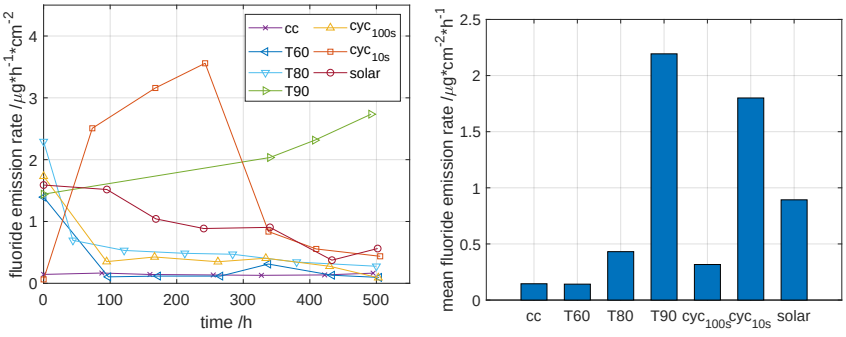

(a) Fluoride emission rates over time. Adjusted from: [C]

(b) Averaged fluoride emission rates

Fig. 5.1: Comparison of in-situ fluoride emission rates at 0.3 A cm^{-2} at the cathode outlet for different operation modes

The comparison reveals that operation at high temperature is unfavorable, especially when exceeding 80 °C. The fluoride emission rates of 0.14, 0.43, and 2.19 µg cm^{-2} h^{-1} for 60 °C, 80 °C, and 90 °C, respectively, suggest a non-linear trend. The factor of roughly 3 between 60 °C and 80 °C is in good agreement with the literature [34, 53]. The values reported by [34] at a comparable current density are generally higher by a factor of around 3. The reason for that might be the different applied current profile and different run-time at which the measurements were taken, of which both may have an influence on the emission rate as shown above.

Moreover, cycling at 100 s dwell time as in cyc_{100s} does not affect the FER considerably compared to *T*80, while faster dynamics as in cyc_{10s} and *solar* do show an increase by a factor of roughly 4.2 and 2, respectively. This suggests a higher impact of fast dynamic operation on ionomer emission, which may be connected to membrane thinning or CL binder loss. In fact, the observed fluoride emission together with the decrease in HFR but only moderate membrane thinning rate points at the cathode CL as a source of the fluoride for fast cycling (cyc_{10s}). The cell voltage decrease indicates that the fluoride loss improves CL performance. No membrane thinning data was available for the *solar* profile experiment as the test was still on-going at the

time of writing.

5.1.1 Impact of Iron and Hydrogen Peroxide

In order to create a controlled environment, the impact of iron (specifically Fe^{2+}) and hydrogen peroxide (H_2O_2) was investigated in an ex-situ experimental set-up. Eleven flasks made of polypropylene were filled with 100 mL solution with defined initial species concentrations according to table 5.1. Five pieces of Nafion® 115 with a total area of 25 cm^2 were immersed in each of the flasks, which were kept at 80 °C for 72 h. In the meanwhile, the fluoride concentration was determined through an ion selective electrode at seven points of time. The measurements are shown in figure 5.2a.

#	$[Fe^{2+}]$ /ppm	$[H_2O_2]$ /wt%	$\frac{[Fe^{2+}]}{[H_2O_2]}$ $/M \cdot M^{-1}$
1	0	0	-
2	1	0	-
3	1	0.003	$2.03 \cdot 10^{-2}$
4	1	0.03	$2.03 \cdot 10^{-3}$
5	1	0.3	$2.03 \cdot 10^{-4}$
6	1	3	$2.03 \cdot 10^{-5}$
7	1	30	$2.03 \cdot 10^{-6}$
8	0	3	-
9	0.1	3	$2.03 \cdot 10^{-6}$
10	10	3	$2.03 \cdot 10^{-4}$
11	20	3	$4.06 \cdot 10^{-4}$

Table 5.1: Experimental matrix for the ex-situ Fenton test, where all concentrations are stated as initial values. Experiment #6 is the baseline test

It can be seen in figures 5.2a and 5.2b that for the two experiments with the highest initial Fe^{2+} concentration of 10 ppm and 20 ppm (#10 and #11), H_2O_2 becomes limiting and the fluoride emission is effectively stopped after around 23 h. Otherwise, the data suggests that a higher Fe^{2+} concentration negatively affects membrane degradation within the investigated range. Furthermore, a fluoride concentration close to zero is observed for experiments with no H_2O_2 initially (#1 and #2). An increase in initial H_2O_2 concentration leads to an increase in fluoride emission until around 3wt%, after which H_2O_2 seems to lower membrane degradation as seen in figure 5.2c. This behavior was not expected, as H_2O_2 is the driving force behind radical formation and therefore ionomer attack. A possible reason is the presence of a competing reaction, that depletes $HO^{\bullet}$ radicals at high H_2O_2 concentrations. However, the result should be confirmed by further experiments.

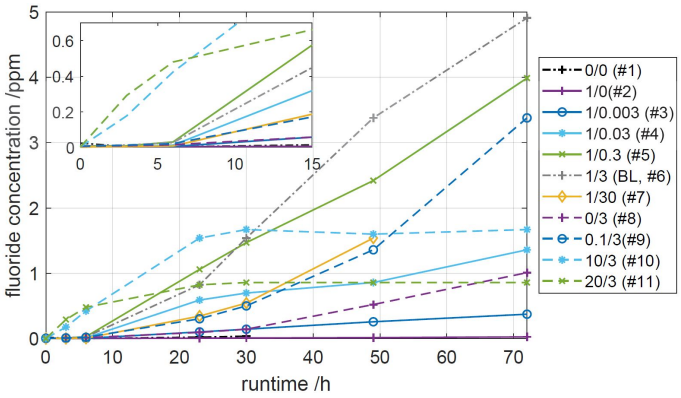

(a) Evolution of fluoride concentration for the investigated experiments. The legend refers to the initial concentrations as $[Fe^{2+}]$ in ppm/$[H_2O_2]$ in wt%; BL = baseline test

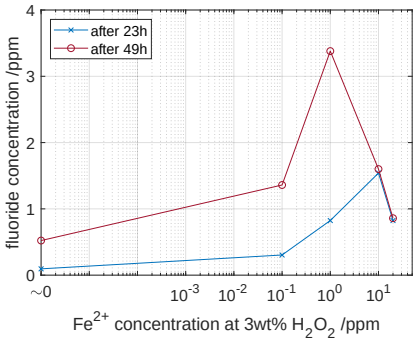

(b) Influence of initial Fe^{2+} concentration on fluoride concentration at different points of time

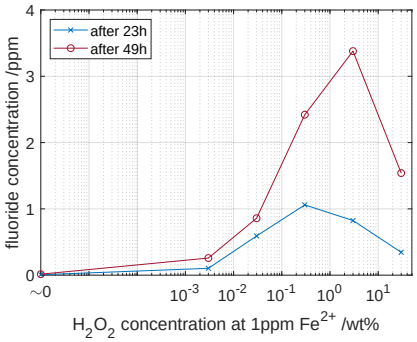

(c) Influence of initial H_2O_2 concentration on fluoride concentration at different points of time

Fig. 5.2: Fluoride emission over time as a function of initial Fe^{2+} and H_2O_2 concentrations. Source: [D]

5.2 Fenton Model Approach

Based on the experimental findings in section 5.1, the degradation mechanism as illustrated in figure 5.3 is proposed. It has been reported in the literature [32], but a full understanding, let alone a full validation, has not yet been achieved.

As a significant amount of F^- was detected within the effluent water at the cathode outlet for the in-situ experiment, it is assumed that it stems from the ionomer close to the cathode CL. Research on PEM FC suggests that F^- is released from the Nafion® structure in the presence of weak carboxylic acid

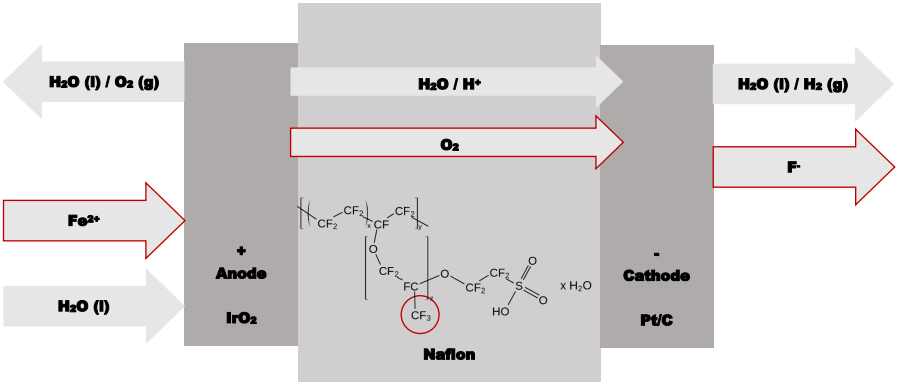

Fig. 5.3: Illustration of the proposed degradation mechanism. Source: [D]

end-groups (-COOH), which are attacked by hydroxyl radicals ($HO^{\bullet}$) [82]. In principle, hydrogen-peroxide (H_2O_2) is formed through the oxygen reduction reaction (ORR) of diffused oxygen at the cathode electrode. H_2O_2 as a precursor for the reaction mechanism is then involved in several reactions, which generate the highly reactive $HO^{\bullet}$ radicals. This is in line with the experimental ex-situ data, where the absence of initial H_2O_2 prevents fluoride emission as seen in figure 5.2a. The reaction is strongly catalyzed by the presence of Fe^{2+} even in very low concentrations in the ppm range and known as the Fenton reaction:

$$H_2O_2 + Fe^{2+} \longrightarrow Fe^{3+} + HO^{\bullet} + HO^{-} \tag{5.1}$$

The source of H_2O_2 may be explained by the ORR within the cathode CL, where the oxygen is assumed to originate from the anode, but is subject to dispute. Formation of H_2O_2 as:

$$O_2 + 2\,H^{+} + 2\,e^{-} \longrightarrow H_2O_2 \tag{5.2}$$

has experimentally been shown to be favorable compared to formation of H_2O through recombination with protons under the PEM WE cathode environment [78]. Finally, the Fe^{2+} that serves as a catalyst is implemented as an influx within contaminated feed water. The source of Fe^{2+} is often mentioned to be stainless steel components from the cell and the balance of plant. However, a small side experiment showed fluoride emission, where this source was excluded. In this set-up, all fluids were transported in plastic tubes and

the cell components consisted exclusively of titanium. The measured fluoride emission rates were in the same order of magnitude as on a set up including stainless steel pipes. The hypothesis is that either Fe^{2+} comes from imperfectly purified feed water or another metal cation catalyzes the reaction in the absence of Fe^{2+}. That is in line with the findings from the ex-situ experiment, where the test without initial Fe^{2+} and 3wt-% H_2O_2 still showed fluoride emission. As it is assumed that a real PEM WE system would include stainless steel components as a potential Fe^{2+} source, the reaction system as shown in table 5.2 is considered for the simulation work. Reaction 1 is the H_2O_2 production, reaction 14 the membrane attack reaction, and reactions 2-13 describe the radical formation and decomposition. No data on the temperature effect on reactions 7 and 14 was found in the literature. Therefore, reaction 7 was implemented with a constant reaction rate constant, while the results of the ex-situ experiment described in section 5.1.1 were used to fit reaction 14 to the Arrhenius equation as described in the following.

#	Reaction		E_{act} /kJ mol^{-1}	A /s^{-1}
1	$O_2 + 2\,H^+$	$\longrightarrow H_2O_2$	42.45 [17]	-
2	H_2O_2	$\longrightarrow 2\,HO^\bullet$	200	$1.09 \cdot 10^{13}$
3	$H_2O_2 + Fe^{2+}$	$\longrightarrow Fe^{3+} + HO^\bullet + HO^-$	35.4	$1.03 \cdot 10^{08}$
4	$H_2O_2 + Fe^{3+}$	$\longrightarrow Fe^{2+} + HOO^\bullet + H^+$	126	$8.31 \cdot 10^{18}$
5	$HO^\bullet + Fe^{2+}$	$\longrightarrow HO^- + Fe^{3+}$	9	$8.68 \cdot 10^{09}$
6	$HO^\bullet + H_2O_2$	$\longrightarrow HOO^\bullet + H_2O$	14	$7.66 \cdot 10^{09}$
7	$HO^\bullet + O_2$	$\longrightarrow HOO^\bullet + H_2O$	-	-
8	$HOO^\bullet + Fe^{3+}$	$\longrightarrow Fe^{2+} + O_2 + H^+$	33	$1.21 \cdot 10^{10}$
9	$HOO^\bullet + Fe^{2+} + H^+$	$\longrightarrow Fe^{3+} + H_2O_2$	42	$2.74 \cdot 10^{13}$
10	$HOO^\bullet + H_2O_2$	$\longrightarrow HO^\bullet + H_2O + O_2$	30	$5.41 \cdot 10^{05}$
11	$2\,HOO^\bullet$	$\longrightarrow H_2O_2 + O_2$	20.6	$3.5 \cdot 10^{09}$
12	$HO^\bullet + HO^\bullet$	$\longrightarrow H_2O_2$	7.9	$1.31 \cdot 10^{11}$
13	$HOO^\bullet + HO^\bullet$	$\longrightarrow H_2O + O_2$	14.2	$2.09 \cdot 10^{12}$
14	$HO^\bullet + R_f - CF_2 - COOH$	$\longrightarrow$ products	6.5*	$1.35 \cdot 10^{07}$*

Table 5.2: Simulated reaction system considered in this study. The data is based on [17] and [40], with the exception of reaction 14 (marked with *), whose implementation is further described in the text. Source: [D]

The model was utilized to simulate the ex-situ behavior, where the differences in parameters compared to the in-situ case are presented in table 5.3. Figure 5.4 summarizes the experimentally determined fluoride concentration for all tests and compares them to the simulated value after 72 h.

The figure reveals the strengths and limitations of the model. Generally, it follows the trends for H_2O_2 and Fe^{2+} fairly well as can be seen for experiments #2 to #6, but underestimates the fluoride emission. Moreover, the sharp drop in fluoride release at high H_2O_2 concentration (#7) is not cap-

	ex-situ	in-situ
i	$i = 0$	$i = set$
O_2	$V_{O_2} = 0$	$V_{O_2} = f(i)$
	$[O_2]_{ini} = p_{O_2} \cdot H_{O2}(T)$	$[O_2]_{eq} = f(OP)$
H_2O_2	$V_{H_2O_2} = 0$	$V_{H_2O_2} = 0$
	$[H_2O_2]_{ini} = set$	$[H_2O_2]_{eq} = f(OP)$
Fe^{2+}	$V_{Fe^{2+}} = 0$	$V_{Fe^{2+}} = set$
	$[Fe^{2+}]_{ini} = set$	$[Fe^{2+}]_{eq} = f(OP)$

Table 5.3: Modeling conditions for ex-situ and in-situ simulations. Square brackets indicate concentrations, while V_s = influx of species s, p_{O_2} = partial pressure of oxygen, $H_{O2}(T)$ = Henry's constant, OP = operation parameters, ini = initial

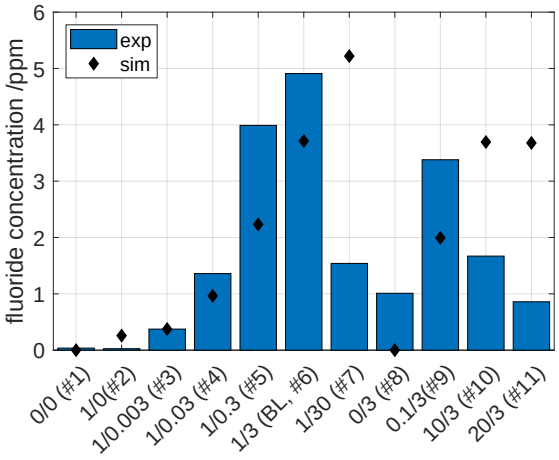

Fig. 5.4: Ex-situ fluoride concentration for all experiments (bars) compared to their respective simulation (⧫). The labels refer to the initial concentrations as $[Fe^{2+}]/[H_2O_2]$, where BL = baseline test. Source: [D]

tured, where the model instead predicts a further increase. The simulations exclude reaction 6 to be dominant over reaction 14 even at high H_2O_2 concentrations, which would have explained the depletion of $HO^{\bullet}$ radicals. However, the simulations in the absence of H_2O_2 in the beginning of test (#1 and #2) lead to almost no fluoride emission, showing good agreement with the experiment. The small value for experiment #2 is a result of H_2O_2 formation through initially dissolved oxygen and is fairly well captured by the model. The trend for high Fe^{2+} concentrations is not fully captured. Although the model correctly predicts H_2O_2 as being the limiting factor, the limitation is already visible at 1ppm instead of 10ppm, while the total fluoride emission is over-predicted. Lastly, experiment #8 is predicted to have almost no fluoride emission due to the lack of a catalyst. However, the measurement does show

a considerable amount of fluoride in the solution. As described above, the reason might be the presence of a different catalyst material, which is not implemented in the model. In this case, it could be other metal impurities from the membrane manufacturing, as the membranes did not undergo any cleaning process such as a break-in for the in-situ cells. Experiments #3 to #6 and #9, all at 80 °C, were used to implement the reaction rate constant of reaction 14 as a function of temperature by fitting them to the Arrhenius equation together with the literature value found at room temperature [17].

5.2.1 In-situ Effect of Operation Conditions

With the previously described reaction system implemented into a simple performance model, an operational cell was simulated to investigate the effect of various conditions. However, a real cell differs from the ex-situ experiments in points such as presence and type of a catalyst, applied potential, and pH value. The found reaction rates are reported to be valid for low pH values [45], which are assumed within an operating electrolysis cell [16, 54]. As the main objective of this work is to investigate the effect of dynamic operation, the current was chosen as the input parameter to be simulated. The current setpoint determines the water velocity through the cell in the direction from anode to cathode. Therefore, oxygen crossover as well as outflux of species is highly affected by the current. The effect of input current density on oxygen permeation and FER at different temperatures is shown in figure 5.5.

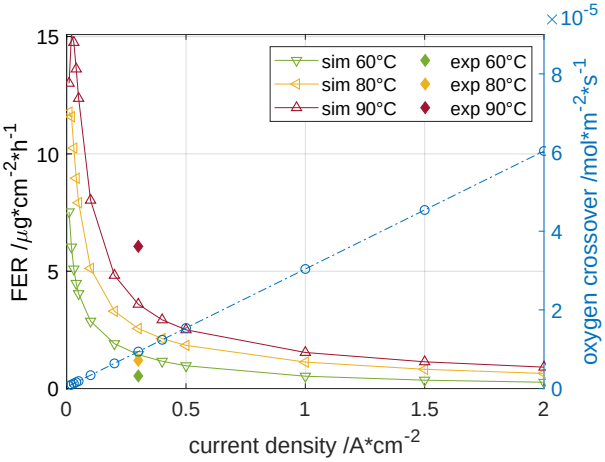

Fig. 5.5: Simulated influence of current density on oxygen crossover from anode to cathode (right axis) and FER (left axis). Experimental FER at 0.3 A cm^{-2} are shown as measured in-situ. Source: [D]

The figure shows that operation at higher current leads to a decrease in FER. Figure 5.6 reveals the cause, as it presents the most important reactions together with the $HO^{\bullet}$ radical concentration as a function of current at 80 °C. Reactive end-groups are considered to be present in constant concentration of 200mM and therefore do not change the kinetics of the reaction system. As implied by the membrane attack reaction 14, the concentration of $HO^{\bullet}$ radicals therefore dictates fluoride emission. The dependence can be deduced from the figure as both decrease with increasing current. Reaction 3 is crucial for radical generation through the Fenton reaction and appears to be negatively affected by current. Additionally, reaction 6 and 7 deplete $HO^{\bullet}$ radicals and become dominant over the membrane attack reaction 14 at high H_2O_2 and O_2 concentrations, which are caused by higher O_2 crossover at higher current. This explains the lower fluoride emission at higher current, which therefore is beneficial in terms of lifetime.

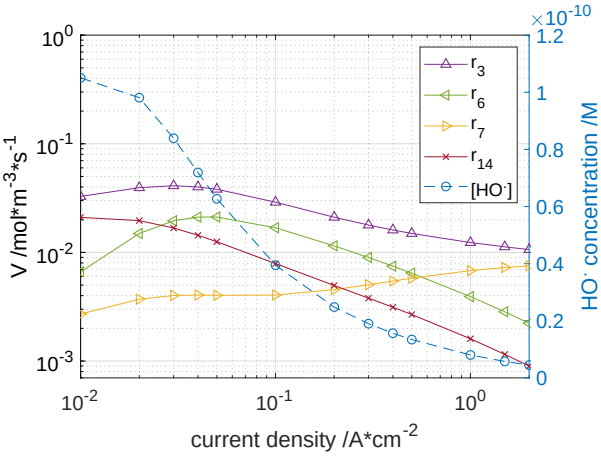

Fig. 5.6: Simulated impact of current density on the most important reactions rates and the $HO^{\bullet}$ concentration at 80 °C. Source: [D]

Furthermore, the FER increases with temperature as seen in figure 5.5. As overall performance increases with temperature, this parameter is important for the optimization of PEM WE operation. However, the effect of temperature is underestimated for 90 °C and overestimated for 80 °C and 60 °C compared to the measured in-situ values. As oxygen crossover and water velocity are implemented as temperature-independent in the model, the reason for the discrepancies may lie within these relationships.

5.2.2 Membrane Thinning through Fluoride Emission

A loss in fluoride causes a thinning of the membrane over time, whose rate can be expressed as in equation 5.3 [18]:

$$\frac{d\delta_{mem}}{dt} = \nu_{F,PFSA} \cdot FER \cdot f_{F,loss} \tag{5.3}$$

where $\nu_{F,PFSA}$ is the partial specific ionomer volume, FER the fluoride emission rate, and $f_{F,loss}$ a fit parameter for the model implementation. The fit parameter takes into account, that not all fluoride ions are captured within the effluent water and that membrane fractions may leave the cell as fluorine, which cannot be detected in the chosen experimental approach. The partial specific volume of the ionomer per unit fluorine can be expressed as in equation 5.4 [18]:

$$\nu_{F,PFSA} = \frac{1}{\omega_F \cdot \rho_{PFSA}} \tag{5.4}$$

where ω_F is the mass fraction of fluorine within the ionomer, and ρ_{PFSA} is its density. This equation sets a relationship between emitted fluoride and lost membrane volume. The total fluoride emission experimentally determined by ionic chromatography analysis for all operation modes is shown in figure 5.7 together with the respective loss of membrane thickness as extracted from SEM images after the tests were terminated.

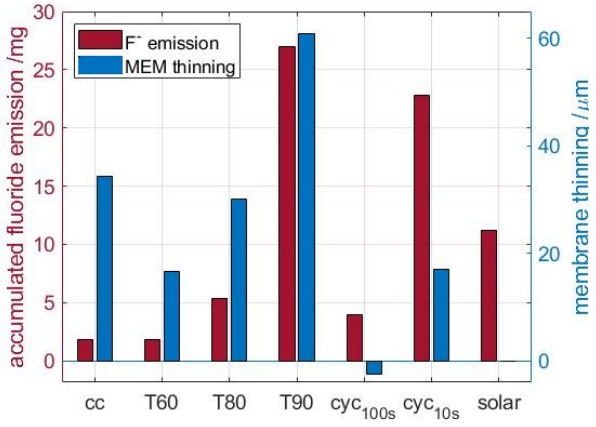

Fig. 5.7: Experimental in-situ fluoride emission accumulated over time together with total membrane thinning at EoL as extracted from SEM images. Source: [C]

The effect of temperature on membrane thinning seems to be coherent with the measured fluoride loss, where the steps between 60 °C and 80 °C,

and 80 °C and 90 °C each roughly doubles the loss in thickness. When it comes to cycling operation, however, the results do not represent the trends from the fluoride emission. While a slight increase in thickness of around 2.5 µm was seen during 100 s current cycling (cyc_{100s}), a thinning of 17 µm was seen for the faster cycling at 10 s (cyc_{10s}). The *solar* profile experiment was not terminated at the point of analysis and therefore has no SEM data available. An increase in thickness in physically impossible and must therefore be connected to inaccuracies in the method. That could be an effect of water uptake, or the limitation of SEM analysis for localized degradation. All values are based on several measurements on one 1 cm sample taken from the middle of the MEA. Local degradation, or in this case high local durability can distort conclusions on overall thinning. However, cyc_{10s}, which was operated at 80 °C, shows less thinning compared to *T*80, while having a higher fluoride emission. At the same time, a decrease in HFR was observed as seen in 4.8a. A feasible explanation could be that the fluoride originates from the CL, or that the attack mechanism is shifted to one that releases more fluorine instead of its ion fluoride. To validate or rule these options out, further experiments are necessary.

With the available data, the measured membrane thinning as a function of temperature is compared to a simulation in figure 5.8. The results show a good agreement until 80 °C and an underestimation of the thinning in the model at 90 °C. This is a result of the above mentioned underestimation of FER at 90 °C and might be connected to the temperature dependence of reaction 14 as well as oxygen crossover. Furthermore, for the simulation it is assumed that all captured fluoride originates from the membrane and therefore contributes to its thinning. The fitting factor $f_{F,loss}$ would change in order to account for fluoride originating from the CL.

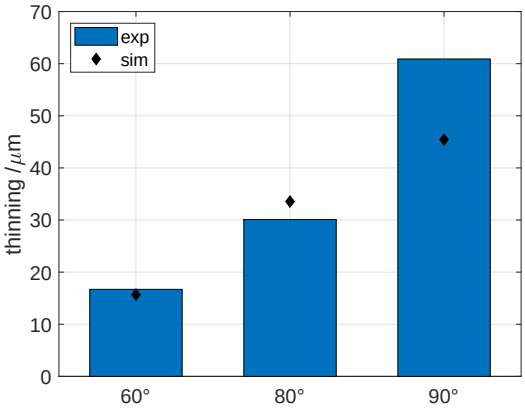

Fig. 5.8: Membrane thinning after 500 h at different temperatures as extracted from SEM images compared to simulation

Chapter 6

Final Remarks

In this project, PEM WE was investigated with special focus on its degradation under dynamic operation. An experimental approach combined with numerical modeling was followed with a focus on single cells to obtain a better understanding of different degradation mechanisms. This chapter firstly summarizes the main outcomes and contributions of this work according to the defined objectives of the project, and secondly presents a future perspective on the topic.

6.1 Conclusion

The impact of cell compression was investigated in-situ, ex-situ, and through a computational performance model on a 2.89 cm^2 single cell. It was experimentally found that high pressure operation decreases the total ohmic losses due to improved contacts. The simulation further revealed a share of roughly one-third to two-thirds between the contact resistances and the membrane resistance, where the current distributors have been found to be responsible for a considerable share of the total contact resistance through an ex-situ experiment. However, compared to the ohmic overpotential, the activation overpotential remains dominant throughout the whole investigated compression range even at elevated currents, and simulations suggest an optimum compression of around 1.5 MPa for the maximum apparent exchange current density. Furthermore, excessive compression may facilitate the formation of hot spots and pinholes.

Concerning degradation, long-term experiments on 25 cm^2 single cells revealed that high temperature operation is beneficial in terms of performance, but negatively affects durability, especially at temperatures above 80 °C. This is due to accelerated membrane thinning, which roughly doubles between 60 °C and 80 °C, and 80 °C and 90 °C, respectively. Furthermore, the total

ohmic cell resistance increases over time due to titanium passivation, where the rate is likewise highly influenced by the temperature. To enable operation above 80 °C and benefit from the efficiency improvement, mitigation strategies for both anode porous transport layer and membrane have to be implemented. The porous transport layer may be platinum-coated, which has to experience a drop in cost for a commercial implementation. The membrane may be stabilized against chemical attack. This can be done through adjustments in the chemical structure by reducing the amount of reactive end groups, which represent the point of attack for hydroxyl radicals.

Economically, the measured voltage degradation rate for operation at 80 °C would increase the specific energy cost for hydrogen production by $0.8\,\mathrm{kW\,h\,kg^{-1}}$ over 10 000 h, which corresponds to a 1.7% increase compared to its initial value. This is considered to be within acceptable range for commercial products. Therefore, a technical or safety-related end of life is considered more critical rather than an economical one.

It was furthermore experimentally found that interdigitated flow channels exhibit a high reversible share of overall voltage increase. The potential cause are trapped oxygen bubbles in the inlet channels that hinder access to the active sites. A sudden change in current and potential clears the reversible voltage increase, which indicates a positive effect of dynamic operation on reversible degradation.

Furthermore, irreversible voltage degradation has also been found to decrease at dynamic operation with a dwell time of 10 s in a set-up with parallel flow field channels. This is mostly due to a decrease in ohmic resistance within the first 350 h of operation of around 12%, while constant operation showed an increase. At the same time, fluoride emission is higher at dynamic operation, while no significant difference for membrane thinning was observed. Therefore, the ionomer within the catalyst layer is suspected to experience the fluoride loss, which improves performance due to an increase in three phase boundaries. However, when fluoride loss exceeds a certain threshold, it is expected to reverse the positive effect into a negative one, which may affect lifetime. This could be due to a critical thinning of the membrane or the loss of binder within the catalyst layer.

Eventually, membrane thinning may cause the electrolyzer to reach its end of life due to increased gas crossover. Therefore, the membrane represents a lifetime-limiting component and its degradation was simulated through a numeric model implemented in Matlab/SIMULINK® . The model was supported by ex-situ experiments, which found hydrogen peroxide to be crucial for the membrane attack reaction, while iron ions act as a strong catalyst for the membrane attack reaction even in low concentrations of a few ppm. Iron impurities as well as other Fenton-active metallic impurities should therefore be avoided in the system. The model was able to capture the trends connected to both hydrogen peroxide and iron ions. Simulations of in-situ oper-

ation revealed a positive impact of high current on fluoride emission rate in terms of degradation, which decreases by a factor of 5 from 0.2 to 2.0 A cm^{-2}. The model is a functional tool to gain insights into the involved degradation mechanisms and may serve as a basis to optimize operation strategies.

6.1.1 Main Contributions

- It was found that voltage degradation for a state of the art cell design is acceptable at temperatures up to 80 °C, while membrane thinning is the lifetime limiting factor
- High temperature operation above 80 °C is a crucial operation parameter that significantly enhances degradation due to membrane thinning and ohmic cell resistance increase
- The experiments revealed that constant operation should be avoided to minimize the effect of both reversible and irreversible voltage degradation, while dynamic operation with current/potential changes of <60 s is beneficial for decreasing voltage degradation
- For the first time, a PEM WE model that takes into account the temperature effect on reaction kinetics was reported. The model was supported by experimental work on the impact of hydrogen peroxide and iron ions on the reaction kinetics

6.2 Future Work

In order to see a wide implementation of the PEM WE technology, a cost reduction is crucial. Concerning the presented work, the set of in-situ experiments should be validated and enriched by high current/high voltage operation. A shift to higher operation currents would lead to a significant drop in cost. Also the seemingly positive effect of current interruption and potential shifts has to be confirmed and further investigated, for example by studying a constant profile that is only interrupted for 1 s every 100 s. Eventually, the results from the single cell experiments have to be validated on a stack.

Furthermore, operation at high pressure has to be investigated in terms of operation safety and degradation. This is due to the need of pressurized hydrogen for both storage and further utilization in industrial processes such as methanol production. Internal pressurization may make external mechanical compression redundant and therefore reduce the cost.

Finally, the membrane degradation model has to be fully validated and the origins of hydrogen peroxide and metallic ions have to be identified.

The latter is considered crucial, as even very low concentrations of Fenton-active metal impurities cause a severe effect on ionomer degradation. Feed water purification is a costly process in terms of both money and energy and has to be addressed in the future. Furthermore, a thorough study on the temperature and current effect on oxygen permeation has to be carried out, where the results may benefit the model accuracy especially where the in-situ fluoride emission rate is underestimated compared to the measured values.

In a broader sense, PEM WE may highly benefit from the emergence of new technologies such as 3D-printing, which may simplify prototyping and therefore cut the development cost. Besides the positive effect of industrial scale production on the price, other fundamentally different approaches in cell design may be beneficial for cost reduction. As bipolar plates are the major contributor to the stack cost, they bear a high saving potential. For example, production cost may be reduced if the function of the flow channels was taken over by the porous transport layer.

Lastly, the cost for the catalyst can drop significantly by replacing the state of the art catalyst with non-noble options. However, the share of the catalyst of the stack cost is less than 10%. Assuming around 60% of the system cost for the stack leaves little saving potential even by cutting the catalyst loading in half. The more severe issue related to the catalyst is the limited availability of iridium, which is the driving force behind the efforts to reduce loading and increase efficiency. Eventually, a functional alternative to iridium has to be found to enable upscaling on a grid-level.

References

References

[1] Z. Abdin, C. J. Webb, and E. M. Gray, "Modelling and simulation of a proton exchange membrane (PEM) electrolyser cell," *International Journal of Hydrogen Energy*, vol. 40, no. 39, pp. 13 243–13 257, 2015. [Online]. Available: http://dx.doi.org/10.1016/j.ijhydene.2015.07.129

[2] A. H. Abdol Rahim, A. S. Tijani, S. K. Kamarudin, and S. Hanapi, "An overview of polymer electrolyte membrane electrolyzer for hydrogen production: Modeling and mass transport," *Journal of Power Sources*, vol. 309, pp. 56–65, 2016. [Online]. Available: http://dx.doi.org/10.1016/j.jpowsour.2016.01.012

[3] F. Arbabi, H. Montazeri, R. Abouatallah, R. Wang, and A. Bazylak, "Three-Dimensional Computational Fluid Dynamics Modelling of Oxygen Bubble Transport in Polymer Electrolyte Membrane Electrolyzer Porous Transport Layers," *Journal of The Electrochemical Society*, vol. 163, no. 11, pp. 3062–3069, 2016.

[4] A. S. Aricò, S. Siracusano, V. Baglio, N. V. Dijk, and L. Merlo, "Durability and Degradation Issues in PEM Electrolysis Cells and its Components Degradation Mechanisms and Enhanced Stability of PEM Electrolysis Cells Using Low Catalyst Loadings and Novel Type of Membranes," Electrohypem, Tech. Rep., 2016.

[5] A. S. Arico, S. Siracusano, N. Briguglio, V. Baglio, A. Di Blasi, and V. Antonucci, "Polymer electrolyte membrane water electrolysis: Status of technologies and potential applications in combination with renewable power sources," *Journal of Applied Electrochemistry*, vol. 43, no. 2, pp. 107–118, 2013.

[6] K. E. Ayers, E. B. Anderson, C. B. Capuano, B. D. Carter, L. T. Dalton, G. Hanlon, J. Manco, and M. Niedzwiecki, "Research Advances Towards Low Cost, High Efficiency PEM Electrolysis," *ECS Transactions*, vol. 33, no. 1, pp. 3–15, 2010.

[7] U. Babic, M. Suermann, F. N. Büchi, L. Gubler, and T. J. Schmidt, "Critical Review—Identifying Critical Gaps for Polymer Electrolyte Water Electrolysis Development," *Journal of The Electrochemical Society*, vol. 164, no. 4, pp. F387–F399, 2017. [Online]. Available: http://jes.ecsdl.org/lookup/doi/10.1149/2.1441704jes

[8] B. Bensmann, R. Hanke-Rauschenbach, G. Müller-Syring, M. Henel, and K. Sundmacher, "Optimal configuration and pressure levels of electrolyzer plants in context of power-to-gas applications," *Applied Energy*, vol. 167, p. 107–124, 2016. [Online]. Available: http://dx.doi.org/10.1016/j.apenergy.2016.01.038

[9] B. Bensmann, R. Hanke-Rauschenbach, I. K. Peña Arias, and K. Sundmacher, "Energetic evaluation of high pressure PEM electrolyzer systems for intermediate storage of renewable energies," *Electrochimica Acta*, vol. 110, pp. 570–580, 2013.

[10] M. Bernt and H. A. H. Gasteiger, "Influence of Ionomer Content in IrO 2 /TiO 2 Electrodes on PEM Water Electrolyzer Performance," *Journal of The Electrochemical Society*, vol. 163, no. 11, pp. F3179–F3189, 2016. [Online]. Available: http://jes.ecsdl.org/lookup/doi/10.1149/2.0231611jes

[11] M. Bernt, A. Siebel, and H. A. Gasteiger, "Analysis of Voltage Losses in PEM Water Electrolyzers with Low Platinum Group Metal Loadings," *Journal of The Electrochemical Society*, vol. 165, no. 5, pp. F305–F314, 2018. [Online]. Available: http://jes.ecsdl.org/lookup/doi/10.1149/2.0641805jes

[12] L. Bertuccioli, A. Chan, D. Hart, F. Lehner, B. Madden, and E. Standen, "Development of Water Electrolysis in the European Union - Final Report," Fuel Cells and Hydrogen Joint Undertaking, Tech. Rep. February, 2014. [Online]. Available: http://www.fch-ju.eu/sites/default/files/studyelectrolyser%7B_%7D0-Logos%7B_%7D0%7B_%7D0.pdfhttp://www.fch-ju.eu/sites/default/files/studyelectrolyser_0-Logos_0_0.pdf

[13] D. Bessarabov, H. Wang, H. Li, and N. Zhao, *PEM Electrolysis for Hydrogen Production - Principles and Applications*. CRC Press, 2016.

[14] BioLogic, "HCP-803 High Current Potentiostat," 2018. [Online]. Available: http://www.bio-logic.net/en/products/potentiostat-galvanostat-eis/hcp-803-high-current-potentiostatgalvanostateis/

[15] F. N. F. Büchi, M. Inaba, and T. J. T. T. J. Schmidt, *Polymer Electrolyte Fuel Cell Durability*. Springer, 2009.

[16] M. Carmo, D. L. Fritz, J. Mergel, and D. Stolten, "A comprehensive review on PEM water electrolysis," *International Journal of Hydrogen Energy*, vol. 38, no. 12, pp. 4901–4934, 2013.

[17] M. Chandesris, V. Médeau, N. Guillet, S. Chelghoum, D. Thoby, and F. Fouda-Onana, "Membrane degradation in PEM water electrolyzer: Numerical modeling and experimental evidence of the influence of temperature and current density," *International Journal of Hydrogen Energy*, vol. 40, no. 3, pp. 1353–1366, 2015.

[18] M. Chandesris, R. Vincent, L. Guetaz, J.-S. Roch, D. Thoby, and M. Quinaud, "Membrane degradation in PEM fuel cells: From experimental results to semi-empirical degradation laws," *International Journal of Hydrogen Energy*, vol. 42, no. 12, pp. 8139–8149, 2017. [Online]. Available: http://linkinghub.elsevier.com/retrieve/pii/S0360319917306249

[19] S. Cherevko, "Stability and dissolution of electrocatalysts : Building the bridge between model and " real world " systems," *Current Opinion in Electrochemistry*, pp. 1–8, 2018. [Online]. Available: https://doi.org/10.1016/j.coelec.2018.03.034

[20] CIA, "The World Factbook: DENMARK," 2018. [Online]. Available: https://www.cia.gov/library/publications/resources/the-world-factbook/geos/da.html

[21] ——, "The World Factbook: ELECTRICITY - FROM HYDROELECTRIC PLANTS," 2018. [Online]. Available: https://www.cia.gov/library/publications/resources/the-world-factbook/rankorder/2238rank.html

[22] ——, "The World Factbook: ELECTRICITY - FROM OTHER RENEWABLE SOURCES," 2018. [Online]. Available: https://www.cia.gov/library/publications/resources/the-world-factbook/rankorder/2240rank.html

[23] ——, "The World Factbook: WORLD," 2018. [Online]. Available: https://www.cia.gov/library/publications/resources/the-world-factbook/geos/xx.html

[24] Danish Governement, "Energy Strategy 2050 - From Coal, Oil and Gas to Green Energy," *Danish Energy Agency*, no. February, 2011.

[25] F. De Bruijn, "PEMFC Lifetime and Durability: an overview," in *Workshop: Entwicklung von Lebensdauerprognosemodellen von Brennstoffzellen in realen Anwendungen*, 2011.

[26] A. Diedrichs, M. Rastedt, F. J. Pinar, and P. Wagner, "Effect of compression on the performance of a HT-PEM fuel cell," *Journal of Applied Electrochemistry*, vol. 43, no. 11, pp. 1079–1099, 2013.

[27] DLR, "Abschlussbericht Verbundsvorhaben LastEISys," DLR, Tech. Rep., 2016.

[28] Energinet, "Teknisk forskrift Automatisk og manuel elforbrugsaf- lastning," Energinet, Tech. Rep., 2014.

[29] ——, "Energinet Electricity Balance Data," 2015. [Online]. Available: https://www.energidataservice.dk/en/dataset/electricitybalance/resource_extract/498c68e3-d248-4965-b36f-3aa738130adc?page=2&applied-filters=HourDK%7CBETWEEN%7C2015-07-09+00%3A00+AND+2015-07-11+00%3A00&sort=HourDK%2C+desc#resource-preview

[30] ENTSO-E, "ENTSO-E Objectives," 2018. [Online]. Available: https://www.entsoe.eu/about/inside-entsoe/objectives/

[31] E. Fabbri, A. Habereder, K. Waltar, R. Kötz, and T. J. Schmidt, "Developments and perspectives of oxide-based catalysts for the oxygen evolution reaction," *Catalysis Science and Technology*, vol. 4, no. 11, pp. 3800–3821, 2014.

[32] Q. Feng, X. Yuan, G. Liu, B. Wei, Z. Zhang, H. Li, and H. Wang, "A review of proton exchange membrane water electrolysis on degradation mechanisms and mitigation strategies," *Journal of Power Sources*, vol. 366, pp. 33–55, 2017. [Online]. Available: http://dx.doi.org/10.1016/j.jpowsour.2017.09.006

[33] C. L. Fevre, "Gas storage in Great Britain," Oxford Institute for Energy Studies, Tech. Rep. January, 2013. [Online]. Available: http://infrastructure.planningportal.gov.uk/wp-content/ipc/uploads/projects/EN030001/3.PostDecisionInformation/Decision/130409_EN030001_Chris_Le_Fevre_Report.pdf

[34] F. Fouda-Onana, M. Chandesris, V. Médeau, S. Chelghoum, D. Thoby, and N. Guillet, "Investigation on the degradation of MEAs for PEM water electrolysers part I: Effects of testing conditions on MEA performances and membrane properties," *International Journal of Hydrogen Energy*, vol. 41, pp. 16 627–16 636, 2016.

[35] F. Fouda-Onana, "AST PROTOCOLS FOR PEM WATER ELECTROLYIS," CEA Grenoble, Tech. Rep., 2016.

[36] M. W. Fowler, "DEGRADATION AND RELIABILITY ANALYSIS OF PEM FUEL CELL STACKS Average Cell Voltage," University of Waterloo, Tech. Rep., 2002.

[37] B. Frois, "Balancing the Grid with hydrogen technologies," CEA, Tech. Rep., 2017. [Online]. Available: http://www.efcf.com/fileadmin/content/GSMpresentations/03_Frois.pdf

[38] A. S. Gago, S. A. Ansar, B. Saruhan, U. Schulz, P. Lettenmeier, N. A. Cañas, P. Gazdzicki, T. Morawietz, R. Hiesgen, J. Arnold, and K. A. Friedrich, "Protective coatings on stainless steel bipolar plates for proton exchange membrane (PEM) electrolysers," *Journal of Power Sources*, vol. 307, p. in press, 2015.

[39] Gamry Instruments, "Reference 30k Booster," 2018. [Online]. Available: https://www.gamry.com/potentiostats/reference-30k-booster/

[40] M. Ghelichi, P. E. A. Melchy, and M. H. Eikerling, "Radically coarse-grained approach to the modeling of chemical degradation in fuel cell ionomers," *Journal of Physical Chemistry B*, vol. 118, no. 38, pp. 11 375–11 386, 2014.

[41] S. A. Grigoriev, K. Dzhus, D. G. Bessarabov, and P. Millet, "Failure of PEM water electrolysis cells: Case study involving anode dissolution and membrane thinning," *International Journal of Hydrogen Energy*, vol. 39, no. 35, pp. 1–7, 2014. [Online]. Available: http://linkinghub.elsevier.com/retrieve/pii/S0360319914013913

[42] S. A. Grigoriev, A. A. Kalinnikov, P. Millet, V. I. Porembsky, and V. N. Fateev, "Mathematical modeling of high-pressure PEM water electrolysis," *Journal of Applied Electrochemistry*, vol. 40, no. 5, pp. 921–932, 2010.

[43] S. A. Grigoriev, P. Millet, S. V. Korobtsev, V. I. Porembskiy, M. Pepic, C. Etievant, C. Puyenchet, and V. N. Fateev, "Hydrogen safety aspects related to high-pressure polymer electrolyte membrane water electrolysis," *International Journal of Hydrogen Energy*, vol. 34, no. 14, pp. 5986–5991, 2009. [Online]. Available: http://dx.doi.org/10.1016/j.ijhydene.2009.01.047

[44] S. A. Grigoriev, V. I. Porembskiy, S. V. Korobtsev, V. N. Fateev, F. Aupre, and P. Millet, "High-pressure PEM water electrolysis and corresponding safety issues," *International Journal of Hydrogen Energy*, vol. 6, pp. 3–10, 2010.

[45] L. Gubler, S. M. Dockheer, and W. H. Koppenol, "Radical (HO, H and HOO) Formation and Ionomer Degradation in Polymer Electrolyte Fuel Cells," *Journal of The Electrochemical Society*, vol. 158, no. 7, p. B755, 2011. [Online]. Available: http://jes.ecsdl.org/cgi/doi/10.1149/1.3581040

[46] F. Gutiérrez-Martín and I. Guerrero-Hernández, "Balancing the grid loads by large scale integration of hydrogen technologies: The case of the Spanish power system," *International Journal of Hydrogen Energy*, vol. 37, no. 2, pp. 1151–1161, 2012.

[47] A. W. Hofmann, *Introduction to modern chemistry experimental and theoretical*. WALTON AND MABERLY, London, 1866.

[48] IEA International Energy Agency, "Key World Energy statistics," 2017. [Online]. Available: http://www.enecho.meti.go.jp/statistics/total_energy/results.html

[49] M. Inaba, T. Kinumoto, M. Kiriake, R. Umebayashi, A. Tasaka, and Z. Ogumi, "Gas crossover and membrane degradation in polymer electrolyte fuel cells," *Electrochimica Acta*, vol. 51, no. 26, pp. 5746–5753, 2006.

[50] ITM Power, "HGAS Product Specifications," 2018. [Online]. Available: http://www.itm-power.com/product/hgas

[51] T. Kato, M. Kubota, N. Kobayashi, and Y. Suzuoki, "Effective utilization of by-product oxygen from electrolysis hydrogen production," *Energy*, vol. 30, no. 14, pp. 2580–2595, 2005.

[52] O. E. Kongstein, N. Guillet, and A. Ødegård, "Next-generation PEM electrolyzer for sustainable hydrogen production," NEXPEL, Tech. Rep., 2010.

[53] A. B. LaConti, H. Liu, C. Mittelsteadt, and R. C. McDonald, "Polymer Electrolyte Membrane Degradation Mechanisms – Findings Over the Past 30 Years and Comparison with Electrolyzers," *ECS Meeting*, vol. 14, no. 1990, pp. 1990–1990, 2005.

[54] M. Langemann, D. L. Fritz, M. Müller, and D. Stolten, "Validation and characterization of suitable materials for bipolar plates in PEM water electrolysis," *International Journal of Hydrogen Energy*, vol. 40, no. 35, pp. 11 385–11 391, 2015.

[55] P. Lettenmeier, R. Wang, R. Abouatallah, F. Burggraf, A. S. Gago, and K. A. Friedrich, "Coated Stainless Steel Bipolar Plates for Proton Exchange Membrane Electrolyzers," *Journal of The Electrochemical Society*, vol. 163, no. 11, pp. F3119–F3124, 2016. [Online]. Available: http://jes.ecsdl.org/lookup/doi/10.1149/2.0141611jes

[56] P. Lettenmeier, R. Wang, R. Abouatallah, S. Helmly, T. Morawietz, R. Hiesgen, S. Kolb, F. Burggraf, J. Kallo, A. S. Gago, and K. A. Friedrich, "Durable Membrane Electrode Assemblies for Proton Exchange Membrane Electrolyzer Systems Operating at High Current Densities," *Electrochimica Acta*, vol. 210, pp. 502–511, 2016. [Online]. Available: http://dx.doi.org/10.1016/j.electacta.2016.04.164

[57] P. Lettenmeier, R. Wang, R. Abouatallah, B. Saruhan, O. Freitag, P. Gazdzicki, T. Morawietz, R. Hiesgen, A. S. Gago, and K. A. Friedrich, "Low-cost and durable bipolar plates for proton exchange membrane electrolyzers," *Scientific Reports*, vol. 7, no. January, pp. 1–12, 2017. [Online]. Available: http://dx.doi.org/10.1038/srep44035

[58] H. W. X.-Z. Y. H. Li, *PEM Fuel Cell Diagnostic Tools*. CRC Press, 2012.

[59] H. Liu, F. D. Coms, J. Zhang, H. A. Gasteiger, and A. B. Laconti, "Chemical degradation: Correlations between electrolyzer and fuel cell findings," *Polymer Electrolyte Fuel Cell Durability*, pp. 71–118, 2009.

[60] W. Liu, K. Ruth, and G. Rusch, "Membrane Durability in PEM Fuel Cells," *Journal of New Materials for Electrochemical Systems*, vol. 4, no. 4, pp. 227–232, 2001.

[61] G. Lu, S. L. Bernasek, and J. Schwartz, "Oxidation of a polycrystalline titanium surface by oxygen and water," *Surface Science*, vol. 458, no. 1, pp. 80–90, 2000.

[62] L. Ma, S. Sui, and Y. Zhai, "Preparation and characterization of Ir/TiC catalyst for oxygen evolution," *Journal of Power Sources*, vol. 177, no. 2, pp. 470–477, 2008. [Online]. Available: http://linkinghub.elsevier.com/retrieve/pii/S0378775307026304

[63] J. Mališ, P. Mazúr, M. Paidar, T. Bystron, and K. Bouzek, "Nafion 117 stability under conditions of PEM water electrolysis at elevated temperature and pressure," *International Journal of Hydrogen Energy*, vol. 41, no. 4, pp. 2177–2188, 2016.

[64] F. Marangio, M. Santarelli, and M. Calì, "Theoretical model and experimental analysis of a high pressure PEM water electrolyser for hydrogen production," *International Journal of Hydrogen Energy*, vol. 34, no. 3, pp. 1143–1158, 2009.

[65] Mathesontrigas, "Lower and Upper Explosive Limits for Flammable Gases and Vapors," Mathesontrigas, Tech. Rep., 2001. [Online]. Available: http://www.chrysalisscientific.com/pg443-Lower-LEL-Upper-UEL-Explosive-Limits.pdf

[66] P. Millet, A. Ranjbari, F. De Guglielmo, S. a. Grigoriev, and F. Auprêtre, "Cell failure mechanisms in PEM water electrolyzers," *International Journal of Hydrogen Energy*, vol. 37, no. 22, pp. 17 478–17 487, 2012.

[67] S. M. R. Niya, R. K. Phillips, and M. Hoorfar, "Process modeling of the impedance characteristics of proton exchange membrane fuel cells," *Electrochimica Acta*, vol. 191, no. May, pp. 1–117, 2 2016. [Online]. Available: http://dx.doi.org/10.1016/j.electacta.2016.01.128

[68] NOVEL, "NOVEL project website," 2016. [Online]. Available: www.novelhydrogen.eu

[69] E. T. Ojong, E. Mayousse, T. Smolinka, and N. Guillet, "Advanced bipolar plates without flow channels , for PEM electrolysers operating at high pressure Hydrogen Session – Bipolar plates for PEM fuel cells and electrolyzers," Fraunhofer ISE, Tech. Rep., 2012.

[70] A. C. Olesen and S. K. Kær, "The Effect of PFSA Membrane Compression on the Predicted Performance of a High Pressure PEM Electrolysis Cell," *ECS Transactions*, vol. 68, no. 3, pp. 99–116, 2015.

[71] A. C. Olesen, C. Roemer, and S. K. Kær, "A numerical study of the gas-liquid, two-phase flow maldistribution in the anode of a high pressure PEM water electrolysis cell," *International Journal of Hydrogen Energy*, vol. 41, no. 1, pp. 52–68, 2016.

[72] P. Olivier, C. Bourasseau, and P. B. Bouamama, "Low-temperature electrolysis system modelling: A review," *Renewable and Sustainable Energy Reviews*, vol. 78, no. March, pp. 280–300, 2017.

[73] P. Paciok, M. Schalenbach, M. Carmo, and D. Stolten, "On the mobility of carbon-supported platinum nanoparticles towards unveiling cathode degradation in water electrolysis," *Journal of Power Sources*, vol. 365, pp. 53–60, 2017. [Online]. Available: http://dx.doi.org/10.1016/j.jpowsour.2017.07.033

[74] C. Rakousky, G. P. Keeley, K. Wippermann, M. Carmo, and D. Stolten, "The stability challenge on the pathway to high-current-density polymer electrolyte membrane water electrolyzers," *Electrochimica Acta*, vol. 278, pp. 324–331, 2018. [Online]. Available: https://doi.org/10.1016/j.electacta.2018.04.154

[75] C. Rakousky, U. Reimer, K. Wippermann, M. Carmo, W. Lueke, and D. Stolten, "An analysis of degradation phenomena in polymer electrolyte membrane water electrolysis," *Journal of Power Sources*, vol. 326, pp. 120–128, 2016.

[76] C. Rakousky, U. Reimer, K. Wippermann, S. Kuhri, M. Carmo, W. Lueke, and D. Stolten, "Polymer electrolyte membrane water electrolysis: Restraining degradation in the presence of fluctuating power," *Journal of Power Sources*, vol. 342, pp. 38–47, 2017. [Online]. Available: http://dx.doi.org/10.1016/j.jpowsour.2016.11.118

[77] C. Rozain, E. Mayousse, N. Guillet, and P. Millet, "Influence of iridium oxide loadings on the performance of PEM water electrolysis cells : Part II – Advanced oxygen electrodes," *"Applied Catalysis B, Environmental"*, vol. 182, pp. 123–131, 2016. [Online]. Available: http://dx.doi.org/10.1016/j.apcatb.2015.09.011

[78] P. S. Ruvinskiy, A. Bonnefont, C. Pham-Huu, and E. R. Savinova, "Using ordered carbon nanomaterials for shedding light on the mechanism of the cathodic oxygen reduction reaction," *Langmuir*, vol. 27, no. 14, pp. 9018–9027, 2011.

[79] D. M. F. Santos, "Hydrogen Production By Alkaline Water Electrolysis," *Quim. Nova*, vol. 36, no. 8, pp. 1176–1193, 2013.

[80] M. Schalenbach, M. Carmo, and D. L. Fritz, "Pressurized PEM water electrolysis : Efficiency and gas crossover," *International Journal of Hydrogen Energy*, vol. 8, no. 1, 2013.

[81] M. Schalenbach, M. A. Hoeh, J. T. Gostick, W. Lueke, and D. Stolten, "Gas Permeation through Nafion. Part 2: Resistor Network Model," *Journal of Physical Chemistry C*, vol. 119, no. 45, pp. 25 156–25 169, 2015.

[82] A. A. Shah, T. R. Ralph, and F. C. Walsh, "Modeling and Simulation of the Degradation of Perfluorinated Ion-Exchange Membranes in PEM Fuel Cells," *Journal of The Electrochemical Society*, vol. 156, no. 4, p. B465, 2009. [Online]. Available: http://jes.ecsdl.org/cgi/doi/10.1149/1.3077573

[83] V. B. Silva and A. Rouboa, "Hydrogen-fed PEMFC: Overvoltage analysis during an activation procedure," *Journal of Electroanalytical Chemistry*, vol. 671, pp. 58–66, 2012. [Online]. Available: http://dx.doi.org/10.1016/j.jelechem.2012.02.013

[84] S. Siracusano, V. Baglio, S. A. Grigoriev, L. Merlo, V. N. Fateev, and A. S. Aricò, "The influence of iridium chemical oxidation state on the performance and durability of oxygen evolution catalysts in PEM electrolysis," *Journal of Power Sources*, vol. 366, pp. 105–114, 2017.

[85] S. Siracusano, N. Van Dijk, R. Backhouse, L. Merlo, V. Baglio, and A. Arico, "Degradation issues of PEM electrolysis MEAs," *Renewable Energy*, vol. 123, pp. 52–57, 2018. [Online]. Available: http://linkinghub.elsevier.com/retrieve/pii/S0960148118301678

[86] S. Siracusano, N. Hodnik, P. Jovanovic, F. Ruiz-Zepeda, M. Šala, V. Baglio, and A. S. Aricò, "New insights into the stability of a high performance nanostructured catalyst for sustainable water electrolysis," *Nano Energy*, vol. 40, no. September, pp. 618–632, 2017.

[87] T. Smolinka, "Second International Workshop on Durability and Degradation Issues in PEM Electrolysis Cells and its Components," NOVEL, Tech. Rep., 2016.

[88] S. Song, H. Zhang, X. Ma, Z. Shao, R. T. Baker, and B. Yi, "Electrochemical investigation of electrocatalysts for the oxygen evolution reaction in PEM water electrolyzers," *International Journal of Hydrogen Energy*, vol. 33, no. 19, pp. 4955–4961, 2008.

[89] C. Spöri, J. T. H. Kwan, A. Bonakdarpour, D. P. Wilkinson, and P. Strasser, "The Stability Challenges of Oxygen Evolving Catalysts: Towards a Common Fundamental Understanding and Mitigation of Catalyst Degradation," *Angewandte Chemie - International Edition*, vol. 56, no. 22, pp. 5994–6021, 2017.

[90] S. Stucki, G. G. Scherer, S. Schlagowski, and E. Fischer, "PEM water electrolysers: evidence for membrane failure in 100 kW demonstration plants," *Journal of Applied Electrochemistry*, vol. 28, no. 10, pp. 1041–1049, 1998.

[91] H. Su, V. Linkov, and B. J. Bladergroen, "Membrane electrode assemblies with low noble metal loadings for hydrogen production from solid polymer electrolyte water electrolysis," *International Journal of Hydrogen Energy*, vol. 38, no. 23, pp. 9601–9608, 2013. [Online]. Available: http://dx.doi.org/10.1016/j.ijhydene.2013.05.099

[92] M. Suermann, A. Pătru, T. J. Schmidt, and F. N. Büchi, "High pressure polymer electrolyte water electrolysis: Test bench development and electrochemical analysis," *International Journal of Hydrogen Energy*, vol. 42, no. 17, pp. 12 076–12 086, 2017.

[93] S. Sun, Z. Shao, H. Yu, G. Li, and B. Yi, "Investigations on degradation of the long-term proton exchange membrane water electrolysis stack," *Journal of Power Sources*, vol. 267, pp. 515–520, 2014. [Online]. Available: http://dx.doi.org/10.1016/j.jpowsour.2014.05.117

[94] P. Trinke, B. Bensmann, and R. Hanke-Rauschenbach, "Current density effect on hydrogen permeation in PEM water electrolyzers," *International Journal of Hydrogen Energy*, vol. 42, no. 21, pp. 14 355–14 366, 2017. [Online]. Available: http://linkinghub.elsevier.com/retrieve/pii/S0360319917312971

[95] P. Trinke, B. Bensmann, S. Reichstein, R. Hanke-Rauschenbach, and K. Sundmacher, "Hydrogen Permeation in PEM Electrolyzer Cells Operated at Asymmetric Pressure Conditions," *Journal of The Electrochemical Society*, vol. 163, no. 11, pp. F3164–F3170, 2016. [Online]. Available: http://jes.ecsdl.org/lookup/doi/10.1149/2.0221611jes

[96] WindEurope, "Wind in power 2017," Wind Europe, Tech. Rep. February, 2018. [Online]. Available: https://windeurope.org/wp-content/uploads/files/about-wind/statistics/WindEurope-Annual-Statistics-2017.pdf

[97] F. J. Wirkert, "Hydraulic cell compression for performance preserving upscaling of PEM electrolyzers," *International Journal of Smart Grid and Clean Energy*, vol. 6, no. 2, pp. 171–176, 2017. [Online]. Available: http://www.ijsgce.com/index.php?m=content&c=index&a=show&catid=66&id=335

[98] K. H. Wong and E. Kjeang, "Macroscopic In-Situ Modeling of Chemical Membrane Degradation in Polymer Electrolyte Fuel Cells," *Journal of the Electrochemical Society*, vol. 161, no. 9, pp. F823–F832, 2014. [Online]. Available: http://jes.ecsdl.org/cgi/doi/10.1149/2.0031409jes

[99] E. Wright, E. Price, and J. Sharman, "The Impact of Non-uniform Electrodes on Performance and Gas Cross-over Challenges for CCMs in PEMWE," Johnson Matthey, Tech. Rep., 2016.

Paper A

Model-supported Characterization of a PEM Water Electrolysis Cell for the Effect of Compression

Steffen Henrik Frensch, Anders Christian Olesen, Samuel Simon Araya, Søren Knudsen Kær

The paper has been published in
Electrochimica Acta Vol. 263, pp. 228–236, 2018.

Model-supported characterization of a PEM water electrolysis cell for the effect of compression

Steffen Henrik Frensch[a,*], Anders Christian Olesen[a], Samuel Simon Araya[a], Søren Knudsen Kær[a]

[a]*Aalborg University, Department of Energy Technology, Pontoppidanstræde 111, 9220 Aalborg Øst, Denmark*

Abstract

This paper investigates the influence of the cell compression of a PEM water electrolysis cell. A small single cell is therefore electrochemically analyzed by means of polarization behavior and impedance spectroscopy throughout a range of currents (0.01 A cm^{-2} to 2.0 A cm^{-2}) at two temperatures (60 °C and 80 °C) and eight compressions (0.77 MPa to 3.45 MPa). Additionally, a computational model is utilized to support the analysis. The main findings are that cell compression has a positive effect on overall cell performance due to decreased contact resistances, but is subject to optimization. In this case, no signs of severe mass transport problems due to crushed transport layers are visible in either polarization curves or impedance plots, even at high currents. However, a Tafel plot analysis revealed more than one slope throughout the current range. The change in the Tafel slope is therefore discussed and connected to the electrochemical reaction or an ohmic contribution from a non-electrode component.

Keywords: PEM water electrolysis, Impedance spectroscopy, Contact resistance, Model validation, Clamping pressure

1. Introduction

Energy storage is considered crucial for a successful transition to carbon neutral energy production. A hydrogen based energy production can be a key technology as hydrogen can be stored and distributed as a liquid or gas, and utilized in fuel cells (FC) to produce electrical energy and heat [1]. Nowadays, the main source of hydrogen is from steam reformed hydrocarbons or alcohols [2] with inevitable release of greenhouse gases. However, hydrogen can also be produced through water electrolysis (WE), where water is electrochemically split into its elements, hydrogen and oxygen. If the required electrical energy comes from renewable energy sources, this process can be considered CO_2 neutral. Additionally, electrolyzers can potentially provide grid-services for frequency stability [3].

Polymer electrolyte membrane (PEM) electrolysis can be considered an evolving technology that is entering the market and has attracted more research interest in the past few years due to certain advantages [2, 4]. Among others, PEM electrolyzers can be manufactured in compact systems due to their solid electrolyte membrane with small footprints and offer relatively high efficiency. In the context of grid stability, they are especially interesting due to good dynamic response times and start/stop behavior, and a wide operating range [5]. Comparably fast starts are possible due to the operation at low temperatures of around 60 °C to 100 °C. Furthermore, the hydrogen gas purity can be maintained fairly high at 99.999% which makes further purification redundant [6]. PEM electrolyzers offer the possibility to operate under high pressures which allows hydrogen gas production at more than 100 bar [7]. Depending on the application, internal pressurization may make external gas compressors redundant and therefore reduce system complexity and cost [8]. Pure oxygen as a byproduct might be utilized and monetized in PEM FC or other applications, or released to the atmosphere [9]. The major drawback is the high cost due to the need of precious materials. Additionally, acceptable lifetime under dynamic operation has yet to be proven [5].

*Corresponding author

Email addresses: stf@et.aau.dk (Steffen Henrik Frensch), aco@et.aau.dk (Anders Christian Olesen), ssa@et.aau.dk (Samuel Simon Araya), skk@et.aau.dk (Søren Knudsen Kær)

An improvement in performance and durability requires proper characterization methods. Besides classic polarization curves (IV), other tools that researchers employed on WE include current interrupt, cyclic voltammetry, more visual approaches, such as electron microscopy, and electrochemical impedance spectroscopy (EIS) [10, 11]. EIS is a versatile characterization technique that is already widely used in fuel cell applications [12, 13] and many researchers have also implemented EIS as a tool in their investigations on PEM electrolyzers [14, 15]. With the above mentioned characterization techniques, performance investigations for different membrane-electrode-assemblies (MEAs) in terms of materials and loading were compared [16, 17], as well as studies on the impact of the feed water flow type [18] and stoichiometry [19].

However, not many systematic studies are available in the literature that reveal more insight about how various operation conditions affect cell performance. Moreover, with the design consisting of multiple solid layers clamped between two end plates, the compression pressure is an interesting parameter and possibly subject to optimization. While the compression pressure is reasonably well researched for FC, WE lacks studies [20, 5]. EIS can provide useful insights for analyzing compression [21, 22].

This paper investigates the performance of a single cell under different current and temperature operation points at various compressions. The purpose is to better understand what the most relevant operation parameters are. The experimental work is supported by computational modelling in order to extract characteristic parameters such as the exchange current density. The combination of experimental data and a model approach also helps to divide the different resistance contributions between the components.

2. Methodology

All experiments are carried out on a single cell set-up. Custom made MEAs by EWII Fuel Cells A/S (Denmark) with an active area of 2.89 cm^2 (1.7 cm*1.7 cm) are tested. The assembly consists of a commercial Nafion 117 membrane coated with Iridium oxide (IrO_2, 0.3 mg cm^{-2}) on the anode and carbon-supported Platinum (Pt/C, 0.5 mg cm^{-2}) on the cathode. The porous transport layers (PTL) are carbon cloth (Sigracet 35DC) and titanium felt on the cathode and the anode, respectively. The Ti felt is 350 µm thick, with a porosity of 81% and a fiber diameter of 20 µm. Additionally, an Iridium contact layer is employed at the anode between the catalyst layer and the Ti-felt. The layer consists only of pure Iridium metal with a loading of 2.48 mg cm^{-2}. The purpose of this layer is to provide better contact between the components and may be considered when calculating the total noble metal loading of the cell, especially when taking financial considerations into account. Other studies of this cell layout have been performed [23]. The coarse metallic Ir may oxidize fully or partially to IrO_2 during operation, which has to be considered when performing degradation studies [24].

The test bench is designed so that the cell is heated by the feed water, which is held at a constant temperature. The temperature is monitored close to the water inlet channel at the anode and close to the hydrogen outlet channel at the cathode. The water flow is constant around 270 mL min^{-1}, which represents a high over-stoichiometry. That way, steady temperature is established and mass transport contributions are minimized.

A Gamry Reference 3000 potentiostat/galvanostat is used for all IV and EIS measurements in a two-electrode set-up, meaning that the anode is connected to the working electrode and the cathode acts as the reference electrode. Figure 1 illustrates the experimental set-up.

Polarization curves are measured in variable steps of 0.01 A cm^{-2} to 0.2 A cm^{-2} in ascending direction. Each current step is held for 60 s before measuring the potential. The feed water flow rate is kept constant, which implies that the stoichiometry is in fact slightly changed throughout the experiment due to changes in current according to Faraday's law of electrolysis. However, the effect should not have a significant impact on the measurements since the over-stoichiometry is very high at any operation point with around 17000 at 1.0 A cm^{-2}.

Impedance spectra are, if not otherwise annotated, measured galvanostatic from 60 000 Hz to 0.1 Hz with 10 points per decade. The potentiostat supplies a variable AC disturbance current of 5% of the DC current operation point. The data is fit to an equivalent circuit as depicted in fig. 2. The circuit and its interpretation is discussed more in sections 3.2 and 3.3.

The MEA compression is controlled through the clamping pressure applied to the cell in eight steps from 0.77 MPa to 3.45 MPa (C0 to C7) according to tab. 1.

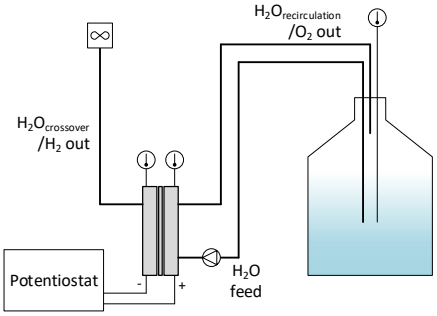

Figure 1: Test set-up including the cell, feed water tank, data acquisition, and power source.

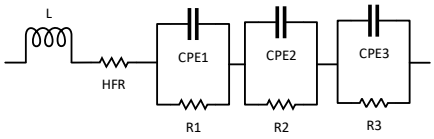

Figure 2: Equivalent circuit for impedance data fit

Estimating the actual clamping pressure applied to the MEA precisely is not as straight forward as it may seem. Additionally, the pressure distribution is generally a topic of interest which is investigated and optimized experimentally, and through simulations [25, 26]. Different approaches in fuel cell research can be found in the literature, which can be transferred to electrolysis research. However, the mechanisms may not be strictly derived from fuel cells since the geometry and fluid compositions differ. Furthermore, it is arguable which area should be considered to calculate the compression. In this work, four die springs are used to establish a pressure distribution as homogeneous as possible. Actual compression pressure as well as homogeneity are tested ex-situ with a pressure sensitive film in sec. 3.1. The film exhibits a red color at points of pressure that is dependent on the pressure value. The color intensity was analyzed with image processing software and can be related to the applied pressure through reference curves supplied by the manufacturer.

Moreover, contact resistances are measured between several components that are accessible. Each contact is investigated separately through a sample with a high precision Ohmmeter while being clamped between two copper plates. The three experimentally determined contact resistances are between the anode bi-polar plate (BPP) and the anode current distributor (CD), between the anode BPP and the Ti felt, and between the cathode BPP and cathode CD.

C0	C1	C2	C3
0.77 MPa	1.15 MPa	1.53 MPa	1.92 MPa

C4	C5	C6	C7
2.30 MPa	2.68 MPa	3.06 MPa	3.45 MPa

Table 1: Compression steps

2.1. Model Description

A 2-dimensional model approach is utilized in this study. The model is based on simulating the polarization curve of the cell at each operation point by fitting certain parameters. For a detailed description of the model development, the reader is referred to a previous publication [27]. The polarization curve is constructed through the Nernst potential raised by the losses. Due to the small geometry of the cell and the high over-stoichiometry, only activation and ohmic losses are considered. The assumption of negligible mass transport losses is validated by the experimentally measured IV curves shown in figure 5. Since all experiments are carried out at atmospheric pressure, the cell potential can be calculated as:

$$E_{cell} = E_{Nernst}(T) + \eta_{act}(i,T) + \eta_{ohm}(i,T) \tag{1}$$

where i is the current density and T the temperature. The activation overpotential is estimated through the Butler-Volmer equation as [28]:

$$i = i_0 \cdot [e^{\alpha n F \eta/(RT)} - e^{-(1-\alpha) n F \eta/(RT)}] \tag{2}$$

where R and F have their common meaning, i_0 is the exchange current density, n the number of electrons, η the overpotential, and α is the charge transfer coefficient. The application of the Butler-Volmer equation assumes one rate determining step (rds) for the modelled reaction mechanism [29]. For the sake of modelling simplicity, α is therefore assumed to be constant over the whole current range [30, 31, 32].

The ohmic overpotential is simulated as:

$$\eta_{ohm} = i \cdot [R_m(T, \lambda) + R_c] \tag{3}$$

where R_m is the area specific membrane resistance and R_c the area specific contact resistance. The membrane resistance is implemented as a function of temperature and water content (λ). The model is utilized to fit the experimental data, where i_0, and R_c are the most important fitting parameters.

3. Results and Discussion

3.1. Compression Pressure Analysis

An ex-situ investigation on the compression pressure is carried out in order to validate the theoretical values as reported in tab. 1. Three layers of pressure sensitive film are placed within the cell: At the anode between flow field and Ti felt and between Ti felt and CL, and at the cathode between PTL and flow field.

Figure 3 indicates the applicability of the method. A higher compression force leads to a more intense red tone, and the contact-less channels between the land areas are visible as white areas, indicating no pressure. The experiment reveals the importance of the pressurization method. The cell in this study was clamped with four die springs.

Figure 3 (grey box) shows the pressure distribution at 2.30 MPa for all three locations. As it can be seen, the cathode side (bottom) exhibits the channels clearly, suggesting that only the land area compresses the MEA. Similar results can be seen at the anode between the BPP and the PTL (middle), where the significantly smaller channels are still clearly visible. The situation changes when comparing to the result between the PTL and the CL at the anode side (top), where the distribution is more uniform and only the cathode-side flow channels can be identified. This can be seen as a confirmation that the Ti felt serves the purpose of uniformly distributing the contact points (and therefore current and fluids) from the BPP to the electrode. The figure also shows the anode-side film after each compression step was applied (left to right), where the last compression step was not experimentally determined due to restrictions in the pressure range of the film.

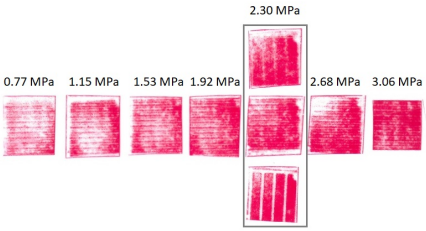

Figure 3: Pressure sensitive film after being clamped between the anode BPP and PTL at 0.77 MPa to 3.06 MPa from left to right. For comparison: Film after being clamped between anode PTL and CL (top), and cathode PTL and BPP (bottom) at 2.30 MPa

The applied pressure is not always uniformly distributed, but can be considered sufficient for this work. A non-homogeneous compression may lead to local hot spots and can affect the lifetime of the cell considerably [33]. Figure

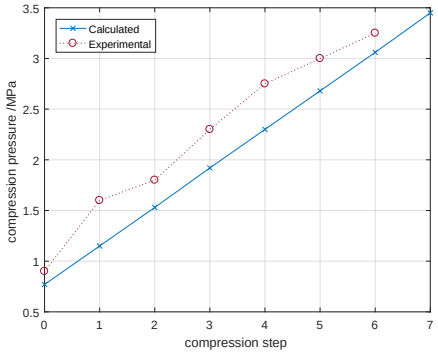

Figure 4: Comparison of calculated and experimentally determined compression pressure for each step. The calculated values are used for the further analysis

4 summarizes the comparison between the experimentally extracted compression pressure for each step compared to the calculated ones. It has to be noted that the experimental determination underlies some uncertainties and can only be seen as an indication. The film itself is rated with ±10% accuracy, but is highly affected by environmental influences such as temperature and humidity. Furthermore, the value for the pressure is extracted as an average over the land area of the flow field, i.e., assuming homogeneous compression and neglecting the area of the channels. As indicated above, the stiff Ti felt distributes the pressure sufficiently well to make this assumption acceptable. It can be seen in the figure that the experimental determination overestimates the values, or that the calculated values are slightly too low, respectively. However, the linear trend is visible and changes in compression are reasonably captured. For further analysis the calculated values are chosen as tabulated in tab. 1.

3.2. Polarization Curves and Electrochemical Impedance Spectroscopy

The performance of the single cell in terms of polarization curves is shown in fig. 5. The figure includes the plots for all eight compressions at both temperatures 60 °C and 80 °C.

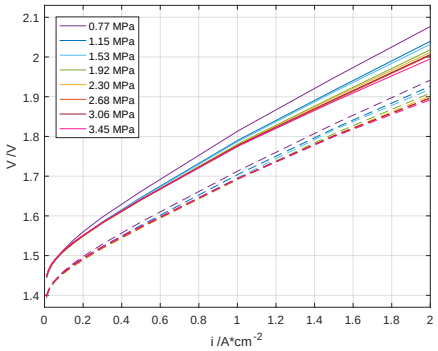

Figure 5: Polarization curves for all compressions at 60 °C (solid) and 80 °C (dashed)

Generally, the cell exhibits close to state of the art performance at both temperatures, with a voltage at 2.0 A cm^{-2} of 2.01 V at 60 °C and 1.90 V at 80 °C at medium compression (2.30 MPa) [34, 35]. The positive effect of increased

temperature can be seen easily. This behavior is expected due to better reaction kinetics for both hydrogen evolution reaction (HER) and oxygen evolution reaction (OER) [2], and better membrane conductivity [36]. This is also confirmed by the impedance data, which was systematically recorded at several operation points. For the impedance analysis, only the values for high frequency resistance (HFR) and low frequency resistance (LFR) are considered. Figure 6 exemplary shows the impedance data together with their model fits as a Nyquist plot for different currents at 2.30 MPa and both temperatures.

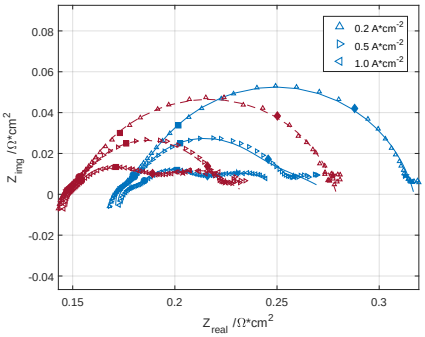

Figure 6: Impedance data at 2.30 MPa and different currents as a Nyquist plots. The marks represent the frequencies 10 000 Hz (∗), 1000 Hz (•), 100 Hz (■), 10 Hz (⧫), and 1 Hz (★). The respective model fits are shown for both 60 °C (solid) and 80 °C (dashed).

HFR and LFR represent the intercepts of the Nyquist plot with the x-axis at high frequency (left) and low frequency (right), respectively. The HFR represents the total area normalized ohmic resistance within cell, which includes the membrane resistance (both to electron and proton transport), material resistance of the components, and contact resistances. Other sources are assumed to be negligible. The LFR moreover includes the polarization resistance of the cell.

It can be seen that the HFR decreases with increasing temperature at the same current operation point. That supports the claim of better membrane conductivity at elevated temperatures. The LFR shifts accordingly, but when comparing the difference between HFR and LFR at the two temperatures, a decrease of around 6 mΩ cm^2 can be observed. This difference is an indication of better reaction kinetics at elevated temperatures.

It can furthermore be seen that the Nyquit plots exhibit different characteristics depending on the operation condition. On first sight, it seems that between the high- and low frequency intercepts, two to three semi-circles can be distinguished. Low current operation (0.2 A cm^{-2}) shows a small semi-circle in the high-frequency area (>10 kHz), followed by one big semi-circle in the mid-frequency area and relatively indistinguishable shape in the at low frequencies (<1 Hz). With increasing current, while the high frequency arc remains unaltered, the second semi circle shrinks, and a third semi-circle appears and becomes more evident at around 1 A cm^{-2}. The shrinking of an arc in the Nyquist plot signifies decreased impedance, and therefore, increase in reaction processes. Even though, the low frequency arc is usually associated with mass transport losses in the fuel cell literature [12], in the current work where high over stoichiometry is used, the evolution of the third arc may be explained differently.

As the LFR represents the total polarization resistance including the HFR parts, the value should be equal to the slope of the polarization curve according to

$$R_{pol} = \frac{\Delta U}{\Delta i} = LFR \tag{4}$$

Therefore, the two values should be in agreement. Figure 7 shows, that the LFR is slightly smaller than the IV slope throughout the whole current range at both temperatures. The slow EIS measurements at low frequencies (<1 Hz) are far more affected by noise compared to the fast measurements at high frequencies. That as well as the fitting procedure for the LFR can induce errors in the measurement. However, since the difference seems to be systematic (all values

are smaller), the cause may not solely lie within inaccuracies. Although the phenomenon was also observed by some fuel cell researchers [37], no commonly agreed explanation can be found in the literature, while other authors found the two resistances to be equal both in FC and WE research [38, 23]. A full paper dedicated to the topic for FC can be found in [37]. The authors connect the difference to the reactant feed mode and account for it through a model. In this work, the difference is within a 12% margin.

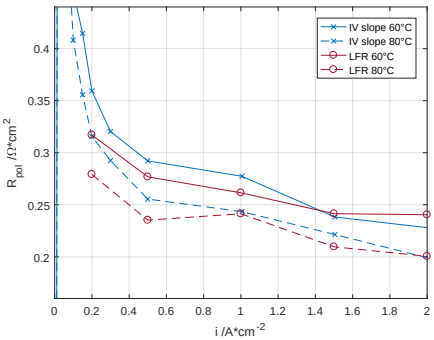

Figure 7: Polarization resistance from IV slopes (X) and LFR (O) at 60 °C (solid) and 80 °C (dashed) at 2.30 MPa for both temperatures

When focusing on the less researched effect of cell compression, the first impression from the polarization curves is that a higher compression has a positive effect on the cell performance at higher currents. The differences in voltage at 2.0 A cm^{-2} at lowest compression compared to highest compression at 60 °C and 80 °C are 81 mV and 49 mV, respectively. This effect seems to vanish or even reverse at lower current operation points. Therefore, it can be concluded that the improved performance is mainly due to decrease in the total ohmic resistance within the cell.

3.3. Model Supported Analysis

To allow for a more detailed analysis on the effect of compression on the cell performance, two modelling approaches are followed based on the two characterization methods: First, the electrical equivalent circuit (EEC) as shown in figure 2 is fit with EIS data. Second, the model proposed in section 2.1 is fit with polarization data. Since no reference electrode is incorporated into the cell, all measurements refer to the whole cell assembly including anode and cathode contributions.

Fitting impedance data to an EEC is a highly sensitive process with multiple sources of errors. The fundamental problem is that most circuit components cannot be connected to an actual cell component. While HFR was introduced earlier and can be justified through the existence of purely ohmic components, the other elements have to be further explained. Many authors, especially in FC research, use two RC-loops and refer to them as anode- and cathode-contributions [39]. This assumption may be supported by the development of a mechanistic model, which results in a similar EEC [40], but cannot overcome the problem of multiple fitting solutions. Sometimes, the hydrogen oxidation reaction at the anode is considered orders of magnitude faster compared to the oxygen reduction reaction at the cathode and therefore neglected [41]. The capacitance then embodies the double layer capacitance at the electrode interface, where the resistance represents the charge transfer resistance. Often, the capacitor is replaced by a constant-phase element (CPE), which represents a non-uniformly distributed double layer that appears as a depressed semi-circle in a Nyquist plot [42, 43]. Generally, R//C-circuits (or R//CPE-circuits) can be associated to characteristic frequency regions, and therefore, represent processes of different time constants. These can include different reaction mechanisms, different steps of a certain reaction, or diffusion processes. Finally, the inductor in series with the HFR represents possible inductive parts of cables and other components that can be observed in the impedance data.

The observation from the IV curves that an increased compression leads to reduced ohmic resistance, is validated by the impedance data. Figure 8 shows the HFR as a function of applied pressure for both temperatures at 1.0 A cm^{-2}.

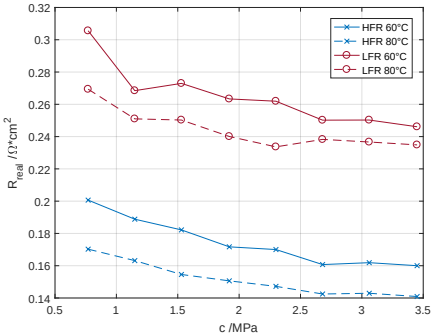

Figure 8: HFR (X) and LFR (O) at 60 °C (solid) and 80 °C (dashed) at 1.0 A cm^{-2}

The HFR decreases both with increasing temperature and increasing compression. Since the HFR represents only ohmic resistances, the decrease with temperature can be connected to the increased conductivity of the membrane [44]. For 0.77 MPa, the HFR drops from 201 mΩ cm^2 at 60 °C to 170 mΩ cm^2 at 80 °C. At higher temperatures, not only do the absolute resistance values decrease with increasing compression, but also the achieved enhancements decrease. For example, the enhancement from 60 °C to 80 °C for 0.77 MPa is around 30 mΩ cm^2, but it drops to around 20 mΩ cm^2 for 3.45 MPa, which has resistance value of 160 mΩ cm^2 at 60 °C and 141 mΩ cm^2 at 80 °C. That means, the compression-related benefits are more pronounced at lower temperatures.

However, the HFR at both temperatures clearly decreases with increased compression. Following a non-linear relationship, the HFR at 3.45 MPa and 60 °C drops to around 80% of its value at 0.77 MPa. At 80 °C, the HFR drops to around 83%. The results are in line with the findings from the IV curves and support the idea that higher compressions lead to lower ohmic losses. Two major reasons may be assumed to contribute to that: A higher membrane compression shortens the distance for protons to travel, i.e. leads to a lower overpotential. Additionally, an increased clamping pressure lowers the contact resistances between the components. The first cause is rejected, as the membrane compression has a negative effect on the water uptake, which overwhelms the positive effect of lower thickness (see figure 10). On the other hand, as it is known from fuel cell research, the electrical contacts between the several solid layers are highly influenced by the compression [20].

Many studies suggest that the compression is subject to optimization, as the contact resistance decreases logarithmic to a certain minimum, while other parameters may affect the cell performance negatively. As an example, the gas diffusion layers (GDL) may be crushed and pushed into the channels, which results in mass transport problems. Although the materials are not exactly the same and partly serve a different purpose compared to fuel cells, the general principles may be transferred. The gas diffusion layers are somewhat equivalent to the PTL in WE, where the cathode side PTL in this case is made of the same material as common GDL for fuel cells. In order to further investigate the influence of compression, temperature, and current, the proposed model is utilized to extract several parameters from the polarization data.

The extracted parameters of major interest are the exchange current density (i_0) and the contact resistance (R_c), which are shown in figure 9 for all compressions. Note that the reported i_0 is the reference value at 25 °C and implemented as a function of temperature, where R_c is temperature independent. Furthermore, the fit value for the activation energy E_{act} is 0.103 455 MJ mol^{-1} and the symmetry factor β is 0.4931

It can be seen that the overall contact resistance steadily decreases with increasing compression. With a value of 65.3 mΩ cm^2 at 0.77 MPa and 52.9 mΩ cm^2 at 3.45 MPa, the reduction accounts for around 19% of its original value.

In the meanwhile, the exchange current density experiences an increase up to around 1.5 MPa, followed by a steady decrease up to the highest compression. In this figure, i_0 represents the apparent exchange current density. That means, the related area does not represent the active area of the cell, but can rather be seen as the electrochemical surface area (ECSA), which includes the surface roughness of the layers. An increase in ECSA implies an increase in

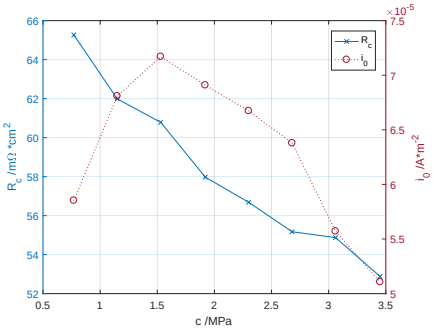

Figure 9: Model fits for contact resistance (solid) and the apparent reference exchange current density at 25°C (dotted)

the apparent exchange current and therefore an increase in performance. From the lowest compression up to 1.5 MPa, an increase in ECSA may be deduced from the figure. As the Ti felt on one hand and the carbon cloth on the other get pressed against the respective catalyst layers, the electrochemically active area may increase. Voids between these layers may be filled and the three phase boundary is increased. At a certain point, the compression may get high enough to not only increase the surface area, but also start crushing the porous PTLs, especially the carbon at the cathode side. In turn, the ECSA decreases as the surfaces smooths, and the exchange current decreases as seen in the figure. Although not observed in this work, a high compression may also lead to increased mass transport problems, as the porosity of the PTLs decrease. Furthermore, it may facilitate degradation, as hot sports are more likely to occur due to mechanical wear down [45].

3.4. Contact Resistances

It is furthermore attempted to separate the total ohmic resistance (HFR) into its main contributors as follows:

$$R_{ohm} = R_{m,H^+} + R_c + R_{components} \tag{5}$$

Figure 10 shows the total ohmic resistance of the cell together with the respective contributions of the membrane and the contacts as predicted by the model. For comparison, the HFR extracted from the impedance data is also plotted.

The membrane compression has a negative effect on the water uptake (λ) of the Nafion, where a lower λ decreases the conductivity, despite the positive effect of a slightly lower thickness. Therefore, the membrane resistance increases slightly over the compression range. However, a positive effect on the cell performance can be observed due to decreasing contact resistance with increasing compression. Figure 10 reveals, that the decrease of ohmic resistance can be solely attributed to contact resistances. To further investigate the contacts, ex-situ measurements are carried out.

Figure 11 shows the three contact resistances as experimentally determined. All measurements were taken at room temperature (25 °C). For comparison, the model prediction for the total contact resistance is also included.

The measurements reveal that the contact between the carbon BPP on the cathode side and the the respective CD accounts for the highest share. Somewhat surprisingly, the cell under investigation here does not show a significant contribution of the anodic PTL (Ti felt) as found by other studies [46]. The reason may be the incorporated Ir metal layer between the CL and the PTL on the anode, which is a relatively unique feature. The total values predicted by the model are higher than the experimental values for most compressions. It has to be kept in mind, that the model summarizes all contact resistances as one, where only three contacts are determined experimentally due to accessibility of the layers. The contacts between the catalyst layers on anode and cathode side add to the total value, as well as the cathode-side PTL contacts. Furthermore, the model as it is constructed assumes a constant charge transfer coefficient

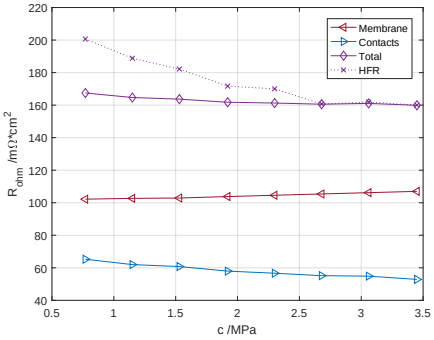

Figure 10: Breakdown of ohmic resistance between the two major contributors membrane and contacts at 60 °C

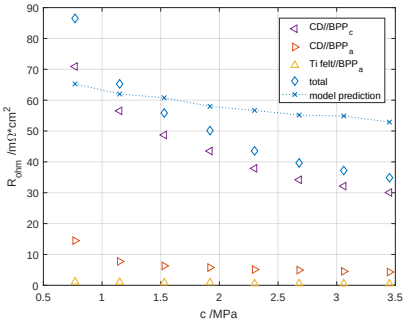

Figure 11: Contact resistances measured ex-situ. The model predictions are added for comparison

and may therefore overestimate the contact resistance as a result of applying the Butler-Volmer equation to the multi-electron transfer reactions. Therefore, the here suggested contact resistance and the further indicated share of roughly 2/3 to 1/3 for the membrane and the contacts, respectively, may be analyzed with care. The next section explains the problems by analyzing possible reaction mechanisms further.

3.5. Tafel Plot Analysis

The overall process of splitting water in a PEM electrolysis cell can be described as

$2\,H_2O \longrightarrow 2\,H_2 + O_2$

The two half-cell reactions at the anode and cathode are the oxygen evolution reaction (OER) and hydrogen evolution reaction (HER), respectively. The HER is fast due to the relatively high exchange current density and the high reversibility. The OER is somewhat more sluggish and less well understood [2]. However, different reaction mechanisms were proposed and table 2 summarizes one that is believed to occur in the given environment. That means acidic media, and an Iridium-based catalyst for the OER. For the following discussion, the cathode is considered as a reference electrode. Therefore, all observations are attributed to the OER, where the HER is neglected here, since it is assumed to only play a minor role for the characterization [47, 14].

Step	Reaction
(1)	$S + H_2O \longrightarrow S-OH + H^+ + e^-$
(2)	$S-OH \longrightarrow S-O^- + H^+ + e^-$
(3)	$2\,S-O \longrightarrow S + O_2$

Table 2: Reaction mechanism for OER under PEM WE environment

Depending on which step is the rate determining step (*rds*), a theoretical Tafel slope for the reaction can be calculated and compared to the experimentally determined slope, which may give insight into the reaction mechanism. Tafel slopes of 132 mV/dec and 44 mV/dec should be observed at 60 °C for the first and the second step as *rds*, respectively. However, the experimental determination of the Tafel slope is not trivial, and controversially discussed in the literature. The discord already starts with how to correctly account for the ohmic (*iR*) correction of the potential. Where many examples of using the purely ohmic resistance of the HFR (or equivalently the current step response) can be found [48, 30, 49, 50], it is also conceivable to compensate for the total cell resistance represented by the LFR (or IV slope), since it may contain ohmic contributions from components of the cell other than the membrane and contacts. An example could be the ionic conduction within the Nafion catalyst binder [51, 23].

The Tafel plots including linear trendlines for both approaches (HFR and LFR correction) at 2.30 MPa together with a Butler-Volmer approximation are shown in figure 12a. It can be seen, that the HFR-corrected plot exhibits two

slopes, where the LFR-corrected plot seems to have only one. The two points at high currents could be explained by the fact that the actual LFR is decreasing with current, where here an average is chosen. The slope of the LFR-corrected plot is very similar to the first slope of the HFR-corrected plot with 43 mV/dec and 45 mV/dec, respectively. The value is also coherent with what is expected from the theoretical calculation when assuming step (2) to be rate determining. From the Tafel slopes, the charge transfer coefficient α can be estimated (not to be confused with the symmetry factor β). The parameter reveals insights into the reaction mechanism, symmetry, and number of exchanged electrons [52, 53, 54]. The single slope for the LFR-corrected plot implies a constant charge transfer coefficient and therefore supports the presented model approach. However, HFR-correction as well as the presence of more than one Tafel slope can be found throughout the literature [55, 56]. One explanation is to connect the deviation from what the Tafel equation predicts at higher currents to mass transport phenomena [30]. However, in this work mass transport problems are excluded due to high over-stoichiometry, interdigitated feed water channels, a small cell geometry, and a high anode PTL porosity [57]. Additionally, no evidence for mass transport problems were found in the recorded IV curves or impedance spectra. That being said, the second slope with 158 mV/dec may indicate a change in the OER *rds* from one at lower potentials to another one at higher potentials.

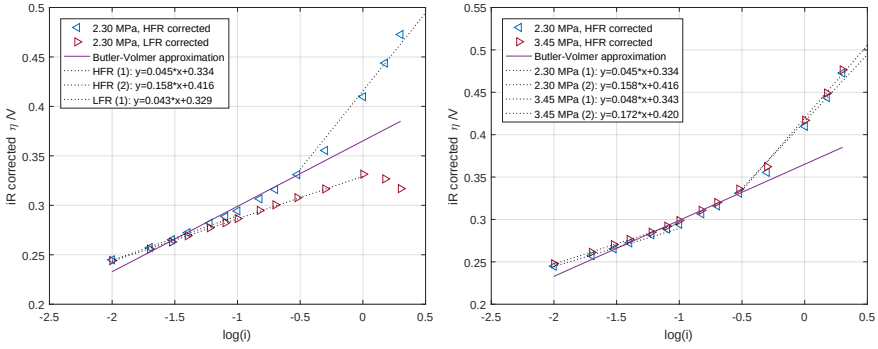

(a) Comparison between HFR- and LFR-correction at 2.30 MPa

(b) Comparison between 2.30 MPa and 3.45 MPa, HFR-correction

Figure 12: Tafel plots at 60°C with their respective linear approximations. The Butler-Volmer relation is added for comparison.

On the other hand, when looking at figure 12b, where the HFR-corrected Tafel plots at 2.30 MPa and 3.45 MPa are shown, it seems that while the first slope is compression-independent (variation of 3 mV/dec), the second slope is in fact slightly affected by the cell compression (variation of 14 mV/dec). That would suggest a more ohmic nature of the overpotential at higher current. A similar suggestion can be found in FC research, where a distinction is made between the non-electrode ohmic resistance, and the electrode ohmic resistance [58]. Where the non-electrode related share was found through the current interrupt method, the electrode related share was developed through oxygen reduction reaction and Ficks law of diffusion. A similar process may be present in PEM WE, although mass transport phenomena are neglected in the present work. It remains for future work to develop a model similar to what is shown for FC to precisely correct for the ohmic voltage drop [59]. Since the compression can also affect electrochemical parameters such as the exchange current density (see fig. 9), a change in reaction mechanism may also not be ruled out completely.

Additionally to the experimental Tafel plots, figure 12 shows the Butler-Volmer equation with the constant parameters apparent charge transfer coefficient and exchange current density as predicted by the model before. By comparison to the experimental data, it becomes clear why the model underpredicts the activation overpotential if a change in *rds* is assumed. Therefore, electrochemical processes are attributed the the ohmic contact resistance as R_c is the fit value. Further investigations on the the nature of the reaction mechanisms are necessary to prove or rule out one of the presented options.

4. Conclusion

The effect of clamping pressure at various currents and temperatures on a state of the art PEM WE cell were investigated. Where a clear influence can already be seen in the polarization curves, electrochemical impedance spectroscopy and Tafel plots were utilized to further narrow down the analysis. Additionally, a mathematical model was utilized to extract exchange current density and contact resistance. The exchange current density seems to have an optimal value of compression at around 1.5 MPa, where the contact resistance decreases throughout the whole range of investigated compressions. That was further supported by ex-situ contact resistance measurements. Compared to the contacts, the membrane is the dominant contributor to the ohmic losses within the cell. A Tafel plot analysis revealed a certain disagreement in the literature. The proposed explanations include a change in rate determining step for the oxygen evolution reaction.

Besides the positive effect on cell performance, it should be kept in mind, that both increased temperature and compression may have a negative effect on the lifetime of the cell due to formation of hot spots. That is investigated in on-going work.

Acknowledgement

The authors would like to acknowledge the support by Innovation Fund Denmark through the e-STORE project, Grant 4106-00025B.

References

[1] International Energy Agency (IEA), Technology Roadmap: Hydrogen and Fuel Cells, Tech. rep., IEA (2015). doi:10.1007/SpringerReference_7300.
[2] A. Godula-Jopek, Hydrogen Production by Electrolysis, Wiley-VCH, 2015.
[3] F. Gutiérrez-Martín, I. Guerrero-Hernández, Balancing the grid loads by large scale integration of hydrogen technologies: The case of the Spanish power system, International Journal of Hydrogen Energy 37 (2) (2012) 1151–1161. doi:10.1016/j.ijhydene.2011.09.116.
[4] D. Bessarabov, H. Wang, H. Li, N. Zhao, PEM Electrolysis for Hydrogen Production - Principles and Applications, CRC Press, 2016.
[5] M. Carmo, D. L. Fritz, J. Mergel, D. Stolten, A comprehensive review on PEM water electrolysis, International Journal of Hydrogen Energy 38 (12) (2013) 4901–4934.
[6] F. Barbir, PEM electrolysis for production of hydrogen from renewable energy sources, Solar Energy 78 (5) (2005) 661–669. doi:10.1016/j.solener.2004.09.003.
[7] S. A. Grigoriev, V. I. Porembskiy, S. V. Korobtsev, V. N. Fateev, F. Aupre, P. Millet, High-pressure PEM water electrolysis and corresponding safety issues, International Journal of Hydrogen Energy 6 (2010) 3–10. doi:10.1016/j.ijhydene.2010.03.058.
[8] B. Bensmann, R. Hanke-Rauschenbach, I. K. Peña Arias, K. Sundmacher, Energetic evaluation of high pressure PEM electrolyzer systems for intermediate storage of renewable energies, Electrochimica Acta 110 (2013) 570–580. doi:10.1016/j.electacta.2013.05.102.
[9] F. N. Büchi, S. A. Freunberger, M. Reum, G. Paganelli, A. Tsukada, P. Dietrich, A. Delfino, On the efficiency of an advanced automotive fuel cell system, Fuel Cells 7 (2) (2007) 159–164. doi:10.1002/fuce.200500257.
[10] A. S. Arico, S. Siracusano, N. Briguglio, V. Baglio, A. Di Blasi, V. Antonucci, Polymer electrolyte membrane water electrolysis: Status of technologies and potential applications in combination with renewable power sources, Journal of Applied Electrochemistry 43 (2) (2013) 107–118. doi:10.1007/s10800-012-0490-5.
[11] C. A. Martinson, G. van Schoor, K. R. Uren, D. Bessarabov, Characterisation of a PEM electrolyser using the current interrupt method, International Journal of Hydrogen Energy 39 (36) (2014) 20865–20878. doi:10.1016/j.ijhydene.2014.09.153.
URL http://dx.doi.org/10.1016/j.ijhydene.2014.09.153
[12] X. Yuan, H. Wang, J. Colinsun, J. Zhang, AC impedance technique in PEM fuel cell diagnosisA review, International Journal of Hydrogen Energy 32 (17) (2007) 4365–4380. doi:10.1016/j.ijhydene.2007.05.036.
[13] J. Wu, X. Z. Yuan, H. Wang, M. Blanco, J. J. Martin, J. Zhang, Diagnostic tools in PEM fuel cell research: Part I Electrochemical techniques, International Journal of Hydrogen Energy 33 (6) (2008) 1735–1746. doi:10.1016/j.ijhydene.2008.01.013.
[14] C. Rozain, P. Millet, Electrochemical characterization of Polymer Electrolyte Membrane Water Electrolysis Cells, Electrochimica Acta 131 (2014) 160–167. doi:10.1016/j.electacta.2014.01.099.
URL http://dx.doi.org/10.1016/j.electacta.2014.01.099
[15] J. Van Der Merwe, K. Uren, G. Van Schoor, D. Bessarabov, Characterisation tools development for PEM electrolysers, International Journal of Hydrogen Energy 39 (26) (2014) 14212–14221. doi:10.1016/j.ijhydene.2014.02.096.
URL http://dx.doi.org/10.1016/j.ijhydene.2014.02.096
[16] H. Su, B. J. Bladergroen, S. Pasupathi, V. Linkov, S. Ji, Performance investigation of membrane electrode assemblies for hydrogen production by solid polymer electrolyte water electrolysis, International Journal of Electrochemical Science 7 (5) (2012) 4223–4234.
[17] B. S. Lee, H. Y. Park, I. Choi, M. K. Cho, H. J. Kim, S. J. Yoo, D. Henkensmeier, J. Y. Kim, S. W. Nam, S. Park, K. Y. Lee, J. H. Jang, Polarization characteristics of a low catalyst loading PEM water electrolyzer operating at elevated temperature, Journal of Power Sources 309 (2016) 127–134. doi:10.1016/j.jpowsour.2015.12.139.
URL http://dx.doi.org/10.1016/j.jpowsour.2015.12.139

[18] I. Dedigama, P. Angeli, K. Ayers, J. B. Robinson, P. R. Shearing, D. Tsaoulidis, D. J. L. Brett, In situ diagnostic techniques for characterisation of polymer electrolyte membrane water electrolysers - Flow visualisation and electrochemical impedance spectroscopy, International Journal of Hydrogen Energy 39 (9) (2014) 4468–4482. doi:10.1016/j.ijhydene.2014.01.026.
URL http://dx.doi.org/10.1016/j.ijhydene.2014.01.026
[19] S. Sun, Y. Xiao, D. Liang, Z. Shao, H. Yu, M. Hou, B. Yi, Behaviors of a proton exchange membrane electrolyzer under water starvation, RSC Adv. 5 (19) (2015) 14506–14513. doi:10.1039/C4RA14104K.
URL http://xlink.rsc.org/?DOI=C4RA14104K
[20] J. Millichamp, T. J. Mason, T. P. Neville, N. Rajalakshmi, R. Jervis, P. R. Shearing, D. J. L. Brett, Mechanisms and effects of mechanical compression and dimensional change in polymer electrolyte fuel cells - A review, Journal of Power Sources 284 (2015) 305–320. doi:10.1016/j.jpowsour.2015.02.111.
URL http://dx.doi.org/10.1016/j.jpowsour.2015.02.111
[21] S. Asghari, A. Mokmeli, M. Samavati, Study of PEM fuel cell performance by electrochemical impedance spectroscopy, International Journal of Hydrogen Energy 35 (17) (2010) 9283–9290. doi:10.1016/j.ijhydene.2010.03.069.
URL http://dx.doi.org/10.1016/j.ijhydene.2010.03.069
[22] A. Diedrichs, M. Rastedt, F. J. Pinar, P. Wagner, Effect of compression on the performance of a HT-PEM fuel cell, Journal of Applied Electrochemistry 43 (11) (2013) 1079–1099. doi:10.1007/s10800-013-0597-3.
[23] K. Elsøe, L. Grahl-Madsen, G. G. Scherer, J. Hjelm, M. B. Mogensen, Electrochemical Characterization of a PEMEC Using Impedance Spectroscopy, Journal of The Electrochemical Society 164 (13) (2017) F1419–F1426. doi:10.1149/2.0651713jes.
URL http://jes.ecsdl.org/lookup/doi/10.1149/2.0651713jes
[24] S. Siracusano, V. Baglio, S. A. Grigoriev, L. Merlo, V. N. Fateev, A. S. Arico, A PEM water electrolyser based on metallic Iridium electrocatalyst, Pt/C and Aquivion membrane (2017).
[25] A. Bates, S. Mukherjee, S. Hwang, S. C. Lee, O. Kwon, G. H. Choi, S. Park, Simulation and experimental analysis of the clamping pressure distribution in a PEM fuel cell stack, International Journal of Hydrogen Energy 38 (15) (2013) 6481–6493. doi:10.1016/j.ijhydene.2013.03.049.
URL http://dx.doi.org/10.1016/j.ijhydene.2013.03.049
[26] E. Alizadeh, M. Ghadimi, M. M. Barzegari, M. Momenifar, S. H. Saadat, Development of contact pressure distribution of PEM fuel cell's MEA using novel clamping mechanism, Energy 131 (2017) 92–97. doi:10.1016/j.energy.2017.05.036.
URL http://dx.doi.org/10.1016/j.energy.2017.05.036
[27] A. C. Olesen, S. K. Kær, The Effect of PFSA Membrane Compression on the Predicted Performance of a High Pressure PEM Electrolysis Cell, ECS Transactions 68 (3) (2015) 99–116. doi:10.1149/06803.0099ecst.
[28] R. O'Hayre, S.-W. Cha, W. Colella, F. B. Prinz, Fuel Cell Fundamentals, John Wiley and Sons, 2006.
[29] R. F. Mann, J. C. Amphlett, B. A. Peppley, C. P. Thurgood, Application of Butler Volmer equations in the modelling of activation polarization for PEM fuel cells, Journal of Power Sources 161 (2006) 775–781. doi:10.1016/j.jpowsour.2006.05.026.
[30] M. Suermann, T. J. Schmidt, F. N. Büchi, Cell Performance Determining Parameters in High Pressure Water Electrolysis, Electrochimica Acta 211 (2016) 989–997. doi:10.1016/j.electacta.2016.06.120.
[31] F. Marangio, M. Santarelli, M. Calì, Theoretical model and experimental analysis of a high pressure PEM water electrolyser for hydrogen production, International Journal of Hydrogen Energy 34 (3) (2009) 1143–1158. doi:10.1016/j.ijhydene.2008.11.083.
[32] Z. Abdin, C. J. Webb, E. M. Gray, Modelling and simulation of a proton exchange membrane (PEM) electrolyser cell, International Journal of Hydrogen Energy 40 (39) (2015) 13243–13257. doi:10.1016/j.ijhydene.2015.07.129.
URL http://dx.doi.org/10.1016/j.ijhydene.2015.07.129
[33] T. Hottinen, O. Himanen, S. Karvonen, I. Nitta, T. Hottinen, O. Himanen, M. Mikkola, S. Karvonen, I. Nitta, Inhomogeneous compression of PEMFC gas diffusion layer. Part II. Modeling the effect, Journal of Power Sources 171 (1) (2007) 113–121.
[34] C. Rozain, E. Mayousse, N. Guillet, P. Millet, Influence of iridium oxide loadings on the performance of PEM water electrolysis cells : Part I Pure IrO 2 -based anodes, "Applied Catalysis B, Environmental" 182 (2016) 153–160. doi:10.1016/j.apcatb.2015.09.013.
URL http://dx.doi.org/10.1016/j.apcatb.2015.09.013
[35] S. Siracusano, V. Baglio, E. Moukheiber, L. Merlo, A. S. Arico, Performance of a PEM water electrolyser combining an IrRu-oxide anode electrocatalyst and a shortside chain Aquivion membrane, International Journal of Hydrogen Energy 40 (42) (2015) 14430–14435. doi:10.1016/j.ijhydene.2015.04.159.
[36] T. a. Zawodzinski, Water Uptake by and Transport Through Nafion® 117 Membranes, Journal of The Electrochemical Society 140 (4) (1993) 1041. doi:10.1149/1.2056194.
[37] M. Chandesris, C. Robin, M. Gerard, Y. Bultel, Investigation of the difference between the low frequency limit of the impedance spectrum and the slope of the polarization curve, Electrochimica Acta 180 (2015) 581–590. doi:10.1016/j.electacta.2015.08.089.
URL http://dx.doi.org/10.1016/j.electacta.2015.08.089
[38] I. Pivac, F. Barbir, Inductive phenomena at low frequencies in impedance spectra of proton exchange membrane fuel cells - A review, Journal of Power Sources 326 (2016) 112–119. doi:10.1016/j.jpowsour.2016.06.119.
URL http://dx.doi.org/10.1016/j.jpowsour.2016.06.119
[39] A. M. Dhirde, N. V. Dale, H. Salehfar, M. D. Mann, T. H. Han, Equivalent electric circuit modeling and performance analysis of a PEM fuel cell stack using impedance spectroscopy, IEEE Transactions on Energy Conversion 25 (3) (2010) 778–786. doi:10.1109/TEC.2010.2049267.
[40] S. M. R. Niya, R. K. Phillips, M. Hoorfar, Process modeling of the impedance characteristics of proton exchange membrane fuel cells, Electrochimica Acta 191 (2016) 594–605. doi:10.1016/j.electacta.2016.01.128.
[41] M. A. Rubio, A. Urquia, R. Kuhn, S. Dormido, Electrochemical parameter estimation in operating proton exchange membrane fuel cells, Journal of Power Sources 183 (1) (2008) 118–125. doi:10.1016/j.jpowsour.2008.05.011.
[42] M. E. Orazem, N. Pebere, B. Tribollet, Enhanced Graphical Representation of Electrochemical Impedance Data, Journal of The Electrochemical Society 153 (4) (2006) 129. doi:10.1149/1.2168377.
[43] P. Córdoba-Torres, T. J. Mesquita, O. Devos, B. Tribollet, V. Roche, R. P. Nogueira, On the intrinsic coupling between

constant-phase element parameters ?? and Q in electrochemical impedance spectroscopy, Electrochimica Acta 72 (2012) 172–178. doi:10.1016/j.electacta.2012.04.020.
URL http://dx.doi.org/10.1016/j.electacta.2012.04.020

[44] H. Ito, T. Maeda, A. Nakano, H. Takenaka, Properties of Nafion membranes under PEM water electrolysis conditions, International Journal of Hydrogen Energy 36 (17) (2011) 10527–10540. doi:10.1016/j.ijhydene.2011.05.127.
URL http://dx.doi.org/10.1016/j.ijhydene.2011.05.127

[45] Q. Feng, X. Yuan, G. Liu, B. Wei, Z. Zhang, H. Li, H. Wang, A review of proton exchange membrane water electrolysis on degradation mechanisms and mitigation strategies, Journal of Power Sources 366 (2017) 33–55. doi:10.1016/j.jpowsour.2017.09.006.
URL http://dx.doi.org/10.1016/j.jpowsour.2017.09.006

[46] P. Lettenmeier, S. Kolb, F. Burggraf, A. S. Gago, K. A. Friedrich, Towards developing a backing layer for proton exchange membrane electrolyzers, Journal of Power Sources 311 (2016) 153–158. doi:10.1016/j.jpowsour.2016.01.100.
URL http://dx.doi.org/10.1016/j.jpowsour.2016.01.100

[47] E. Brightman, J. Dodwell, N. Van Dijk, G. Hinds, In situ characterisation of PEM water electrolysers using a novel reference electrode, Electrochemistry Communications 52 (2015) 1–4. doi:10.1016/j.elecom.2015.01.005.
URL http://dx.doi.org/10.1016/j.elecom.2015.01.005

[48] K. S. Kadakia, P. Jampani, O. I. Velikokhatnyi, M. K. Datta, S. J. Chung, J. a. Poston, A. Manivannan, P. N. Kumta, Nanostructured (Ir,Sn)O2:F - Oxygen Evolution Reaction Anode Electro-Catalyst Powders for PEM Based Water Electrolysis, Journal of the Electrochemical Society 161 (9) (2014) F868–F875. doi:10.1149/2.0381409jes.
URL http://jes.ecsdl.org/cgi/doi/10.1149/2.0381409jes

[49] Gamry Instruments, Understanding iR Compensation (2017).

[50] A. J. Bard, G. Inzelt, F. Scholz, Electrochemical dictionary, Springer-Verlag, 2008.

[51] M. Bernt, H. A. H. Gasteiger, Influence of Ionomer Content in IrO 2 /TiO 2 Electrodes on PEM Water Electrolyzer Performance, Journal of The Electrochemical Society 163 (11) (2016) F3179–F3189. doi:10.1149/2.0231611jes.
URL http://jes.ecsdl.org/lookup/doi/10.1149/2.0231611jes

[52] J. Bockris, Z. Nagy, Symmetry Factor and Transfer Coefficient, Journal of Chemical Education.

[53] M. Noel, K. Vasu, Charge Tranfer Kinetics and Diffusion, in: Cyclic Voltammetry and the Frontiers of Electrochemistry, Oxford & IBH Publishing Co. Pvt. Ltd., New Delhi, 1990, pp. 157–194.
URL http://noel-cyclic-voltametric-one.tripod.com/cvm/Chapter-4.PDF

[54] R. Guidelli, R. G. Compton, J. M. Feliu, E. Gileadi, J. Lipkowski, W. Schmickler, S. Trasatti, Defining the transfer coefficient in electrochemistry: An assessment (IUPAC Technical Report), Pure and Applied Chemistry 86 (2) (2014) 245–258. doi:10.1515/pac-2014-5026.
URL http://www.degruyter.com/view/j/pac.2014.86.issue-2/pac-2014-5026/pac-2014-5026.xml

[55] J. M. Hu, J. Q. Zhang, C. N. Cao, Oxygen evolution reaction on IrO2-based DSA?? type electrodes: Kinetics analysis of Tafel lines and EIS, International Journal of Hydrogen Energy 29 (8) (2004) 791–797. doi:10.1016/j.ijhydene.2003.09.007.

[56] E. Slavcheva, I. Radev, S. Bliznakov, G. Topalov, P. Andreev, E. Budevski, Sputtered iridium oxide films as electrocatalysts for water splitting via PEM electrolysis, Electrochimica Acta 52 (12) (2007) 3889–3894. doi:10.1016/j.electacta.2006.11.005.

[57] U. Babic, M. Suermann, F. N. Büchi, L. Gubler, T. J. Schmidt, Critical ReviewIdentifying Critical Gaps for Polymer Electrolyte Water Electrolysis Development, Journal of The Electrochemical Society 164 (4) (2017) F387–F399. doi:10.1149/2.1441704jes.
URL http://jes.ecsdl.org/lookup/doi/10.1149/2.1441704jes

[58] M. V. Williams, H. R. Kunz, J. M. Fenton, Analysis of Polarization Curves to Evaluate Polarization Sources in Hydrogen/Air PEM Fuel Cells, Journal of The Electrochemical Society 152 (3) (2005) A635. doi:10.1149/1.1860034.

[59] K. C. Neyerlin, W. Gu, J. Jorne, H. A. Gasteiger, Determination of Catalyst Unique Parameters for the Oxygen Reduction Reaction in a PEMFC, Journal of The Electrochemical Society 153 (10) (2006) A1955. doi:10.1149/1.2266294.
URL http://jes.ecsdl.org/cgi/doi/10.1149/1.2266294

Paper B

Model-supported Analysis of Degradation Phenomena of a PEM Water Electrolysis Cell under Dynamic Operation

Steffen Henrik Frensch, Anders Christian Olesen, Samuel Simon Araya, Søren Knudsen Kær

The paper has been published in
ECS Transactions Vol. 85 (11), pp. 37–45, 2018.

Model-supported Analysis of Degradation Phenomena of a PEM Water Electrolysis Cell under dynamic Operation

Steffen Henrik Frensch[a,*], Anders Christian Olesen[a], Samuel Simon Araya[a], Søren Knudsen Kær[a]

[a]*Aalborg University, Department of Energy Technology, Pontoppidanstræde 111, 9220 Aalborg Øst, Denmark*

Abstract

In this study, a small PEM water electrolysis single cell set up is utilized to extract information about degradation mechanisms. The major parameter of interest is the operational condition, which is changed from constant to cycling current input signal throughout a period of just over 1000 h. The cell shows a high reversible share of the voltage increase at constant operation, which builds up slowly and can be recovered through a short interruption of cell operation. Impedance measurements reveal a considerable change in ohmic contributions as well as electrochemical performance over time. The model supported IV curve analysis backs the impedance data and reveals an increase in contact resistances. At the same time, the electrochemical surface area on both electrodes is reduced. The results suggest that dynamic operation may be beneficial for cell performance and therefore operational cost, while a degradation rate of 164.1 $\mu V\,h^{-1}$ was calculated.

Keywords: PEM water electrolysis, Degradation, Impedance spectroscopy, Reversible Irreversible, Operation Strategy

1. Introduction

Hydrogen production through polymere electrolyte membrane water electrolysis (PEM WE) is considered as an emerging technology. Two of the major applications are hydrogen production for industrial processes and water electrolysis as a part of a future energy system. Concerning the first, the worldwide hydrogen demand is mostly met by steam reforming of hydrocarbons or alcohols [1]. This process emits greenhouse gases such as CO_2. As many climate policies go towards decarbonization, an alternative source of hydrogen has to be employed. If fed by renewable energy sources, water electrolysis can be considered CO_2 neutral.

The second application as a part of an energy system includes energy storage as well as grid services. Hydrogen can be stored as a gas or liquid and converted back into electrical energy in fuel cells or utilized for the production of other fuels such as syngas. The PEM technology offers certain characteristics that make it interesting for grid balancing and frequency stabilization. A fast response time to changing operation parameters and fast start/stop operation are crucial specifically for providing grid services. Additionally, the produced hydrogen can be pressurized internally. That makes further compression cheaper or even redundant while lowering the system complexity and cost [2]. Although the technology can be considered mature, a wide implementation can not be observed. The relatively high cost is one of the major obstacles that hinders an accelerated implementation.

Furthermore, durability under highly dynamic operation has yet to be proven, specifically under the aspect of integrating the technology into the electrical grid. The research towards long-term tests is increasing in the last years. Where acceptable voltage increase rates have been reported under constant operation at moderate current density, dynamic operation and and accelerated stress tests are still sparse [3, 4]. A comparative study between operation modes has been conducted and suggest that cycling operation may be beneficial for durability [5]. This work tries

*Corresponding author

Email addresses: stf@et.aau.dk (Steffen Henrik Frensch), aco@et.aau.dk (Anders Christian Olesen), ssa@et.aau.dk (Samuel Simon Araya), skk@et.aau.dk (Søren Knudsen Kær)

to confirm the findings by investigating the behavior of a PEM electrolysis cell under constant and cycling current operation, while focusing on reversible and irreversible voltage increase. It is seen as a step towards coupled operation with fluctuating renewable energy sources.

2. Methodology

All tests presented in this work are carried out on a single cell set-up. A commercial Nafion 117 membrane is used as the solid electrolyte. On the cathode side, where the hydrogen is produced, carbon-supported platinum functions as a catalyst layer with a loading of 0.5 mg cm^{-2}. A carbon cloth acts as a porous transport layer (PTL) and ensures decent current distribution. The anode side consists of a 0.3 mg cm^{-2} Iridium oxide layer followed by an Iridium contact layer with a loading of 2.48 mg cm^{-2} and a titanium felt as a PTL. The MEAs (membrane-electrode-assemblies) are delivered by EWII Fuel Cells A/S (Denmark). A cell compression of 2.30 MPa was chosen based on a previous study on clamping pressure [6]. De-ionized (DI) water is fed to the anode at a constant flow rates of around 270 mL min^{-1}. That represents high overstoichiometry in any operation point and ensures fast heat removal from the cell since the operation temperature is controlled by the pre-heated feed water. Furthermore, an interdigitated flow field is applied to enhance mass transport. A Gamry Reference 3000 potentiostat/galvanostat together with a current booster acts as the power supply for the cell. The device is furthermore utilized to record polarization curves and impedance data. All measurements are done in a two electrode set-up. Cell voltage and current as well as anode and cathode temperatures are monitored throughout the whole experiment. Figure 1 illustrates the experimental set-up.

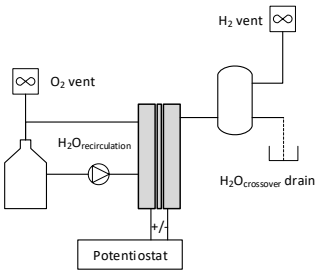

Figure 1: Test set-up

Electrochemical impedance spectroscopy (EIS) and polarization (IV) curves are recorded after every 24 h of operation. Polarization curves are measured in ascending direction in flexible steps from 0.01 A cm^{-2} to 3.0 A cm^{-2}. Each operation point is held for 120 s to achieve steady state. Where applicable, galvanostatic EIS measurements are done after the polarization measurement. EIS measurements range from 60 000 Hz to 0.1 Hz with 10 points per decade. On top of the DC current, an AC disturbance current is imposed to the cell with a value of 5% with respect to the DC operation point. All fits are done based on an equivalent circuit consisting of two parallel resistor-constant phase element circuits in series with an ohmic resistance and an ohmic resistor in parallel with an inductance. Furthermore, the polarization data is fit to a model in order to extract parameters such as contact resistances (R_c and exchange current density (i_0). In order to facilitate the analysis, some simplifications were made in our previous work [6], such as not resolving the catalyst layer. To evaluate the contact resistances more precisely, the present work does not assume these simplifications and the applied model corresponds in general with the one presented in a former publication, where a complete description can be found [7]. It is based on the approach of modelling the cell voltage by utilizing the Nernst equation raised by losses due to activation processes through Butler-Volmer and ohmic losses.

During the whole period of the test, the cell was held constant at 60 °C. In the initial period of 504 h (3 weeks), the applied current density was held constant at 1.5 A cm^{-2}. In the following 504 h, the current density was cycled

between 1.0 A cm^{-2} and 2.0 A cm^{-2}, holding each value for 1 h. Between the two operation modes, the cell was only interrupted to change the automated script.

3. Results and Discussion

The analysis is based on the voltage profile over time, and model-supported interpretation of IV and impedance data. For the whole period of the test at both constant and cycling operation, the cell voltage was monitored. Figure 2a shows the whole time span of the constant current period, figure 2b shows the cycling period only as an extract of 200 h for better visibility.

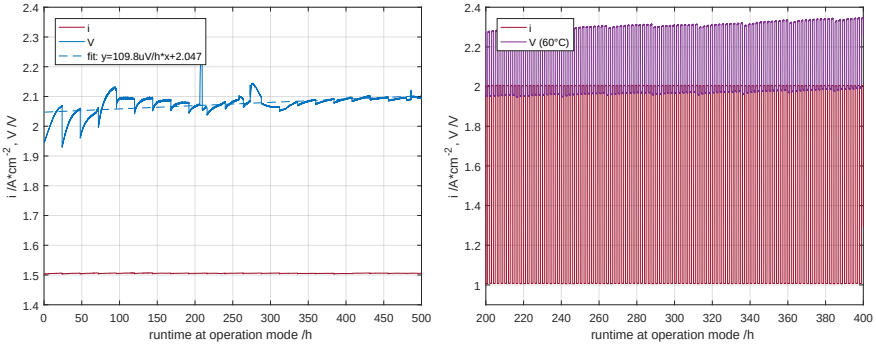

(a) Constant current, 0 h to 504 h

(b) Cycling, extract from 200 h to 400 h for better visibility

Figure 2: Voltage profiles for both operation modes

3.1. Reversible Voltage Increase

It can be seen that the voltage increases during the constant operation over time. A linear fit for the whole data set was applied and included in the figure. The slope of the fitting curve is 109.8 µV h^{-1} and can be interpreted as a first estimation of the voltage increase rate. However, the actual voltage profile reveals, that a linear approximation may not be sufficient to describe the degradation. Firstly, the performance decay rate seems to decrease over time. That is, a logarithmic fit may be utilized. Secondly, the profile shows that a considerable share of the voltage increase is reversible and is recovered after each characterization. At this point, it is important to point out, that also the constant operation mode is in fact interrupted frequently by a characterization. Last but not least, the voltage profile alone cannot reveal insights about the the underlying degradation phenomena. Figure 3b illustrates the reversible and the irreversible shares of the absolute voltage increase during the respective past 24 h at constant operation. As mentioned before, the total voltage increase over 24 h decreases throughout operation time, and so does the reversible share. The reversible and irreversible shares are calculated according to equations 1 and 2 (see figure 3a for graphical explanation).

$$V_{rev}(t) = V(t, end) - V(t+1, start) \tag{1}$$

$$V_{irrev}(t) = V(t+1, start) - V(t, start) \tag{2}$$

As figure 3c shows, the share of the reversible voltage increase of the total increase does not show a clear trend over time, suggesting that it does not change systematically. Similar long term experiments are scarce and only few

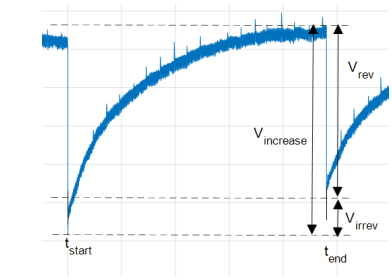

(a) Explanation of terms and timestamps

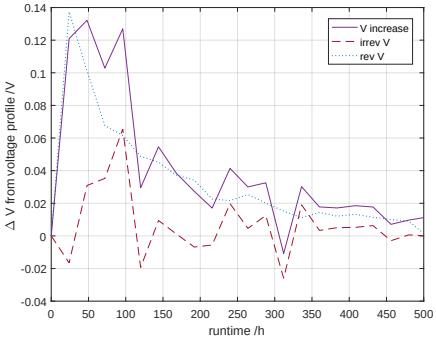

(b) Total voltage increase and the respective reversible and irreversible shares over time

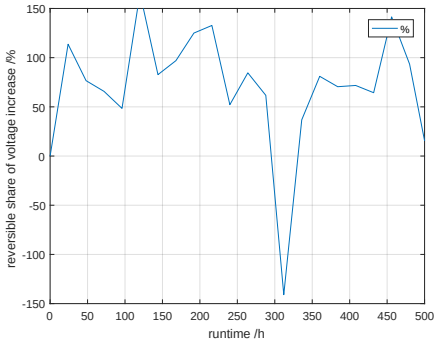

(c) Relative reversible share of total voltage increase over time

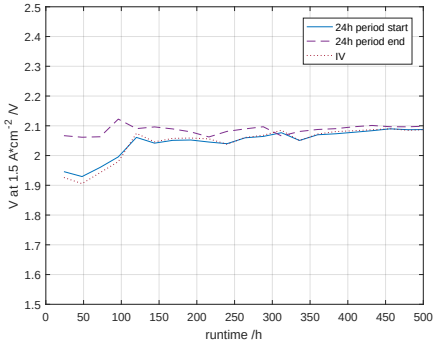

(d) Potential at 1.5 A cm^{-2} measured at the beginning and end of each 24 h period compared to measurement during IV curve

Figure 3: Reversible voltage increase

publications focus on reversible voltage increase. However, the phenomenon of voltage relaxation after an interruption is reported for both PEM fuel cells and electrolysis [8, 9, 10]. In this work, a flow field based on interdigitated channels on the anode side is utilized. The cell design supposedly enhances mass transport by forcing all feed water through the PTL in order to reach the outlet channels together with the produced oxygen bubbles [11, 12]. However, with the results from this long term test, the high reversible share may be explain by this very flow field design. Produced oxygen bubbles may travel from the three-phase boundary at the catalyst layer through the PTL and get trapped in the end of one of the inlet channels. The bubbles then block the channels for the feed water, leaving a less active area behind. After 24 h, the current is interrupted by the IV measurement starting at low current densities. This process may act as a resting period, where the trapped bubbles are flushed out of the channel and leave the cell. Since the whole active area can be utilized again after the characterization, the potential decreases accordingly. This assumption is supported by comparing the potential from the profile to the potential from the IV curves at 1.5 A cm^{-2}, which is shown in figure 3d. It can be seen that the measured potential from the IV is very close to the value taken from the profile at the beginning of each 24 h period. This implies that the reason for the reversible voltage increase is immediately recovered when changing to lower current and potential, and only slowly builds up over time again. It also implies that only the irreversible share of the voltage increase can be captured by the IV curve. Reversible voltage

increase was previously connected to the change in Ti-PTL resistance with applied potential in the literature [9]. The time interval for maximum Ti-dissolution is supposedly longer than the holding time for each current step in this work [13], therefore the effect would be expected to be captured by the IV curve. However, this was not the case and therefore would be in support of the suspicion that the reversible increase is not of ohmic nature, but related to mass transport, which the authors also state as a possibility. The cycling operation that was applied in the second half of the experiment may have a similar effect as the change in applied current during characterization. The sudden drop/raise between 1.0 A cm^{-2} and 2.0 A cm^{-2} can partly recover the voltage. During the cycling time of 1 h, the possibility of building up a higher potential is limited. Since the hydrogen production rate is a function of applied current, but not potential, that has an impact on the specific energy consumption per unit hydrogen (in J mol^{-1}) and therefore on the production cost. However, a certain share of the voltage increase is not recovered, and therefore decreases these two values over time.

3.2. Irreversible Voltage Increase

To get more insight into the irreversible voltage increase (i.e. performance degradation), figure 4a shows the evolution of the polarization curves over time. The plot shows the curves after each week (168 h) of operation. It can clearly be seen that the performance is decreasing over time. The most obvious step can be observed from the beginning of life to the next recorded IV curve. The measurements in between (not shown here) reveal that, after a slight increase in performance after 24 h, the performance decreases relatively steep in the following days. The performance decrease is then slowed down as it can be seen from the plotted curves after 1, 2, and 3 weeks. The slight increase in performance within the first 24 h can be connected to activation processes such as full humidification of the membrane, which is a fast process [14]. A further separation between degradation processes can be achieved through the analysis of EIS data.

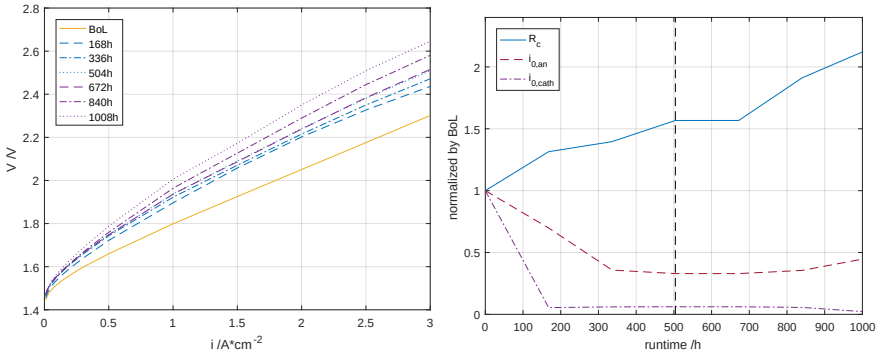

(a) Polarization curve evolution over time

(b) Normalized extracted fit parameters from IV curve model

Figure 4: Polarization curve analysis

Reversible voltage increase cannot be captured through EIS within the present methodology since the measurement was made together with the polarization curve in one characterization interruption. Therefore, the impedance data is utilized to analyze the irreversible degradation. Figure 5 shows the evolution of the HFR (high frequency resistance), LFR (low frequency resistance), and the IV slope for comparison. The HFR and LFR are defined as the intercept of the Nyquist plot with the x-axis at high frequencies and low frequencies, respectively. Additionally, the difference between LFR and HFR is plotted.

The evolution of the HFR within the initial phase of operation (<100 h) support the observations from the IV curves. After an initial drop, the HFR increases steeply. A better performance due to better ion conduction in Nafion at higher humidification can explain the initial drop [14], and the following increase indicates an increase in ohmic

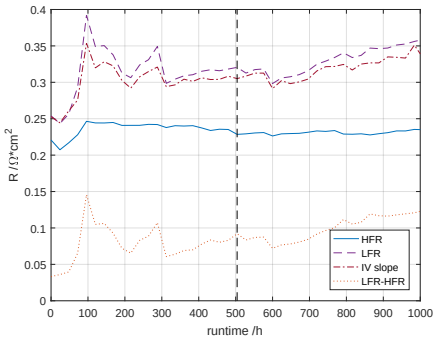

Figure 5: HFR, LFR, and IV slope evolution over time

resistance of the cell. The extracted parameters from the IV curve model fit are shown in figure 4b and support the general trends that were described before. The figure presents the evolution of contact resistances and apparent exchange current densities normalized by the initial value. It reveals an increase in contact resistance of around 32% within the first week, which may be connected to the passivation of the Ti-PTL at the anode side. At the same time, the apparent exchange current densities at anode and cathode are decreasing as seen in figure 4b. After a steep initial drop within the first 200 h-300 h, their values stabilize. This decrease is connected to a decrease in electrochemical surface area (ECSA). Possible reasons for that need further investigations, but it may be speculated that the number of active sites is reduced due to geometrical changes in the cathode side carbon transport layer. That can be caused by an increase in effective cell compression due to thermal expansion of the components, or a delayed effect of the membrane swelling due to water uptake within the first hours, since the cell was assembled dry. Furthermore, particle agglomeration and/or loss on both electrodes may decrease ECSA as well as surface coverage phenomena. Besides the presented bubble formation, that is assumed to be reversible, other species may block access to the active sites. The evolution of both contact resistance and exchange current density is in line with the literature [5].

The decrease in apparent exchange current is also underlined by the evolution of the LFR as seen in figure 5. As expected, the the LFR and the IV slope at 1.5 A cm^{-2} coincide well. It can be observed, that both follow a very similar trend and are similar in absolute value as well. Additionally to the LFR evolution, the difference between HFR and LFR is shown in the figure. Since the HFR was previously connected to the membrane and contact resistances, the difference between the two may reveal an insight into the other components of the cell. The increase in difference between LFR and HFR indicates the non-ohmic contribution of the loss of ECSA on both electrodes.

During cycling operation, the exchange current densities do not change significantly until the end of the test. This stagnation cannot necessarily be connected to the operation mode, but is more likely a function of time. Further investigations on activation processes on different MEAs are necessary to draw more conclusions. However, the contact resistance continues to increase also during the cycling experiment. The overall slope of increase seems relatively constant and linear throughout the whole 1008 h. Both findings indicate that cycling operation does not have a significant impact on these parameters. However, the evolution of IV curves in figure 4a together with the increase of the LFR after 504 h in figure 5 suggest that the operation mode does affect degradation. Further experiments have to carried out in order to identify the mechanisms and exclude the factor time as the cause.

3.3. Performance Degradation Rate

In order to compare different cells and operation modes, degradation rates can be calculated from either the IV curves or the profile at constant operation. Figure 6a shows the degradation rate in µV h^{-1} calculated from IV curves at different potentials, and figure 6b compares the value at 1.5 A cm^{-2} to the degradation rate calculated from the voltage profile at constant operation with respect to the potential at the beginning of life. As a first observation, these two values coincide very well, which can be seen as a sign for the integrity of the recorded data.

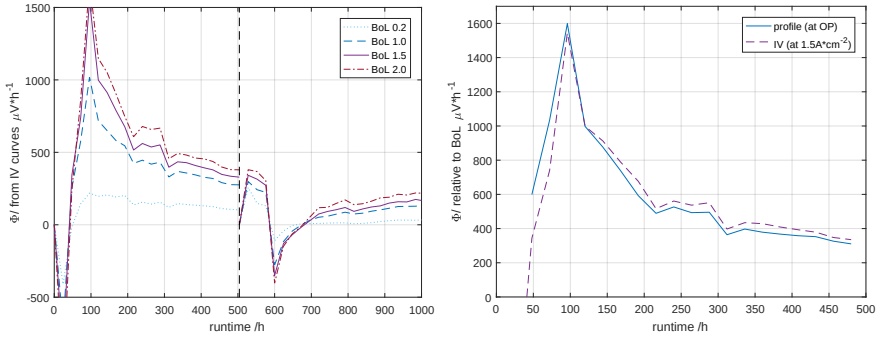

(a) Degradation rate calculated from IV curves at different potentials

(b) Degradation rates at constant operation at 1.5 A cm^{-2} calculated from IV curves compared to profile

Figure 6: Degradation rates

The shown values in figure 6b are with respect to the beginning of test (0 h for constant and 504 h for cycling). It can be seen, that the degradation is more pronounced at higher current especially at early stages of the experiment. This implies that the degradation is dominantly of ohmic nature, which is in line with the previous findings. The degradation at constant operation at 1.5 A cm^{-2} with a value of around 328.6 µV h^{-1} is very high compared to the literature [15, 9, 5]. However, as figure 6a shows, the degradation rate is highly changing with time. That is, the initial degradation rates are very high. When considering an activation phase of 4 days (from where on the degradation rate decreases significantly), the degradation rate at the end of the test is 125.1 µV h^{-1} (with respect to the potential at 168 h). Besides being similar to the first estimation of the linear fit approach of 109.8 µV h^{-1}, this value is more comparable to reported experiments. Why this cell shows a relatively high degradation can explained by two reasons. Firstly, the anode PTL is not coated, which would reportedly prevent Ti passivation [9]. Furthermore, the fact that the feed water is recirculated, increases water impurities. Although the feed water tank is replaced manually throughout the test period several times, conductivity measurements reveal a rise in conductive ions within the water. However, when the initial performance drop is neglected, the performance degradation is within the state of the art. The degradation rate at the end of the cycling experiment with respect to the beginning of the cycling test is 164.1 µV h^{-1}. With the stated considerations taken into account, the number is comparable to constant operation.

4. Conclusion

A long term degradation test of more than 1000 h was carried out on a single cell PEM WE. During constant operation at 1.5 A cm^{-2}, a considerable share of reversible voltage increase was observed. An explanation may be found in the accumulation of oxygen bubbles within the anode side flow field channels, which are flushed out during changes in potential. Therefore, a cycling operation may be beneficial. Furthermore, IV curve model fit parameters reveal that the ohmic resistances increase over time, while the exchange current densities for the anode and cathode decrease. The causes of voltage increase were therefore identified as Ti-PTL passivation and a decrease of ECSA at both electrodes. A quantitative evaluation of performance degradation led to rates of 125.1 µV h^{-1} and 164.1 µV h^{-1} for constant and cycling operation, respectively.

Acknowledgement

The authors would like to acknowledge the support by Innovation Fund Denmark through the e-STORE project, Grant 4106-00025B.

References

[1] A. Godula-Jopek, Hydrogen Production by Electrolysis, Wiley-VCH, 2015.

[2] B. Bensmann, R. Hanke-Rauschenbach, I. K. Peña Arias, K. Sundmacher, Energetic evaluation of high pressure PEM electrolyzer systems for intermediate storage of renewable energies, Electrochimica Acta 110 (2013) 570–580. doi:10.1016/j.electacta.2013.05.102.

[3] E. Anderson, K. Ayers, C. Capuano, R & D Focus Areas Based on 60 , 000 hr Life PEM Water Electrolysis Stack Experience p Proton OnSite Manufacturer of packaged products , systems, First International Workshop on Durability and Degradation Issues in PEM Electrolysis Cells and its Components (March).

[4] F. Fouda-Onana, M. Chandesris, V. Médeau, S. Chelghoum, D. Thoby, N. Guillet, Investigation on the degradation of MEAs for PEM water electrolysers part I: Effects of testing conditions on MEA performances and membrane properties, International Journal of Hydrogen Energy (41) (2016) 16627–16636. doi:10.1016/j.ijhydene.2016.07.125.

[5] C. Rakousky, U. Reimer, K. Wippermann, S. Kuhri, M. Carmo, W. Lueke, D. Stolten, Polymer electrolyte membrane water electrolysis: Restraining degradation in the presence of fluctuating power, Journal of Power Sources 342 (2017) 38–47. doi:10.1016/j.jpowsour.2016.11.118.
URL http://dx.doi.org/10.1016/j.jpowsour.2016.11.118

[6] S. H. Frensch, A. C. Olesen, S. S. Araya, S. K. Kær, Model-supported characterization of a PEM water electrolysis cell for the effect of compression, Electrochimica Actadoi:10.1016/j.electacta.2018.01.040.
URL https://doi.org/10.1016/j.electacta.2018.01.040

[7] A. C. Olesen, S. K. Kær, The Effect of PFSA Membrane Compression on the Predicted Performance of a High Pressure PEM Electrolysis Cell, ECS Transactions 68 (3) (2015) 99–116. doi:10.1149/06803.0099ecst.

[8] M. Chandesris, T. Jahnke, M. Zago, T. A. Aarhaug, P. Schott, M. Baum, Investigation of permanent and reversible degradations in PEMFC and DMFC stationary applications using statistical and modelling tools, in: Modval13, 2016, p. 621216.

[9] C. Rakousky, U. Reimer, K. Wippermann, M. Carmo, W. Lueke, D. Stolten, An analysis of degradation phenomena in polymer electrolyte membrane water electrolysis, Journal of Power Sources 326 (2016) 120–128. doi:http://dx.doi.org/10.1016/j.jpowsour.2016.06.082.
URL http://www.sciencedirect.com/science/article/pii/S0378775316307844

[10] W. Schmittinger, A. Vahidi, A review of the main parameters influencing long-term performance and durability of PEM fuel cells, Journal of Power Sources 180 (2008) 1–14. doi:10.1016/j.jpowsour.2008.01.070.

[11] T. V. Nguyen, A gas distributor design for proton-exchange-membrane fuel cells, Journal of The Electrochemical Society 143 (5) (1996) L103–L105. doi:Doi 10.1149/1.1836666.

[12] D. L. Wood, Y. S. Yi, T. V. Nguyen, Effect of direct liquid water injection and interdigitated flow field on the performance of proton exchange membrane fuel cells, Electrochimica Acta 43 (24) (1998) 3795–3809. doi:10.1016/S0013-4686(98)00139-X.

[13] S. Cherevko, T. Reier, A. R. Zeradjanin, Z. Pawolek, P. Strasser, K. J. Mayrhofer, Stability of nanostructured iridium oxide electrocatalysts during oxygen evolution reaction in acidic environment, Electrochemistry Communications 48 (2014) 81–85. doi:10.1016/j.elecom.2014.08.027.
URL http://dx.doi.org/10.1016/j.elecom.2014.08.027

[14] T. a. Zawodzinski, Water Uptake by and Transport Through Nafion® 117 Membranes, Journal of The Electrochemical Society 140 (4) (1993) 1041. doi:10.1149/1.2056194.

[15] P. Lettenmeier, R. Wang, R. Abouatallah, S. Helmly, T. Morawietz, R. Hiesgen, S. Kolb, F. Burggraf, J. Kallo, A. S. Gago, K. A. Friedrich, Durable Membrane Electrode Assemblies for Proton Exchange Membrane Electrolyzer Systems Operating at High Current Densities, Electrochimica Acta 210 (2016) 502–511. doi:10.1016/j.electacta.2016.04.164.
URL http://dx.doi.org/10.1016/j.electacta.2016.04.164

Paper C

Influence of the Operation Mode on PEM Water Electrolysis Degradation

Steffen Henrik Frensch, Frédéric Fouda-Onana, Guillaume Serre, Dominique Thoby, Samuel Simon Araya, Søren Knudsen Kær.

The paper has been submitted to the
International Journal of Hydrogen Energy.

submitted to an Elsevier Ltd. journal

Influence of the Operation Mode on PEM Water Electrolysis Degradation

Steffen Henrik Frensch[a,*], Frédéric Fouda-Onana[b], Guillaume Serre[b], Dominique Thoby[b], Samuel Simon Araya[a], Søren Knudsen Kær[a]

[a]*Aalborg University, Department of Energy Technology, Pontoppidanstræde 111, 9220 Aalborg Øst, Denmark*
[b]*CEA, LITEN, DEHT, F-38054, Grenoble, France*

Abstract

Since realistic operation scenarios for polymer electrolyte membrane water electrolysis (PEM WE) systems may be dynamic, this study compares the performance over time for seven different operation modes. Besides the effect of temperature, constant and dynamic current profiles were investigated, including cycling operation and the simulation of a solar profile. It was found that fast current switches improved the overall cell performance over the test period of 500 h. The major cause for this was a decrease in total ohmic resistance, which was also observed during the break-in phase preceding the experiments. This decrease can partly be explained by membrane thinning and partly by an improvement in contacts between the components. Dynamic operation led to more severe fluoride emission from the catalyst binder, which improved the performance in terms of cell potential. However, it could be a concern for long term degradation as membrane thinning promotes higher gas crossover. All other operation modes on the other hand suffered from an increase in total ohmic resistance, leading to an overall performance decrease. This was connected to the passivation of Ti components. Higher temperature was found to be advantageous for performance, but disadvantageous in terms of both membrane thinning and passivation processes.

Keywords: PEM water electrolysis aging, Membrane Degradation, Dynamic operation mode, Durability, Break-in

1. Introduction

Hydrogen may play an important role in future energy systems. With the transition from fossil fuels to fluctuating energy sources such as solar and wind comes an increase in fluctuation of power input. Due to its multiple applications in this context, hydrogen production through polymer electrolyte membrane water electrolysis (PEM WE) is a subject of increasing attention [1]. The technology may be utilized for energy storage by producing hydrogen for a later use to convert it back into electrical energy or thermal energy. Besides using gaseous hydrogen directly for example in PEM fuel cells (FC), it can also be part of power-to-x systems including syngas or liquid fuels such as methanol [2, 3]. Furthermore, due to certain advantages, PEM electrolysis may take over grid services such as frequency stabilization [1], that were previously provided by conventional thermal turbines through their inertia. Last but not least, water electrolysis presents an alternative to natural gas reforming for industrial hydrogen production that is potentially CO_2 neutral.

Although the PEM technology for both fuel cells and electrolysis is well researched, a wide market implementation is not yet observed. One of the biggest challenges is the high cost of production, which has to be addressed both by lowering material cost and by extending the useful lifetime of the system. An increasing amount of literature is available on the topic, but especially degradation under dynamic operation has a demand for more research. The most comprehensive work with the focus on dynamic operation can be found in [4], where the authors compare different operation modes in terms of degradation rates. The work includes the contributions of anode and cathode through

*Corresponding author

Email addresses: stf@et.aau.dk (Steffen Henrik Frensch), frederic.fouda-onana@cea.fr (Frédéric Fouda-Onana), guillaume.serre@cea.fr (Guillaume Serre), dominique.thoby@cea.fr (Dominique Thoby), ssa@et.aau.dk (Samuel Simon Araya), skk@et.aau.dk (Søren Knudsen Kær)

an implemented reference electrode and comes to the conclusion, that cycling operation may be beneficial in terms of hydrogen-output-normalized degradation rates. It is based on their previous work, where the major degradation cause in constant operation was identified as passivation of the porous transport layer (PTL) made of titanium due to oxidation [5]. Ti-PTL passivation together with membrane thinning was also found by other authors [6].

Other causes of degradation under constant operation were observed in the anode catalyst layer (CL) [7] and from impurities within the ionomer (membrane and catalyst layer) from the feed water, which increase ionic and charge transfer resistance [8]. PEM fuel cell degradation studies showed the proof of concept to utilize fluoride emission as an indicator for membrane degradation [9]. Since the used membrane in PEM WE is often very similar in its structure and only differs in thickness, the method can also be applied for electrolysis and was already shown in a previous publication [6]. Fluoride in the effluent water must originate from the Nafion® ionomer either in the membrane or the catalyst layers, and can be correlated to the membrane degradation [10, 6].

This work provides a systematic study of the effect of dynamic operation of PEM WE on degradation. Fast cycling operation as well as direct coupling to a photovoltaic system is investigated to simulate PEM WE participation in the grid. Furthermore, the effect of elevated temperature is investigated, as operation above 80 °C is desirable in terms of efficiency and commercialization [11].

2. Methodology

2.1. Experimental Set-Up

All experiments were carried out on a single cell set-up. The catalyst inks and membrane-electrode-assemblies (MEAs) with an active area of 25 cm^2 were produced in house. The circular electrodes were sprayed on Teflon® sheets and transferred onto a Nafion® 115 (N115) membrane through hot-pressing. The transfer was done at 170 °C for 5 min at 300 kg followed by 2 min at 2000 kg. The MEA for a high temperature experiment is an exception, where Nafion® 117 (N117) was used to avoid gas crossover rates at dangerous levels. The cathode, where the hydrogen evolution reaction (HER) takes place, is based on 1.0 mg cm^{-2} carbon-supported platinum (Tanaka TEC10V50E), the anode for the oxygen evolution reaction (OER) consists of 2.3 mg cm^{-2} iridium-oxide (Surepure Chemetals). Commercial SGL Sigracet® 28BC carbon sheet and a 1 mm titanium sinter (Accumet, 30% porosity) act as the porous transport layer (PTL) on the cathode and anode, respectively. Both flow fields with parallel channels were made of titanium.

An external power supply was used to monitor current and voltage during the tests. All electrochemical characterizations were carried out on a Biologic® HCP-803 potentiostat, which replaced the external power supply during each characterization phase. Figure 1 illustrates the set-up.

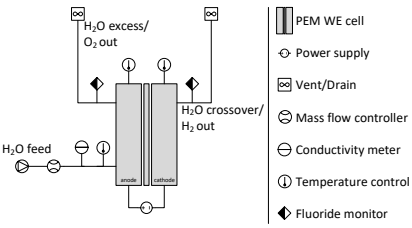

Figure 1: Test set-up for all experiments. The power supply was replaced by a high current potentiostat during characterization

2.2. Procedures

The cell characterization included recording the polarization curve (IV-curve), the anode-side cyclic voltammogram (CV), electrochemical impedance spectroscopy (EIS) measurements at several currents, and collecting an effluent water sample at both anode and cathode for fluoride analysis.

Polarization curves were measured in ascending direction in flexible steps from 0.01 to 2.0 A cm^{-2} to capture the low current range, which is dominated by activation losses, sufficiently well.

This was followed by galvanostatic EIS measurements at 0.1, 0.5, 1.0, 1.5, and 2.0 A cm^{-2}. The frequency range was set to 60 000 Hz - 0.1 Hz, with 10 points per decade and an AC amplitude of 5% of the value of the DC operation point. For this work, the impedance data is used to extract the intercepts with the x-axis in the Nyquist representation at high and low frequency. The high frequency intercept (HFR) represents all ohmic resistances of the cell assembly, whereas the low frequency intercept (LFR) represents the polarization resistance.

During the CV measurements, the cathode side was flushed with hydrogen gas, while the water flow was kept constant at the anode. Measurements with scan rates of 300 and 50 mV s^{-1} were recorded. Furthermore, a sample of effluent water at anode and cathode outlets at 0.3 A cm^{-2} was captured for each point of characterization. As a trade-off between the need for capturing steady state ion concentrations and short collection time to exclude capturing transients, the effluent water was collected for 150 s at the anode and 1 h at the cathode side. The samples were then analyzed in an ion chromatograph (Thermo Scientific DIONEX® ICS 2100) for fluoride content.

Finally, the MEAs were investigated ex-situ under a ZEIS LEO 1530 scanning electron microscope (SEM). All samples were taken from the same spot in the middle of the MEA, put into a resin and polished for examination.

The tests were run at atmospheric pressure with a constant feed water flow rate of 500 mL h^{-1} without recirculation. The feed water was preheated to the operation temperature and the conductivity was monitored throughout the whole test to ensure sufficient quality of 18.2 MΩ · cm. Additionally, heater pads on both sides were installed for a homogeneous temperature distribution within the cell. Each experiment was run for at least 500 h. Table 1 summarizes the investigated operation modes. The parameter of interest besides temperature was the current profile. Therefore, one constant and three dynamic current profiles were tested. The solar profile was constructed from data of a real photovoltaic system over 16 h, where the the mean value was around 1.0 A cm^{-2} and the dwell time 60 s. The periods of the two current cycling profiles, 100 s and 10 s, were extracted by a Fourier transformation of the solar profile. Although no clear dominant frequency was identified, two broad peaks at the highest frequencies were chosen as highly dynamic operation is simulated.

#	operation mode	operation point	temperature	experiment name
1	constant current	2.0 A cm^{-2}	80 °C	*cc*
2	constant voltage	2.0 V	60 °C	*T*60
3	constant voltage	2.0 V	80 °C	*T*80
4	constant voltage	2.0 V	90 °C	*T*90
5	cycling current	0–2.0 A cm^{-2}, 100 s dwell time	80 °C	cyc_{100s}
6	cycling current	0–2.0 A cm^{-2}, 10 s dwell time	80 °C	cyc_{10s}
7	dynamic current	0–2.0 A cm^{-2}, 60 s dwell time, solar profile	80 °C	*solar*

Table 1: Investigated operation modes. Each experiment was carried out on a fresh cell assembly after break-in for at least 500 h

3. Results and discussion

3.1. Break-in phase monitoring

All cells went through the same break-in phase according to the procedure seen in figure 2a. The procedure includes current steps at lower and higher frequencies, and periods of constant current. One cycle lasts around 40 min and is repeated for around 60 h. To get more insight into the involved processes, the break-in phase of experiment *solar* was monitored, including short EIS measurements at the indicated points. The parameters were set to have as little impact on the actual procedure as possible. Furthermore, the anode side CV was recorded before and after break-in.

Break-in may generally be assumed to make more active sites available [12]. This could be achieved by washing impurities within the components that originate from the manufacturing and assembly process. In fact, the recorded anode side CVs before and after break-in indicate an increase in active sites with around 6% increase in charge at 50 mV s^{-1} as seen in figure 2d. When looking at the evolution of potentials and EIS data, a clear impact over time is visible. As seen in figure 2b, the potential at 2.0 A cm^{-2} drops considerably from around 2.07 V after the first cycle to 1.88 V after 21 cycles and a little further down to 1.84 V just before the break-in was terminated after 83 cycles. At

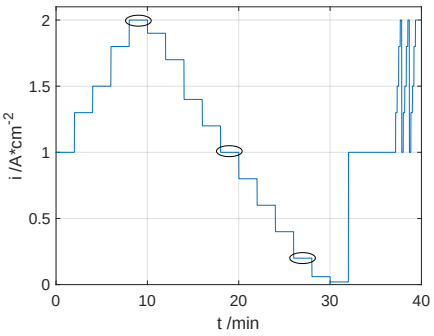

(a) Break-in profile each cell went through prior to the experiment. For experiment *solar*, EIS measurements were taken at the marked points

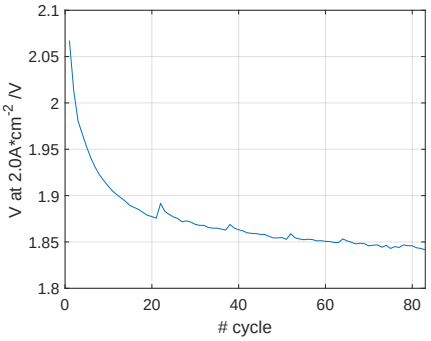

(b) Evolution of the potential at 2.0 A cm^{-2} during break-in for experiment *solar*

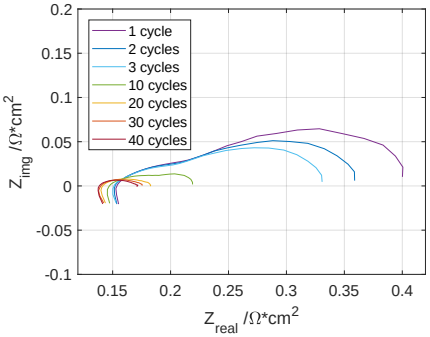

(c) Evolution of the Nyquist diagram at 2.0 A cm^{-2} during break-in for experiment *solar*

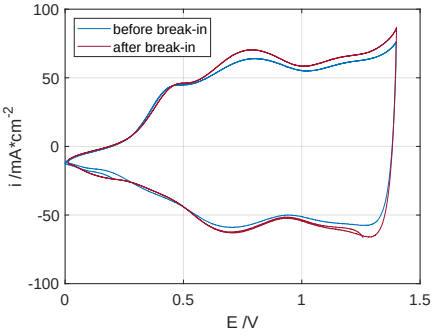

(d) Anode side cyclic voltammogram at 50 mV s^{-1} before and after break-in

Figure 2: Break-in phase monitoring

the same time, both HFR and LFR decrease at different rates as seen in figure 2c. During the first 30 cycles (≈ 20 h), the LFR decreases from 400 to 180 mΩ cm^2, where it stabilizes. Meanwhile, the HFR decreases by 6.7% from 150 to 140 mΩ cm^2. Both values are reduced by another 10 mΩ cm^2 within the remaining 53 cycles (≈ 38 h), before the break-in was terminated.

Break-in can manifest itself as an improvement of contacts through homogenization of the layers, where they adjust to each others specific surface. This could be due to an increase of the number of three-phase boundaries, which leads to a decrease in LFR. Such an adjustment has been observed during long-term operation through SEM images [5]. Furthermore, the performance increase during break-in may be explained by washing out impurities from the manufacturing process. Different compounds of the MEA have reportedly been suspected to be washed out during operation [13]. A deep understanding of the break-in process for PEM WE is missing in the literature, while a decrease in HFR has also been reported for PEM FC [14], where it has been connected to fully humidifying the membrane. However, this process is neglected for PEM WE since it should be faster in the presence of excess liquid water.

3.2. Analysis of fast cycling operation (experiment cyc_{10s}

) Since this work aims at dynamic operation, the focus is given to the analysis of experiment cyc_{10s} (0–2.0 A cm^{-2}, 10 s each, 80 °C). Hereafter, the operation modes are compared among each other.

3.2.1. Cell voltage degradation rates

The IV curves in figure 3 reveal an increase in potential at low currents, while the potential decreases at higher currents (around ≥ 1.2 A cm^{-2}) over time as seen in the two magnified inserts. For a deeper analysis, a way to represent the data is by calculating voltage degradation rates from the evolution of IV curves at different current set points. Figure 4 shows the voltage degradation rate at 0.1, 0.5, 1.0, and 2.0 A cm^{-2} relative to the beginning of life value. That is, the last point represents the rate for the period between 0 h and 506 h, which illustrates the overall impact until the end of the experiment. Since the parameter represents a voltage change, positive values indicate a loss in performance (voltage increase), whereas negative values indicate a gain in performance (voltage decrease).

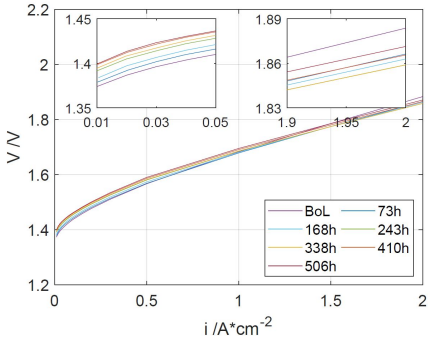

Figure 3: Evolution of polarization curves at all characterization points for experiment cyc_{10s}. The inserts show a magnified view for low (left) and high (right) currents

When looking at the entire duration of the experiment in figure 4, it can be seen that the performance at 2.0 A cm^{-2} after 500 h is better than at the beginning of life. However, when looking at the evolution of the voltage degradation rate at 2.0 A cm^{-2}, a trend is visible. Starting at around −250 µV h^{-1}, it increases up to around 75 µV h^{-1}. This means, the performance at higher current operation initially increases, before a performance decrease can be observed, where the turning point lies at 338 h. This is not the case for low current operation (0.1 and 0.5 A cm^{-2}), which is dominated by activation processes. Since their rates are positive throughout the whole experiment and are relatively constant around 50 µV h^{-1} over time, it may be deduced that the overpotential due to OER and HER degrades at a constant rate. This behavior suggests that the initial increase in performance is of ohmic or mass transport nature, since these processes are most pronounced at high current.

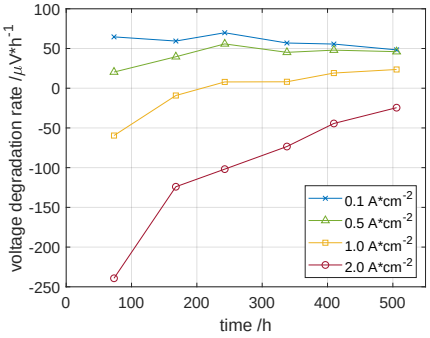

Figure 4: Evolution of voltage degradation rates at different current densities over time for experiment cyc_{10s} relative to the beginning of life (after break-in). Positive values indicate performance decrease, while negative values indicate a performance increase

3.2.2. Membrane degradation

Perfluorinated membranes such as Nafion® are known to potentially experience fluoride loss over time. In this work, Nafion® is used for the membrane as well as a binder within the CL, which means that both components are prone to degradation. The extent of fluoride emission was measured through its concentration within the effluent water as shown in figure 5.

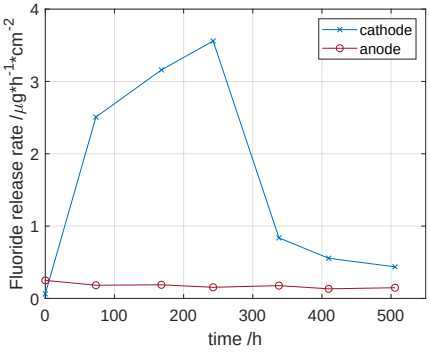

Figure 5: Evolution of fluoride emission rates normalized to area and time at the anode and cathode outlets over time for experiment cyc_{10s}

It can be seen that the fluoride emission at the anode outlet is generally one order of magnitude lower compared to the cathode outlet at the same operation point. The beginning of life is an exception, where the cathode concentration is almost zero and therefore lower than the anode concentration. The anode side concentration is constantly around $0.18\,\mu g\,h^{-1}\,cm^{-2}$, while the cathode side fluoride concentration is not as stable and varies from almost zero to $3.56\,\mu g\,h^{-1}\,cm^{-2}$. The peak is reached at around 250 h. These results suggest that the major ionomer degradation occurs at the cathode side of the cell. This has been observed before in the literature [6] and is true for all operation modes. The following degradation pathway may explain the mechanism: Oxygen produced at the anode crosses the membrane, where it is reduced to hydrogen peroxide in the presence of the cathodic platinum catalyst. Metallic ions from impurities within the PEM WE system, catalyze hydroxyl radical ($HO^{\bullet}$) generation from hydrogen peroxide known as the Fenton reaction. This has been suggested for PEM FC before [10]. The radicals in turn attack the ionomer, leading to detectable fluoride emission [15]. In this case the origin of the fluoride could be the membrane

and the ionomer binder within the CL.

Due to the fluoride loss, the membrane may experience thinning over time [16], which was examined through SEM images in this work. Besides this, an optical image of the different components can be obtained. The samples were compared to a sample of fresh N115 membrane as shown in figure 6a. The image of the MEA after being used in experiment cyc_{10s} is shown in figure 6b, where a thinning effect was observed. The difference in thickness was 17 µm, which corresponds to a thinning rate of 33.7 nm h^{-1}. However, many challenges make an extraction of quantitative data from SEM images difficult. The water uptake highly influences the thickness [17] and was attempted to be comparable by applying the same procedure to all MEAs after the cell disassembly. Since all experiments were carried out at the same cell compression, the impact on thickness due to compression was minimized. Accounting for inhomogeneous thinning over the active area was limited to the given sample, which was approximately 1 cm · 0.5 cm. As all samples were taken from the middle of the MEA to ensure the highest possible comparability.

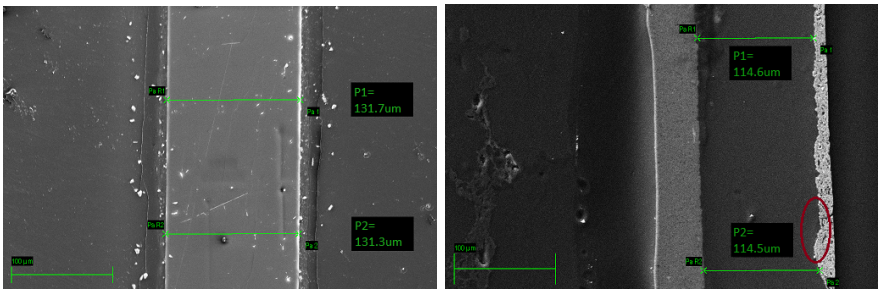

(a) Fresh Nafion® 115 membrane without catalyst layers

(b) MEA including cathode PTL after experiment cyc_{10s}. The cathode is on the left, the anode on the right. The circle indicates an example of adjustments to local variations

Figure 6: SEM images before and after experiment cyc_{10s} to extract qualitative and quantitative data

3.2.3. Catalyst layer degradation

Qualitatively, the SEM images reveal that the cathode catalyst layer is relatively thick with around 20 µm due to the carbon-support, and does not exhibit severe damage. It can also be observed that the CL especially at the anode side and membrane adapted to local variations.

The evolution of the anodic electrode charge as extracted from the CV is shown in figure 7. The charge was normalized by area and calculated from the integral of the forward scan between 0.4 V and 1.2 V divided by the geometric area of 25 cm^2. From the evolution of charge no degradation is visible, which may be explained by the high anode catalyst loading that supposedly benefits CL durability [18]. In fact, the measured charge increased by around 10%, which has been observed in different tests as well [19]. This can be connected to an adjustment of the structure of the catalyst layer to local inhomogeneities in the first period of operation, which has been reported to affect the contact resistance [5] but is here suspected to also have a positive effect on available active sites. It can be concluded that the anode catalyst layer is not responsible for a major voltage increase. A further insight can be obtained from the EIS data.

3.2.4. Evolution of resistances

The LFR represents the polarization resistance and should therefore be equal to the slope of the IV curve at the specific operation point. Figure 8 shows all three values at 2.0 A cm^{-2} over time (left y-axis) together with the difference between LFR and HFR (right y-axis).

The values of LFR and IV slope do correlate quite well, which is seen as a proof of the integrity of the recorded data. Therefore, from now on only the LFR is used to quantify the polarization resistance of the cell. It can be seen

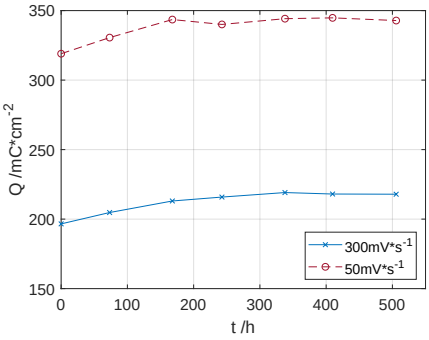

Figure 7: Evolution of anodic electrode charge extracted from CV at 50 mV s^{-1} and 300 mV s^{-1} over time for experiment cyc_{10s}

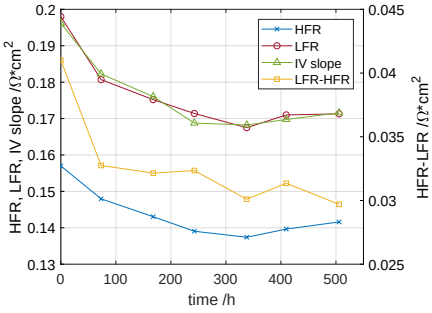

Figure 8: Evolution of resistances over time for experiment cyc_{10s}. HFR, LFR (left axis), and their difference (right axis) were extracted from EIS measurements at 2.0 A cm^{-2}, IV slopes (left axis) from polarization curves.

that the HFR as well as the LFR are decreasing within the first 338 h, before both show a slight increase for the rest of the experiment.

To see if the increase in performance solely stems from the decrease in HFR, the difference between LFR (equivalent to the polarization resistance) and HFR (total ohmic resistance) is calculated. If this was the case, the difference would be constant. However, the values are shown in figure 8 and reveal a decrease in difference over time. This suggests that there is also another component involved in the performance gain, where the major share of around $8\,\mathrm{m\Omega\,cm^2}$ is attributed to the first ~100 h of operation. Afterwards, the value stabilizes and further decrease is negligible with around $2\,\mathrm{m\Omega\,cm^2}$ during a period of 400 h of operation. The initial drop correlates well to the observed increase in charge within the first ~150 h and may be connected to an improved mass transport of oxygen bubbles through the catalyst layer or porous transport layer [20]. This decrease is in fact similar to what was observed for the break-in phase and may therefore be caused by the same phenomena.

Just as the increase in performance at high currents from the IV curve analysis suggested, the decrease in HFR can be connected to a decrease in ohmic resistance due to enhanced membrane conductivity and membrane thinning, and improved contacts among the different components of the cell [21]. The observed decrease in HFR is $15.4\,\mathrm{m\Omega\,cm^2}$ over the whole duration of the test, which would lead to a thinning-induced voltage decrease rate of $-61\,\mu\mathrm{V\,h^{-1}}$ at $2.0\,\mathrm{A\,cm^{-2}}$, where the observed rate lies at $-25\,\mu\mathrm{V\,h^{-1}}$. While the change in ohmic resistance will be discussed further in section 3.3.3, it can already be extracted, that different mechanisms occur simultaneously. The previously identified mechanisms that affect cell potential are membrane thinning [22], structural adjustments of the CL [5], improvement of ionic conductive pathways [7], catalyst degradation/loss [7], and Ti-PTL passivation [5]. Their extent and therefore the dominant phenomenon is not coherent within the stated literature, which leads to the occurrence of both positive and negative voltage degradation rates.

3.3. Comparative analysis of operation modes

The above presented analysis for experiment cyc_{10s} was done for all operation modes and the results are compared and summarized in this section.

3.3.1. Comparison of cell voltage degradation rates

The mean voltage degradation rates over the entire duration of the test for each operation mode are shown in figure 9. The graph reveals that fast cycling and the solar profile are the only modes with a negative value (-25.0 and $-19.0\,\mu\mathrm{V\,h^{-1}}$). According to the results, a temperature increase from 60 °C to 80 °C has a moderate negative impact on the rate from 1.2 to $3.0\,\mu\mathrm{V\,h^{-1}}$, while operating at 90 °C causes a major rise to $183.8\,\mu\mathrm{V\,h^{-1}}$. Slow cycling operation cyc_{100s} at 80 °C is placed in between these values with $17.1\,\mu\mathrm{V\,h^{-1}}$. Experiment *cc* exhibits a much higher voltage degradation than the other experiments at 80 °C. Although constant operation at $2.0\,\mathrm{A\,cm^{-2}}$ has been reported to negatively affect voltage durability compared to other operation modes [5], the here observed high rate is suspected to at least partly stem from the slightly different cell design for that experiment. A thin gold foil was inserted into the cell assembly in an attempt to monitor contact resistances in-situ. Although the impact is maintained low through the design of the experiment, it can not be excluded that the slight modification may have affected the pressure distribution or cell tightness, leading to a higher degradation rate.

Voltage degradation rates on a molar basis have been calculated, where the hydrogen production is considered. Their averaged values for experiments *cc*, cyc_{100s}, cyc_{10s}, and *solar* are 286.1, 36.7, -53.5, and $-40.8\,\mu\mathrm{V/mol_{H_2}}$, respectively. It should be born in mind that the calculation was done on a theoretical basis according to Faraday's law of electrolysis, where potential losses such as gas crossover are neglected. However, these values could be more useful in further cost analyses, in which the operating expense and capital expense could be compared to the revenue. Potential revenue streams besides the obvious monetarization of the produced hydrogen include offering grid services as described in the introduction. Molar-based degradation rates may be more comparable than time-based degradation rates, since the hydrogen production is different according to current magnitude and cycling characteristics. In this context, the required energy per produced unit of hydrogen would also have to be considered, since it is highly affected by temperature and degradation processes.

3.3.2. Comparison of membrane degradation

As discussed in section 3.2.2, the fluoride emission at the cathode is higher. Therefore, figure 10a shows only the values at the cathode outlet over time for all operation modes. From the figure, no clear trend with regard to the time

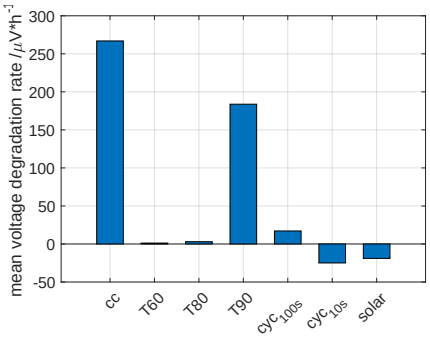

Figure 9: Mean voltage degradation rates at 2.0 A cm^{-2} after each experiment was terminated

can be extracted. While most operation modes exhibit the highest emission rate at the beginning of the test followed by a decline, experiment *cc* is quite steady over the whole course, experiment cyc_{10s} finds its peak after around 250 h, and experiment $T90$ shows an increase all the time.

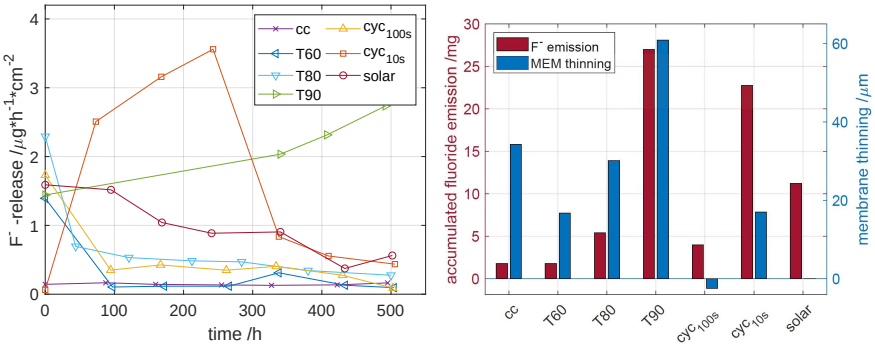

(a) Fluoride emission rates at the cathode outlet over time

(b) Accumulated fluoride emission and membrane thinning after each experiment as extracted from SEM images

Figure 10: Comparison of fluoride emission (all experiments) and membrane thinning (all experiments except *solar*)

The absolute numbers of emitted fluoride mass after each experiment was terminated can be seen in figure 10b, where the values were calculated as the integral of each curve. It can be seen, that an increase in temperature leads to an increase in fluoride emission. The change from 60 °C to 90 °C is accompanied by an increase in fluoride emission by one order of magnitude from 1.8 mg to 27.0 mg. The total fluoride emission at 80 °C is 5.4 mg, suggesting a non-linear relationship with temperature. Cycling at 100 s dwell time, which was also carried out at 80 °C, leads to a similar value of 4.0 mg. However, the two more dynamic experiments cyc_{10s} and *solar* exhibit an elevated emission of 22.8 mg and 11.2 mg, respectively. Since they are also operated at 80 °C, it can be concluded that dynamic operation leads to higher fluoride emission.

As SEM microscopy is destructive and therefore only carried out at the end of each experiment, a membrane thickness tracking over time is not possible. However, figure 10b summarizes the thinning after each experiment measured through SEM except for the *solar*, as it was not terminated at the time of writing. As all other experiments were carried out for 500 ± 5h, those numbers are comparable. The extracted thickness loss for the three temperature-

experiments is coherent with their respective fluoride loss, where the test at 90 °C led to almost 35% decrease. It should be noted, that this experiment utilized a N117 membrane, which is considered the same as N115 in terms of chemical structure except for the thickness. The influence of dynamic operation on the other hand is somewhat contradictory to the fluoride emission. Experiment cyc_{100s} exhibits an increase in thickness, while experiment cyc_{10s} has less decrease than experiment $T80$, which is not what would be expected from the fluoride emission data. The increase in thickness may not be explained physically. A higher water uptake compared to the fresh N115 sample may explain the difference [17], or coincidentally taking the sample from a portion of the membrane, where it was locally thicker from the beginning. However, it is possible that the operation mode shifts the major point of attack from the membrane to the ionomer content in the CL. This may explain a high fluoride emission without evidence of accelerated membrane thinning. To follow on this hypothesis, the impedance data is further analyzed.

3.3.3. Comparison of evolution of resistances

The total ohmic resistance of all cells increases, with experiment cyc_{10s} and *solar* being the exceptions, where a decrease was observed. Figure 11 shows the evolution of the HFR in relative numbers with respect to their respective initial value.

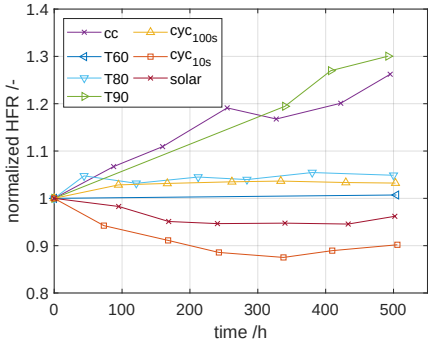

Figure 11: Comparison of HFR relative to the beginning of life for all experiments over time

Experiments $T80$ and cyc_{100s} are similar to each other in their behavior, where both increase slightly by around 4% during the first period and stay constant for the rest of the test. Experiment *cc* on the other hand increased continuously over the whole course of time, reaching around 25% increase after 500 h. This behavior has been observed in the literature [4], where constant operation at 2 A cm^{-2} as well as cycling with a 6-hour period show a similar trend. An increase in HFR has previously been reported and connected to impurities within the membrane and Ti-PTL passivation [8, 5]. It is reported that a thin oxide layer builds up on the Ti-PTL, which increases the ohmic resistance.

Experiments cyc_{10s} and *solar* exhibit an increase in performance over the first approximately 300 h, in both cases mostly associated to a decrease in ohmic resistance, while all other experiments behave the opposite. Experiments cyc_{10s} and *solar* are also the most similar in nature to the applied break-in procedure, which is based on a fast change in potential as described in section 3.1. Since a decrease in ohmic resistance is also observed during the break-in phase, which was performed at similar cycling conditions, it is suspected that similar processes are involved. That includes beneficial structural changes within the layers and removal of impurities. Although it is assumed that these processes are finished after the break-in before the test, they may be prolonged in this specific operation mode.

Meanwhile, low-frequency cycling may not have a positive impact due to the long periods at constant potential. The time between a potential change in experiments cyc_{10s}, *solar*, and cyc_{100s} are 10 s, 60 s, and 100 s, respectively. Therefore, it is possible that the threshold dwell time above which no positive effect is observed anymore lies between 60 s and 100 s. Furthermore, a possible explanation may be that the bubble growth under a constant signal leads to a resistance increase [23, 20]. In this case, the bubbles are suspected to further locally dehydrate the membrane.

When a shift in potential occurs, the bubbles may experience a faster detachment or change in growth behavior, which is beneficial for membrane hydration and therefore durability. It has been reported that low-frequency cycling (0–2.0 A cm^{-2}, 6 h each) led to a decrease in HFR, compared to an increase for constant operation at 2.0 A cm^{-2} [4]. The same experiment with a 10-minute cycle showed a more or less constant HFR after 500 h. However, they did not observe a voltage decrease in any of their operation modes, which were constant current or had more than 100 s dwell time. A stack operated at up to 4.0 A cm^{-2} constant current exhibited a decrease in HFR and potential, and exhibited fluoride emission while no membrane thinning was observed [7]. The authors connected the decrease in HFR to improved ionic conductive pathways, and the increase in overall cell performance over time to the fact that positive phenomena dominate over the negative such as Ti-passivation.

In the following it is attempted to separate the total ohmic change into the components membrane thinning and PTL. The PTL contribution consists of Ti passivation and the suspected positive effect of MEA adjustments to the PTL. They may also have an impact on the non-ohmic overpotential. Ti passivation has in fact been reported in connection with the HFR [19, 4] as well as in connection with a high frequency arc in the Nyquist plot [7]. This work attempts to identify the purely ohmic contribution and therefore investigates the effect on HFR.

On the other hand, a thinning of the membrane over time results in a decrease of its overpotential due to the linear relationship according to Ohm's law. The theoretical decrease in cell voltage due to that is calculated and subtracted from the total voltage degradation rate due to ohmic phenomena measured from the HFR at 2.0 A cm^{-2}. A constant membrane conductivity of 15 S m^{-1}, which is seen as the upper limit, is assumed for this analysis [17, 24]. The result is the voltage degradation rate connected to all other ohmic phenomena than membrane thinning and shown in figure 12. For comparison, the total cell voltage degradation rate as in figure 9 is repeated as well as the voltage degradation rate extracted from the change in HFR.

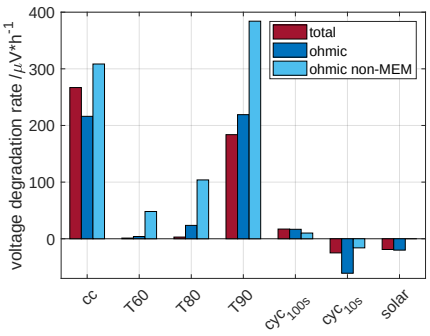

Figure 12: Separation of the impact of processes on the voltage degradation rates at 2.0 A cm^{-2}. The total is extracted from IV curves, ohmic from the change in HFR, and ohmic non-membrane (MEM) is the membrane-thinning-corrected value extracted from the HFR

It can be seen that the membrane-thinning-corrected value is highly affected by the temperature, as it increases from 104 µV h^{-1} at 80 °C to 384 µV h^{-1} at 90 °C. A reasonable explanation is the previously suggested passivation of the Ti-PTL, which is enhanced at elevated temperatures [25] and has been observed in the literature [5, 6]. The value is reduced to 10 µV h^{-1} for cyc_{100s}, where the lower extent of titanium passivation may be explained by a lower residual time of oxygen within the electrode for cycling operation, which was earlier suggested as a reason for lower local membrane dehydration. If the non-membrane thinning related contribution to the change in HFR is higher than what the HFR change induces, it means that the negative effect of PTL passivation is dominant over the positive effect of membrane thinning. The negative value for cyc_{10s} suggests that a positive ohmic phenomenon is dominant over PTL passivation. This could be due to the discussed improved contact between MEA and PTL.

Experiments cyc_{10s} and *solar* show a decrease in HFR together with a high fluoride emission rate. However, membrane thinning was not found to be more severe compared to the other operation modes, which points to the cathode CL as a source of the fluoride. This fluoride loss actually seems to improve the structure and therefore performance of the CL as the cell voltage decreases over time. The changing point is after around 300 h, where the

HFR starts to slowly increase, may it be due to dominant PTL passivation or another process such as irreversible cation contamination.

4. Conclusion

An analysis of degradation phenomena in PEM WE with a focus on the impact of operation modes was presented. Therefore, seven MEAs with the same specifications were run for 500 h each at constant, cycling, and dynamic operation, where for constant operation the effect of temperature was also investigated. It was found that the CL only played a minor role on degradation, while a change in total ohmic resistance dominated the voltage change. Subsequently, the respective shares of membrane and porous transport layer related phenomena were quantified.

It was found that Ti passivation is the major cause of voltage degradation at constant operation, dominating the voltage decrease through membrane thinning. Operation at 90 °C is favorable in terms of efficiency, but highly increases both Ti passivation and membrane thinning over time. Therefore, higher temperature can limit the lifetime considerably due to increased gas crossover for a thinner membrane, while the passivation may revoke the gain in efficiency over time without an appropriate mitigation strategy.

On the other hand, fast cycling operation and simulating a direct coupling of the cell to a solar profile increased the overall performance over the investigated time frame due to a decrease in ohmic resistance. It was furthermore found that fluoride emission is enhanced with fast potential switches, while no significant impact on membrane thickness was observed. Therefore, the fluoride is suspected to originate from the cathode catalyst layer.

Acknowledgement

The authors would like to acknowledge the support by Innovation Fund Denmark through the e-STORE project, Grant 4106-00025B.

References

[1] A. S. Arico, S. Siracusano, N. Briguglio, V. Baglio, A. Di Blasi, V. Antonucci, Polymer electrolyte membrane water electrolysis: Status of technologies and potential applications in combination with renewable power sources, Journal of Applied Electrochemistry 43 (2) (2013) 107–118. doi:10.1007/s10800-012-0490-5.

[2] B. Bensmann, R. Hanke-Rauschenbach, G. Müller-Syring, M. Henel, K. Sundmacher, Optimal configuration and pressure levels of electrolyzer plants in context of power-to-gas applications, Applied Energy 167 (2016) 107124. doi:10.1016/j.apenergy.2016.01.038.
URL http://dx.doi.org/10.1016/j.apenergy.2016.01.038

[3] G. A. Olah, A. Goeppert, G. S. Prakash, Beyond Oil and Gas: The Methanol Economy, Wiley-VCH, 2009.

[4] C. Rakousky, U. Reimer, K. Wippermann, S. Kuhri, M. Carmo, W. Lueke, D. Stolten, Polymer electrolyte membrane water electrolysis: Restraining degradation in the presence of fluctuating power, Journal of Power Sources 342 (2017) 38–47. doi:10.1016/j.jpowsour.2016.11.118.
URL http://dx.doi.org/10.1016/j.jpowsour.2016.11.118

[5] C. Rakousky, U. Reimer, K. Wippermann, M. Carmo, W. Lueke, D. Stolten, An analysis of degradation phenomena in polymer electrolyte membrane water electrolysis, Journal of Power Sources 326 (2016) 120–128. doi:http://dx.doi.org/10.1016/j.jpowsour.2016.06.082.

[6] F. Fouda-Onana, M. Chandesris, V. Médeau, S. Chelghoum, D. Thoby, N. Guillet, Investigation on the degradation of MEAs for PEM water electrolysers part I: Effects of testing conditions on MEA performances and membrane properties, International Journal of Hydrogen Energy 41 (2016) 16627–16636. doi:10.1016/j.ijhydene.2016.07.125.

[7] P. Lettenmeier, R. Wang, R. Abouatallah, S. Helmly, T. Morawietz, R. Hiesgen, S. Kolb, F. Burggraf, J. Kallo, A. S. Gago, K. A. Friedrich, Durable Membrane Electrode Assemblies for Proton Exchange Membrane Electrolyzer Systems Operating at High Current Densities, Electrochimica Acta 210 (2016) 502–511. doi:10.1016/j.electacta.2016.04.164.
URL http://dx.doi.org/10.1016/j.electacta.2016.04.164

[8] S. Sun, Z. Shao, H. Yu, G. Li, B. Yi, Investigations on degradation of the long-term proton exchange membrane water electrolysis stack, Journal of Power Sources 267 (2014) 515–520. doi:10.1016/j.jpowsour.2014.05.117.
URL http://dx.doi.org/10.1016/j.jpowsour.2014.05.117

[9] M. Inaba, T. Kinumoto, M. Kiriake, R. Umebayashi, A. Tasaka, Z. Ogumi, Gas crossover and membrane degradation in polymer electrolyte fuel cells, Electrochimica Acta 51 (26) (2006) 5746–5753. doi:10.1016/j.electacta.2006.03.008.

[10] A. B. LaConti, H. Liu, C. Mittelsteadt, R. C. M. Giner, POLYMER ELECTROLYTE MEMBRANE DEGRADATION MECHANISMS IN FUEL CELLS FINDINGS OVER THE PAST 30 YEARS AND COMPARISON WITH ELECTROLYZERS, ECS Transactions 1 (8) (2006) 199–219.

[11] FCH-JU, ANNUAL WORK PLAN and BUDGET, Tech. rep., FCH-JU (2017).

[12] F. Hasché, Activity , stability , and degradation mechanisms of platinum and platinum alloy nanoparticle PEM fuel cell electrocatalysts, Ph.D. thesis, TU Berlin (2012).

[13] M. Langemann, D. L. Fritz, M. Müller, D. Stolten, Validation and characterization of suitable materials for bipolar plates in PEM water electrolysis, International Journal of Hydrogen Energy 40 (35) (2015) 11385–11391. doi:10.1016/j.ijhydene.2015.04.155.
[14] V. B. Silva, A. Rouboa, Hydrogen-fed PEMFC: Overvoltage analysis during an activation procedure, Journal of Electroanalytical Chemistry 671 (2012) 58–66. doi:10.1016/j.jelechem.2012.02.013.
URL http://dx.doi.org/10.1016/j.jelechem.2012.02.013
[15] M. Chandesris, V. Médeau, N. Guillet, S. Chelghoum, D. Thoby, F. Fouda-Onana, Membrane degradation in PEM water electrolyzer: Numerical modeling and experimental evidence of the influence of temperature and current density, International Journal of Hydrogen Energy 40 (3) (2015) 1353–1366. doi:10.1016/j.ijhydene.2014.11.111.
[16] F. N. F. Büchi, M. Inaba, T. J. T. T. J. Schmidt, Polymer Electrolyte Fuel Cell Durability, Springer, 2009.
[17] H. Ito, T. Maeda, A. Nakano, H. Takenaka, Properties of Nafion membranes under PEM water electrolysis conditions, International Journal of Hydrogen Energy 36 (17) (2011) 10527–10540. doi:10.1016/j.ijhydene.2011.05.127.
URL http://dx.doi.org/10.1016/j.ijhydene.2011.05.127
[18] S. Cherevko, Stability and dissolution of electrocatalysts : Building the bridge between model and real world systems, Current Opinion in Electrochemistry (2018) 1–8doi:10.1016/j.coelec.2018.03.034.
URL https://doi.org/10.1016/j.coelec.2018.03.034
[19] S. Siracusano, N. Hodnik, P. Jovanovic, F. Ruiz-Zepeda, M. Šala, V. Baglio, A. S. Aricò, New insights into the stability of a high performance nanostructured catalyst for sustainable water electrolysis, Nano Energy 40 (September) (2017) 618–632. doi:10.1016/j.nanoen.2017.09.014.
[20] C. Lee, R. Banerjee, F. Arbabi, J. Hinebaugh, A. Bazylak, Porous Transport Layer Related Mass Transport Losses in Polymer Electrolyte Membrane Electrolysis - A Review, Proceedings of the 14th International Conference on Nanochannels, Microchannels, and Minichannels.
[21] S. M. R. Niya, R. K. Phillips, M. Hoorfar, Process modeling of the impedance characteristics of proton exchange membrane fuel cells, Electrochimica Acta 191 (May) (2016) 1–117. doi:10.1016/j.electacta.2016.01.128.
URL http://dx.doi.org/10.1016/j.electacta.2016.01.128
[22] S. Siracusano, N. Van Dijk, R. Backhouse, L. Merlo, V. Baglio, A. Arico, Degradation issues of PEM electrolysis MEAs, Renewable Energy 123 (2018) 52–57. doi:10.1016/j.renene.2018.02.024.
URL http://linkinghub.elsevier.com/retrieve/pii/S0960148118301678
[23] D. Kiuchi, H. Matsushima, Y. Fukunaka, K. Kuribayashi, Ohmic Resistance Measurement of Bubble Froth Layer in Water Electrolysis under Microgravity, Journal of The Electrochemical Society 153 (8) (2006) E138. doi:10.1149/1.2207008.
URL http://jes.ecsdl.org/cgi/doi/10.1149/1.2207008
[24] A. Kusoglu, B. L. Kienitz, A. Z. Weber, Understanding the Effects of Compression and Constraints on Water Uptake of Fuel-Cell Membranes, Journal ofThe Electrochemical Society 158 (12) (2011) 1504–1514. doi:10.1149/2.097112jes.
[25] G. Lu, S. L. Bernasek, J. Schwartz, Oxidation of a polycrystalline titanium surface by oxygen and water, Surface Science 458 (1) (2000) 80–90. doi:10.1016/S0039-6028(00)00420-9.

Paper D

Impact of Iron and Hydrogen Peroxide on Membrane Degradation for PEM Water Electrolysis: Computational and Experimental Investigation on Fluoride Emission

Steffen Henrik Frensch, Guillaume Serre, Frédéric Fouda-Onana, Henriette Casper Jensen, Morten Lykkegaard Christensen, Samuel Simon Araya, Søren Knudsen Kær

The paper has been submitted to the
Journal of Power Sources.

submitted to an Elsevier Ltd. journal

Impact of Iron and Hydrogen Peroxide on Membrane Degradation for Polymer Electrolyte Membrane Water Electrolysis: Computational and Experimental Investigation on Fluoride Emission

Steffen Henrik Frensch[a,*], Guillaume Serre[b], Frédéric Fouda-Onana[b], Henriette Casper Jensen[c], Morten Lykkegaard Christensen[c], Samuel Simon Araya[a], Søren Knudsen Kær[a]

[a] *Aalborg University, Department of Energy Technology, Pontoppidanstræde 111, 9220 Aalborg Øst, Denmark*
[b] *CEA, LITEN, DEHT, F-38054, Grenoble, France*
[c] *Aalborg University, Department of Chemistry and Bioscience, Fredrik Bajers Vej 7, 9220 Aalborg Øst, Denmark*

Abstract

Polymer electrolyte membrane (PEM) degradation in electrolysis mode is simulated through a Fenton model that includes all major involved electrochemical reactions. Supportive experimental investigations on the effect of hydrogen peroxide and iron impurities are carried out in an ex-situ set-up, where the results are utilized to fit model parameters. The experiments reveal a high dependence of fluoride emission on iron concentration, which catalyzes the reaction, and identifies hydrogen peroxide as a necessary precursor for destructive hydroxyl radical formation. Simulations of in-situ operation reveal

[*] Corresponding author, (+45) 50 25 10 31
Email addresses: stf@et.aau.dk (Steffen Henrik Frensch), guillaume.serre@cea.fr (Guillaume Serre), frederic.fouda-onana@cea.fr (Frédéric Fouda-Onana), hcj@bio.aau.dk (Henriette Casper Jensen), mlc@bio.aau.dk (Morten Lykkegaard Christensen), ssa@et.aau.dk (Samuel Simon Araya), skk@et.aau.dk (Søren Knudsen Kær)

that elevated current is favorable in terms of lower fluoride emission, as the radicals are depleted by side reactions. Temperatures above 80 °C significantly accelerate membrane thinning, where the step from 80 °C to 90 °C more than doubles thinning after 500 h.

Keywords: PEM water electrolysis aging, Membrane degradation modelling, Fenton reaction model, Hydrogen peroxide, Fluoride emission rate

---

Nomenclature

1. Introduction

Membrane degradation for polymer electrolyte membrane water electrolysis (PEM WE) is crucial, since it does not only have an impact on cell performance, but also directly affects operation safety. Membrane thinning as a result of degradation increases gas crossover, possibly leading to explosive mixtures [1, 2]. The membrane is therefore considered as one of the lifetime limiting components of a PEM WE system [2]. Membrane degradation in PEM WE is not yet fully understood, but the here described mechanism has been suggested in the literature [2]. Besides protons (H^+) and water (H_2O), also oxygen (O_2) is transported through the membrane from the anode to the cathode side. In the presence of a platinum catalyst, as it is the case in a state of the art PEM WE cathode (CL_c), oxygen and protons react to form hydrogen peroxide (H_2O_2) according to equation I [3]:

$$O_2 + 2\,H^+ + 2\,e^- \longrightarrow H_2O_2 \tag{I}$$

In turn, the produced H_2O_2 forms highly reactive hydroxyl radicals ($HO^\bullet$). This reaction is strongly catalyzed by ferrous iron ions (Fe^{2+}) and under that

symbol	**name**	**value/ unit**
A_i	frequency factor of rxn i	-
αH_2O_2	transfer coefficient of rxn 1	0.5
c_s	concentration of species s	$\mathrm{mol\,m^{-3}}$
δ_{mem}	membrane thickness	m
$E_{act,i}$	activation energy of rxn i	$\mathrm{J\,mol^{-1}}$
$\eta_{H_2O_2}$	equilibrium potential of rxn 1	0.695 V
EW	equivalent weight PFSA	$1100\,\mathrm{g\,mol^{-1}}$
F	Faraday constant	$96485\,\mathrm{C\,mol^{-1}}$
$f_{F,loss}$	model fit factor	20.8
FER	fluoride emission rate	$\mu\mathrm{g/m^2/h}$
k_i	reaction rate constant of rxn i	$\mathrm{m^3\,mol^{-1}\,s^{-1}}$ (rxn 3 – 13)
$\nu_{F,PFSA}$	partial specific volume PFSA	$\mathrm{m^3\,g^{-1}}$
ω_F	mass fraction of fluorine in PFSA	0.69
R	gas constant	$8.314\,\mathrm{J\,mol^{-1}\,K^{-1}}$
r_i	reaction rate of rxn i	$\mathrm{mol\,m^{-3}\,s^{-1}}$
ρ_{PFSA}	density dry PFSA	$1980\,\mathrm{kg\,m^{-3}}$
T	temperature	K
T^0	reference temperature	298.15 K
ν_s	stoichiometric factor of species s	-
V_s	volumetric flow rate of species s	$\mathrm{mol\,m^{-3}\,s^{-1}}$

Table 1: Nomenclature

condition well known as the Fenton reaction as seen in equation II:

$$H_2O_2 + Fe^{2+} \longrightarrow Fe^{3+} + HO^{\bullet} + HO^{-} \quad \text{(II)}$$

The exact mechanisms of the Fenton reaction are not yet fully understood [4], but assumed to play a role in PEM WE degradation. It is commonly agreed that metallic impurities such as iron ions accelerate membrane attack in the presence of H_2O_2. These iron impurities may stem from the balance of plant [2], however, this claim has yet to be proven and further developed. The assumption is that all components made of stainless steel such as the the cell housing and the piping system release iron ions over time [5]. The behavior of iron within the system is not well documented, i.e. the ions may cross the membrane, stay within it, or be flushed out at one of the outlets. An accumulation of ions would increase the concentration over time, which may affect the reaction kinetics. The radicals formed through the Fenton reaction may attack the membrane structure, which leads to a release of fluoride in the case of Nafion®.

Although the operating conditions and therefore the reaction environment is different in PEM WE, the underlying mechanisms may be deduced from PEM fuel cell (FC) research, since the state of the art membrane material is usually the same. A good PEM FC review can be found in the literature [6] that summarizes the proposal that hydrogen peroxide (H_2O_2) decomposition is highly involved in chemical degradation. This claim is challenged by an experimental investigation, which finds H_2O_2 to be responsible for only a small fraction of membrane degradation [7]. With or without involvement of H_2O_2, radicals may attack the ionomer binder within the catalyst layer, at the inter-

face between catalyst layer and membrane, or diffuse from the cathode electrode back into the membrane, where it can also attack the ionomer.

A modelling framework for chemical degradation based on radical attack as described above was proposed in [8], who resolved the membrane and assumed the above mentioned involvement of H_2O_2. Similarily, a comprehensive simulation with a focus on radical formation through H_2O_2 compares perfluoroalkyl sulfonic acid (PFSA) membranes to poly(styrenesulfonic acid) (PSSA) membranes and includes an ex-situ Fenton reaction simulation [9]. The authors find very different attack mechanisms for both membrane types and reveal a higher FER for the ex-situ test by 2-3 orders of magnitude. The points of attack and the evolution of their availability in PFSA membranes was simulated by [10], who found a more severe impact of iron ion concentration compared to H_2O_2 on radical formation. Finally, semi-empirical degradation data was incorporated into a model to simulate membrane thinning in [11].

As for PEM WE, a model approach similar to the ones found for PEM FC is described in the literature [12]. The work is based on modelling and experimental data to simulate membrane attack accompanied by membrane thinning. However, the degradation behavior of both are not fully identical [13] and compared to PEM FC, studies dedicated to PEM WE remain scarce. Experimentally, the effect of current density on fluoride emission rate (FER) was investigated in [14], who found a peak between 0.2 and 0.4 $\mathrm{A\,m^{-2}}$. The authors furthermore reported that a majority of membrane degradation can be observed on the cathode side [14], which supports the presented degradation mechanism.

This work aims at developing the presented modelling approach further

for PEM WE applications and operation strategies. Furthermore, the simulations are supported by experimental data that investigates the effect of hydrogen peroxide and iron ions on fluoride release.

2. Experimental Methodology

Eleven polypropylene flasks were filled with 100 mL ultra-pure water for the ex-situ experiment. A specific initial concentration of Fe^{2+} and H_2O_2 according to table 2 was established based on a literature review of previous tests [15, 9, 7]. The iron concentration was set through iron (II) sulfate heptahydrate ($FeSO_4 \cdot 7H_2O$, Merck KGaA) and the hydrogen peroxide concentration through 33%-H_2O_2 solution (VWR Chemicals). 25 cm^2 Nafion® 115 cut into five pieces was immersed and each experiment lasted for 72 h at 80 °C inside an oven. The fluoride content was monitored frequently with an ion selective electrode (ISE, Hach Company ISE301F combined electrode).

3. Model Development

The degradation processes are assumed to be as described above and depicted in figure 1.

The model approach is carried out in Matlab/Simulink® and consists of a 0-dimensional membrane degradation model, which is implemented into a simple performance model. Membrane degradation is among the most crucial mechanisms for PEM WE and can be considered a lifetime-limiting factor [2]. Therefore, capturing the membrane degradation over time through chemical attack is simulated as described above. The Fenton model calculates fluoride emission through concentration of species such as H_2O_2, and

EXP #	[Fe^{2+}] /ppm	[H_2O_2] /wt%
1	0	0
2	1	0
3	1	0.003
4	1	0.03
5	1	0.3
6	1	3
7	1	30
8	0	3
9	0.1	3
10	10	3
11	20	3

Table 2: Experimental matrix for the ex-situ Fenton test. All concentrations refer to their initial value. The highlighted condition is the baseline test

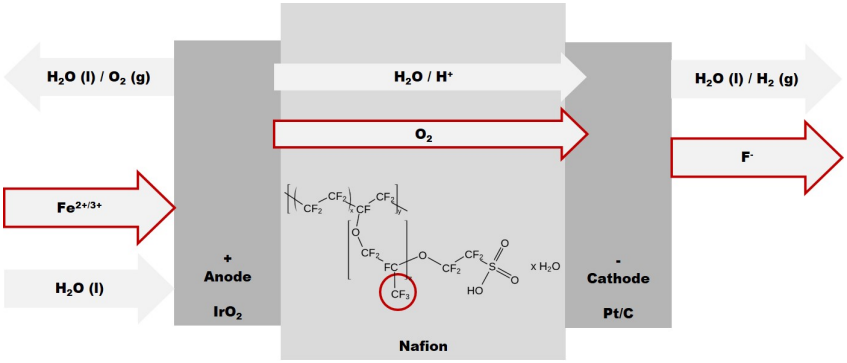

Figure 1: Model scheme for the proposed degradation mechanism

the involved radicals. In its core, the description of the involved electrochemical reaction system is based on [12]. In this work, a set of 14 electrochemical reactions was modelled as one reaction system. An overview over the considered reactions is given in table 3.

The main assumptions are:

- all 14 reactions occur in the same space (CL_c)
- oxygen transported to the cathode is entirely and exclusively reduced to hydrogen peroxide (reaction 1)
- reactions 2-13 follow Arrhenius behavior
- the total fluoride emission (reaction 14) as a macroscopic reaction behaves like an elementary reaction (i.e. also follows Arrhenius behavior)

3.1. Reaction System and Rate Constants

In a coarse-grained approach, the rate constants at 25 °C and the activation energies for reactions 2 to 13 (except for reactions 7, where data for only one temperature was found) were fitted to the Arrhenius equation as in equation III:

$$k = A \cdot exp(-\frac{E_{act}}{R \cdot T}) \tag{III}$$

where k is the rate constant, A the frequency factor in s^{-1} (also known as the pre-exponential factor), E_{act} the activation energy in $J\,mol^{-1}$, R the gas constant in $J\,mol^{-1}\,K^{-1}$, and T the temperature in K. The rate constant for each reaction was then implemented as a function of temperature. Reaction 1 is implemented as described in section 3.2, while reaction 14 is further addressed

in section 3.3. An acidic environment is assumed as the reactions take place close to the highly acidic membrane. The concentrations of species are calculated as in equation IV:

$$\frac{dc_s}{dt} = \sum_{rxn=i} (\upsilon_{s,i} \cdot r_i) + V_{s,in} - V_{s,out} \tag{IV}$$

where υ_s is the stoichiometric factor of species s in reaction i, r_i the reaction rate of reaction i in $\mathrm{mol\,m^{-3}\,s^{-1}}$, and $V_{s,in}$ and $V_{s,out}$ the volumetric flow rate of species s in and out of the modelled volume in $\mathrm{mol\,m^{-3}\,s^{-1}}$, respectively. The stoichiometric factor is negative for reactants and positive for products by convention. It is furthermore assumed to be zero if the species does not participate in the reaction.

3.2. Hydrogen Peroxide Formation

Hydrogen peroxide is the precursor of the here considered reaction system, without which no membrane attack would be observed. As described above, the source of H_2O_2 is oxygen that crossed the membrane and is reduced on the Pt catalyst as shown in reaction 1 in table 3. This pathway has been shown to be dominant in a PEM WE cathode environment, while water formation can be neglected [3]. The reaction kinetics are modelled as in equation V [16]:

$$r_1 = k_1 \cdot c_{O_2} \cdot c_{H^+}^2 \tag{V}$$

where c_{O_2} and c_{H^+} are the oxygen and proton concentrations, respectively, and the rate constant k_1 is given as in equation VI [16]:

$$k_1 = k_1^0 \cdot exp(\frac{-E_{act,1}}{R \cdot T}) \cdot exp(\frac{-\alpha_{H_2O_2} \cdot F \cdot \eta_{H_2O_2}}{R \cdot T^0}) \tag{VI}$$

RXN #	Reaction		E_{act} /kJ mol^{-1}	A /s^{-1}
1	$O_2 + 2H^+$	$\longrightarrow H_2O_2$	42.45* [12]	-*
2	H_2O_2	$\longrightarrow 2HO^\bullet$	200	$1.09 \cdot 10^{13}$
3	$H_2O_2 + Fe^{2+}$	$\longrightarrow Fe^{3+} + HO^\bullet + HO^-$	35.4	$1.03 \cdot 10^{08}$
4	$H_2O_2 + Fe^{3+}$	$\longrightarrow Fe^{2+} + HOO^\bullet + H^+$	126	$8.31 \cdot 10^{18}$
5	$HO^\bullet + Fe^{2+}$	$\longrightarrow HO^- + Fe^{3+}$	9	$8.68 \cdot 10^{09}$
6	$HO^\bullet + H_2O_2$	$\longrightarrow HOO^\bullet + H_2O$	14	$7.66 \cdot 10^{09}$
7	$HO^\bullet + O_2$	$\longrightarrow HOO^\bullet + H_2O$	-*	-*
8	$HOO^\bullet + Fe^{3+}$	$\longrightarrow Fe^{2+} + O_2 + H^+$	33	$1.21 \cdot 10^{10}$
9	$HOO^\bullet + Fe^{2+} + H^+$	$\longrightarrow Fe^{3+} + H_2O_2$	42	$2.74 \cdot 10^{13}$
10	$HOO^\bullet + H_2O_2$	$\longrightarrow HO^\bullet + H_2O + O_2$	30	$5.41 \cdot 10^{05}$
11	$2\,HOO^\bullet$	$\longrightarrow H_2O_2 + O_2$	20.6	$3.5 \cdot 10^{09}$
12	$HO^\bullet + HO^\bullet$	$\longrightarrow H_2O_2$	7.9	$1.31 \cdot 10^{11}$
13	$HOO^\bullet + HO^\bullet$	$\longrightarrow H_2O + O_2$	14.2	$2.09 \cdot 10^{12}$
14	$HO^\bullet + R_f - CF_2 - COOH$	$\longrightarrow$ products	6.5*	$1.35 \cdot 10^{07}$*

Table 3: Simulated reaction system based on [12]. If not otherwise annotated, the frequency factors were calculated from data for activation energies in [10]. *: For the implementation of reactions 1, 7, and 14, see the respective sections in the text

where R, F, and T have their generic meaning, $E_{act,1}$ is the activation energy for reaction 1, and $\alpha_{H_2O_2}$ and η_{H2O2} are the transfer coefficient and equilibrium potential, respectively. k_1^0 is $706.8 \cdot 10^{-14} m^7 \cdot mol^{-2} \cdot s^{-1}$ [16, 12].

While the oxygen concentration is dictated by the dynamics of the reaction system, the proton concentration is dependent on the ionomer humidification and implemented as in equation VII [16]:

$$c_{H+} = \frac{\rho_{PFSA}(\lambda)}{EW} \tag{VII}$$

where $\rho_{PFSA}(\lambda)$ and EW are the humidity-dependent density and the equivalent weight of the ionomer, respectively.

3.3. Membrane Attack Mechanism

The attack mechanism of a polymer such as Nafion® through radicals is widely discussed in the literature [8, 17, 9, 10]. Although the vast majority of publications are attributed to PEM FC, it is assumed that the mechanism itself can be adopted to PEM WE. In this work it is proposed that the radicals formed as described by reactions 2 to 13 attack the ionomer structure at their weak carboxylic acid end-groups (−COOH) [8]. Furthermore, the linkage between backbone and side chains is suspected to be an important point of attack [18, 19].

The attack reaction 14 shown in table 3 is of second order and affected by the concentrations of hydroxyl radicals ($HO^{\bullet}$) and reactive end-groups of the polymer (−COOH). While the $HO^{\bullet}$ concentration is calculated within the reaction system, the concentration of −COOH end-groups is subject of discussion. In this work, a constant value of 200 mM is chosen. This lies within

the values found in the literature, where a constant concentration of 1.17M, representing 5% of the total -CF_2- count in the polymer main chain, can be found [9]. The authors interpret this value as an upper limit, while bringing to the attention that a value of around 2 mM to 20 mM would have to be assumed according to [19], with a potential increase over time as described in [18]. A sensitivity analysis of the parameter is carried out below as shown in figure 7. The reaction rate constant k_{14} was not found for any other temperature than room temperature in the literature. Therefore, it is attempted to fit experimental data from the ex-situ experiments to the Arrhenius equation as described later.

3.4. Quantification of Membrane Degradation Through Fluoride Emission

To quantify membrane thinning through fluoride emission, a relationship between fluoride content and membrane volume has to be established. The partial specific volume of the ionomer per unit fluorine can be expressed as in equation VIII [11]:

$$v_{F,PFSA} = \frac{1}{\omega_F \cdot \rho_{PFSA}} \tag{VIII}$$

where ω_F is the mass fraction of fluorine within the ionomer, and ρ_{PFSA} is its density. The thinning rate is then expressed as in equation IX [11]:

$$\frac{d\delta_{mem}}{dt} = v_{F,PFSA} \cdot FER \cdot f_{F,loss} \tag{IX}$$

where $v_{F,PFSA}$ is the above described partial specific ionomer volume, FER the fluoride emission rate as introduced, and $f_{F,loss}$ a factor that accounts for not

captured fluoride ions and incompletely decomposed fluorine. It is implemented relative to each captured fluoride ion and therefore technically has the unit gg^{-1}, which means it is dimensionless. The extent of total fluorine emission is not widely reported, but FC research indicates that it might be a considerable share [20]. Therefore, membrane thinning may be underestimated in this approach. On the other hand, all fluoride emission is accounted for membrane thinning, while the ionomer binder in the catalyst layers may also contribute to the total fluoride emission. It is experimentally impractical to differentiate between the origin of fluoride, which may lead to an overestimation of membrane thinning.

4. Results and Discussion

4.1. Ex-situ Fluoride Emission

The fluoride concentration for each experiment over time is shown in figure 2. Experiments with varying initial H_2O_2 concentration are shown in solid lines and varying initial Fe^{2+} concentrations in dashed lines together with the baseline and the pure water test in dash-dot lines.

As expected, the test with neither H_2O_2 nor Fe^{2+} initially (#1) only shows a negligible fluoride release, which might be a consequence of hygrothermal aging [21]. The experiment with no H_2O_2 and 1 ppm Fe^{2+} (#2) also exhibits almost no fluoride emission, while the presence of 3wt% H_2O_2 but no Fe^{2+} (#8) lead to a considerable fluoride concentration especially towards the end of the experiment of around 1 ppm. This observation supports the above presented assumption that H_2O_2 is as a obligatory precursor for the whole reaction system, while Fe^{2+} acts as a catalyst.

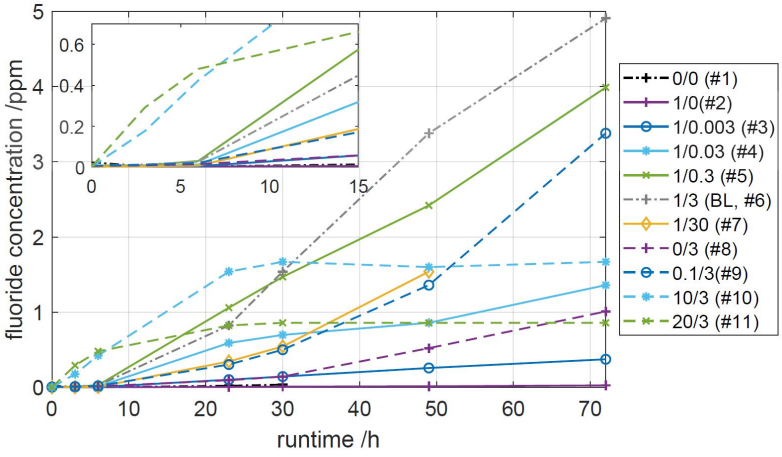

Figure 2: Fluoride concentration over time for all experiments. The legend refers to the initial concentrations as $[Fe^{2+}]/[H_2O_2]$, where BL = baseline test

Before analyzing the effect of the initial species concentration in more detail, two different trends can be observed for the reaction kinetics of fluoride emission: Firstly, a steep increase in the first hours, followed by a constant concentration after around 23 h, and secondly, a rate that starts slowly and accelerates over time. The two experiments with high initial Fe^{2+} concentration (#10 and #11) follow the first trend, while all others tend to follow the second. The second category may exhibit an exponential behavior, where experiments with very low initial H_2O_2 concentration (#1, #2, and #3) arguably follow a more linear trend in the investigated time-frame. A longer period of time would have to be investigated in order to conclude on the kinetic trend. For all tests except the ones with high initial Fe^{2+} concentration, the fluoride concentration is below or just around the detection limit of $5 \cdot 10^{-7}$M (= 0.0095 ppm)

within the first 3 to 6 hours of test as shown in the magnification in figure 2.

The flattening of the curves with high initial Fe^{2+} concentration may be due to H_2O_2 exhaustion. With Fe^{2+} as a strong catalyst, the needed H_2O_2 to run the reaction may be used up very fast and therefore represent the limiting factor in these experiments. Consequently, the final fluoride concentration after the test was terminated may be significantly higher if more H_2O_2 was available, either as an initial concentration or as a steady influx. It can in fact be observed, that the higher initial Fe^{2+} concentration of 20 ppm leads to higher fluoride emission than 10 ppm as measured after 3 h as shown in the magnification in figure 2. Possibly due to the same limiting effect, 20 ppm Fe^{2+} (#11) produced less fluoride emission than 10 ppm Fe^{2+} (#10) at the same H_2O_2 concentration after 6 hours. Therefore, a peak appears at 10 ppm after 23 h when plotting the fluoride concentration over initial Fe^{2+} concentration as seen in figure 3a, which shifts to 1 ppm after 49 h.

When looking at the experiment without any initial Fe^{2+} (#8), an unexpectedly high fluoride emission can be observed. Although Fe^{2+} only acts as a catalyst and is theoretically not necessary to produce $HO^{\bullet}$ radicals as shown in reaction 2, simulations of experiment #8 reveal that a fluoride concentration close to zero is expected after 72 h, as can be seen in figure 4b. This discrepancy might be explained by the presence of other metal impurities such as copper ions (Cu^{2+}) in the solution, which catalyze the Fenton reaction but are not implemented in the model [22, 23]. They may stem for example from the membrane manufacturing process or the feed water that may not be purified perfectly. Furthermore, it has been shown in the literature that Fe^{2+} may be replaced by other Fenton-like metal catalysts to produce $HO^{\bullet}$ radicals, including

titanium [24, 25]. Reactions between other metal impurities and H_2O_2 can be implemented similarly as done with Fe^{2+} in this work.

The impact of initial H_2O_2 concentration on fluoride emission at 1 ppm initial Fe^{2+} concentration can be seen in figure 3b. As for iron, the figure includes measurements after 23 h (blue) and 49 h (red). Besides the above mentioned zero-emission at the absence of H_2O_2, a dependency is visible. While low initial H_2O_2 concentration leads to low fluoride emission, the peak is reached between 0.03 and 30wt%, depending on the considered time-frame. This suggests the existence of an optimal concentration to prevent excessive membrane degradation outside these boundaries. Simulations have confirmed the theoretical existence of such an optimum and will be discussed later. However, intuitively an increase in fluoride emission with H_2O_2 concentration would be expected. A repetition of the set of experiments has to be carried out in order to finally conclude on the existence of an optimum and to rule out experimental errors. An ex-situ experiment was carried out in the literature to find the dependence of the fluoride emission on temperature at 0.36 mM Fe^{2+} ($\approx$ 20 ppm) and 9.68 M H_2O_2 ($\approx$33wt%) [15]. They found a concentration of roughly 0.38 ppm F^- after 9.5 h at 80 °C. The conditions are different from any of the here investigated ones, but come closest to experiment #7 with 30wt% H_2O_2 and 1 ppm Fe^{2+}, where the measured fluoride concentration was 0.35 ppm after 23 h.

4.1.1. Implications on the Membrane Attack Reaction

The model described above is utilized in order to simulate ex-situ behavior and adjusted by setting all in- and outflux to zero. Instead, the initial concentrations of Fe^{2+} and H_2O_2 are set according to the test as in table 2. Further-

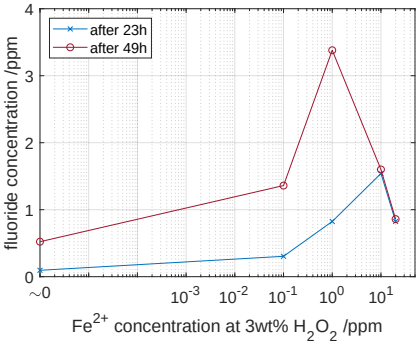

(a) Measured fluoride concentration as a function of initial Fe^{2+} concentration

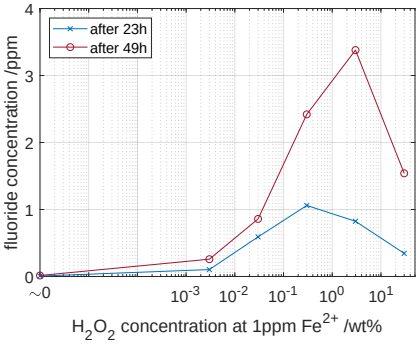

(b) Measured fluoride concentration as a function of initial H_2O_2 concentration

Figure 3: Influence of initial Fe_2^+ and H_2O_2 concentration according to table 2 on fluoride emission

more, the initial oxygen concentration was set according to Henry's law due to dilution from the air. The approach is shown for experiment #6 (BL) in figure 4a, while figure 4b compares the measured value to the simulation after 72 h for all tests.

Even though the model estimates correct trends according to the initial conditions, it can be seen that the modelling approach cannot fully capture the kinetics of the reaction. It underestimates fluoride emission with the exception of test #7, #10, and #11. The latter two are highly influenced by H_2O_2 limitation and are therefore excluded from further analysis, although H_2O_2 limitation itself is correctly simulated as a qualitative trend. Experiment #7 with 30wt-% H_2O_2 unexpectedly showed a lower fluoride emission compared to the tests with 3wt-% H_2O_2. As discussed before, this result has to be confirmed and will therefore be excluded for this analysis. Furthermore, experiments #1, #2, and #8 all have simulated emission close to zero and will not be used. Apart from these, the gathered data at 80 °C together with the reported value at 25 °C is utilized to implement k_{14} as a function of temperature to improve model predictions. For that it is assumed that reaction 14 follows the Arrhenius law. Fluoride emission from a polymer membrane has in fact previously been reported to be sensitive to temperature [15].

4.2. In-situ Fluoride Emission

The model inputs for in-situ FER simulations are oxygen crossover, which determines the equilibrium H_2O_2 concentration, and Fe^{2+} influx, which determines the equilibrium Fe^{2+} concentration. Equilibrium concentrations are a result of in- and outflux of species as described in equation IV and appear in an operational cell in steady state. To simulate the impact of both, a base-

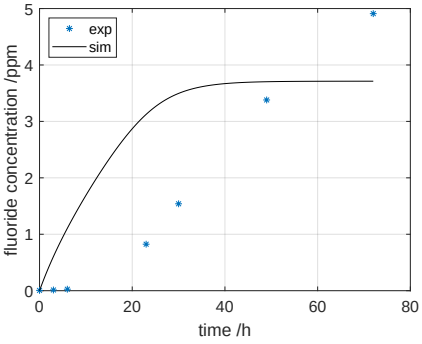

(a) Baseline case (experiment #6, 1 ppm Fe^{2+}/3wt-% H_2O_2)

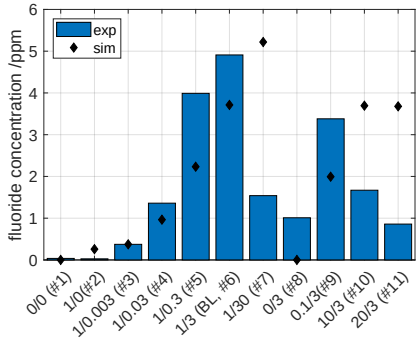

(b) Concentrations as experimentally determined (bars) compared to simulations (⧫) for all experiments. The labels refer to the initial concentrations as $[Fe^{2+}]/[H_2O_2]$, where BL = baseline test

Figure 4: Simulated and measured ex-situ fluoride concentration

line for O_2 crossover was set to $6 \cdot 10^{-5} \mathrm{mol\,m^{-2}\,s^{-1}}$, leading to around = $7.6 \cdot 10^{-3} M$ H_2O_2 equilibrium concentration. This is in fair agreement with the assumed constant background H_2O_2 concentration of = $5 \cdot 10^{-4} M$ in [9] when considering that this number will change according to the operation condition. The O_2 permeation rate was found in the literature as experimentally determined at $2.0\,\mathrm{A\,cm^{-2}}$ and 70 °C [26]. The baseline Fe^{2+} influx is set to $3.58 \cdot 10^{-7} \mathrm{mol\,m^{-2}\,s^{-1}}$ (= 1 ppm$\cdot s^{-1}$), leading to $2.6 \cdot 10^{-5} M$ (= 0.13 ppm) equilibrium concentration. The Fe^{2+} influx was chosen as a starting point and is slightly lower than what was found in a previous simulation work [12]. Setting an in- and outflux rather than a constant background concentration assumes that Fe^{2+} has a source term outside the MEA, which might be any stainless steel component in the cell assembly or balance of plant. Lastly, the baseline current was set to $2.0\,\mathrm{A\,cm^{-2}}$ and the temperature to 80 °C.

The model results show that oxygen is needed to produce H_2O_2, but does not play a vital role in the reaction system otherwise. H_2O_2 formation however is crucial, as it serves as a precursor for all other reactions. This is supported by the ex-situ experiment, where the two tests without H_2O_2 (#1 and #2) lead to a fluoride emission close to zero. The driving force for the membrane attack as in reaction 14 is the $HO^{\bullet}$ radical. Therefore, a lower concentration leads to a lower simulated FER as it can be seen in figure 5. The cause for a lower $HO^{\bullet}$ concentration at higher current can be found within reactions 3, 6, and 7, which are also shown in the figure. While reaction 3 is the dominant pathway for radical production, reactions 6 and 7 are its major sinks besides the attack reaction 14. It can be observed that the reaction rate of reaction 3 decreases with increasing current, whereas the rate for reaction 7 increases. Therefore,

the net-reaction rate for HO• production eventually becomes negative.

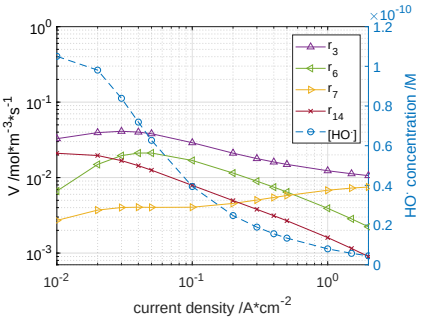

Figure 5: Simulated reaction rates for the most important reactions (left axis) and HO• concentration (right axis) as a function of current density

4.2.1. Impact of Reactants Influx and Concentrations

The Fe^{2+} influx highly affects the equilibrium concentrations and therefore FER. The simulated effects shown in figure 6a reveal that the equilibrium H_2O_2 concentration is not considerably affected over the majority of simulated range, while a non-linear relationship on equilibrium Fe^{2+} concentration and subsequently FER is visible. This is expected, as reaction 3 produces more HO• radicals at higher Fe^{2+} concentrations. At very high Fe^{2+} equilibrium concentrations due to a high influx, the FER is decreasing mostly due to a faster depletion of HO• radicals through reaction 5 as illustrated in figure 6b.

A sensitivity towards O_2 influx can be seen in figure 6c. The simulations reveal that an increase in O_2 influx leads to higher equilibrium concentrations for both O_2 and H_2O_2. Furthermore, it causes a decrease in FER when higher than around $6 \cdot 10^{-6} \mathrm{mol\,m^{-2}\,s^{-1}}$. The dependence lies within reaction 6 and 7,

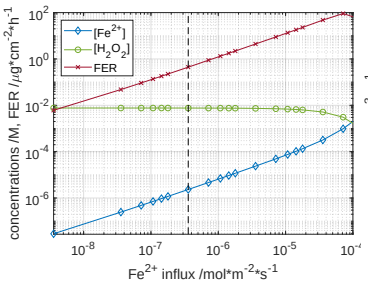

(a) Impact of the Fe^{2+} influx on equilibrium concentrations of Fe^{2+} (dark blue) and H_2O_2 (green), and FER (red)

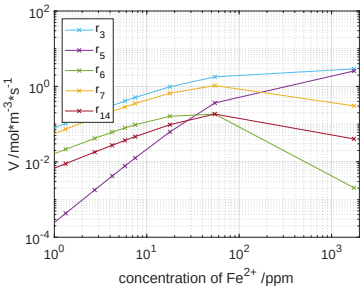

(b) Impact of Fe^{2+} equilibrium concentration on the most affected reactions

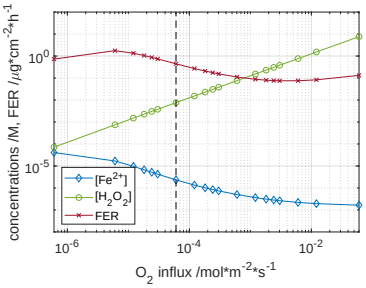

(c) Impact of the O_2 influx on equilibrium concentrations of Fe^{2+} (dark blue) and H_2O_2 (green), and FER (red)

Figure 6: Impact of Fe^{2+} and O_2 on the reaction system. For the other parameters, baseline case is assumed. The baseline influx of the investigated species is marked with the dashed line

which become dominant over reaction 14 at high H_2O_2 and O_2 concentrations and result in $HO^\bullet$ depletion as shown in figure 5). At the same time, reaction 9 accelerates slightly, leading to a reduction of Fe^{2+} ions without forming $HO^\bullet$ radicals.

Model Sensitivity Towards Reactive End-group Concentration

Unlike the other chemical species, reactive end-groups $-COOH$ do not participate in the reaction system to reach an equilibrium concentration, but are assumed to be constant in this work. As a result of a literature review, the end-group concentration is connected to uncertainty and together with $HO^\bullet$, it determines the membrane attack reaction rate. Therefore, the chosen value may affect the accuracy of the simulations and a sensitivity analysis is carried out. The sensitivity study assumed the baseline case. The results are shown in figure 7 and reveal that the FER is in fact changing. A drop of $-COOH$ concentration by one order of magnitude to 20 mM implies a reduction in FER to around one tenth, where an increase by one order of magnitude to 2000 mM roughly increases the FER by a factor of 6.5. Additionally, a higher $-COOH$ concentration amplifies the effect of current on FER. The simulation further reveals that an increase in $-COOH$ concentration shifts the Fe^{2+} equilibrium concentration up by 20%, which may be the cause for the increased FER. End-group concentration has been found to become very limiting on polymer attack below 100 mM under fuel cell conditions, but to remain within the same order of magnitude above [9].

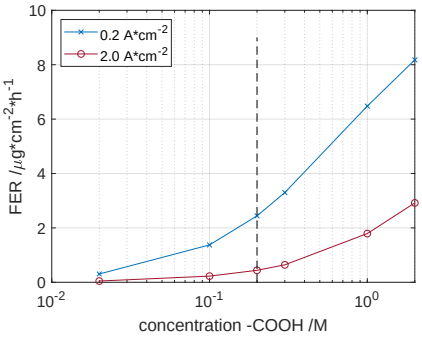

Figure 7: Impact of the concentration of reactive -COOH end-groups on Fe^{2+} concentration (blue) and FER (red). The value used for this work of 200 mM is marked with the dashed line

4.2.2. Simulation of a Single Cell and Comparison to in-situ Measurements

In order to simulate a cell in realistic operation, the oxygen influx was implemented as oxygen crossover through the membrane. For this work, the effect of current density on degradation is investigated. Oxygen crossover can be modelled as diffusion and convection [27], which was experimentally found to be insufficient to describe the behavior [26]. Instead, the oxygen flux at the cathode outlet was found to be a linear function of current density for PEM WE. Although this neglects any potential reactions within the cathode catalyst layer involving oxygen, the crossover is implemented as empirically determined in [26]. Since the experiment was only carried out at 70 °C, the temperature dependence is unknown and not implemented in this approach. The simulated oxygen crossover and FER as a function of current density and temperature can be seen in figure 8a, while the Fe^{2+} influx is set to the baseline case of $3.58 \cdot 10^{-7} \mathrm{mol\,m^{-2}\,s^{-1}}$. Additionally, in-situ measurements at $2.0\,\mathrm{A\,cm^{-2}}$

at 60, 80, and 90 °C are shown.

The simulation reveals that the FER seems to be a negative non-linear function of current density, where higher currents are favorable in terms of minimizing the FER in a real cell application. While running at 0.2 A cm^{-2} at 80 °C would lead to a FER of 3.30 µg cm^{-2} h^{-1}, operation at 2.0 A cm^{-2} lowers that to 0.64 µg cm^{-2} h^{-1}. Furthermore, lower temperatures are favorable since they reduce the FER. On the contrary, higher temperatures are generally favorable in terms of performance, which suggests the existence of an optimum operation point when weighing between efficiency and lifetime. However, the simulated effect of temperature is low, especially at increased current density.

The simulation data was compared to data from a previous work, in which FER were measured in-situ on a 25 cm^2 set-up at different operation conditions [28]. This experimental data suggested a much bigger dependence of FER on temperature compared to the simulations as it can be seen from the filled diamonds in the respective colors at 0.3 A cm^{-2} in figure 8a. The difference in magnitude for all temperatures may be a result of a different Fe^{2+} concentration in a real cell, which is set to the baseline case for the simulation and shown to have a significant impact on FER in figure 6a.

The less pronounced temperature dependence in the experimental data on the other hand can be explained by the model implementation. While the membrane attack (reaction 14) was fitted to the ex-situ results, the oxygen crossover is not implemented as a function of temperature due to the lack of available data. A more sophisticated oxygen generation and transportation throughout the cell has to be implemented in order to compare different operation scenarios. Additionally, the iron influx may be a function of temperature

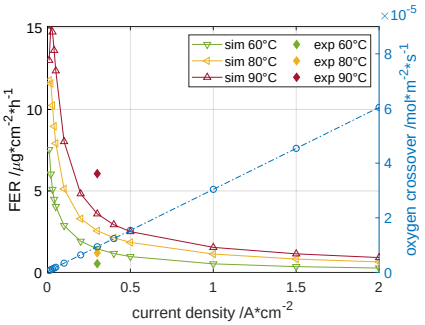

(a) Simulated oxygen crossover from anode to cathode (blue, left axis) and FER at different temperatures (right axis) as a function of current. Additionally, experimental FER at $0.3\,\mathrm{A\,cm^{-2}}$ are shown

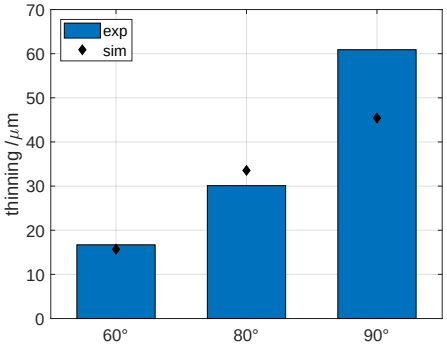

(b) Membrane thinning as determined from SEM images (bars) compared to simulations (♦)

Figure 8: Comparison of simulations to experimental data from in-situ cells

if assuming corrosion of balance of plant components as a source. Both factors may increase the FER at elevated temperatures. For the sake of completeness, the experimental in-situ data was fitted to the Arrhenius equation, which resulted in 79 kJ mol^{-1} and $4.04 \cdot 10^{18}$ for activation energy and frequency factor for reaction 14, respectively. The activation energy for membrane degradation reaction has previously been reported as around 70 kJ mol^{-1} [9].

4.2.3. Simulated Membrane Thinning Through Fluoride Emission

Membrane thinning was evaluated experimentally in a previous work by means of scanning electron microscopy (SEM) after 500 h for several operation conditions [28]. The values for three temperatures together with the respective simulated thinning according to equation IX is presented in figure 8b. The model fitting factor, $f_{F,loss}$ was set to 20.8 [12] for all simulations. The factor takes into account, that not all fluoride ions are captured in the outlet effluent water. It furthermore accounts for fluorine loss within polymer fragments that cannot be detected by an ion-selective electrode as used in this experimental approach. As a rough estimation, fluorine emission was found up to 6 times higher compared to fluoride [20].

The simulation shows fairly good fit at 60 °C and 80 °C with an error of 6% and 11%, but underestimates thinning at 90 °C by 25%. Given the uncertainties throughout the several assumptions made, these numbers are considered acceptable as a first evaluation of the effect of the operation mode on membrane degradation. Due to the underestimation of fluoride emission at 90 °C, the thinning is also underestimated. As a result, the fitting factor $f_{F,loss}$ could be empirically adjusted to the measured dataset.

5. Conclusion

The influence of hydrogen peroxide and iron ions on fluoride emission have been investigated in ex-situ and in-situ experiments, and through a computational model. The results show that hydrogen peroxide acts as a required precursor, while iron catalyzes the reaction considerably. However, even in the absence of iron, a considerable amount of fluoride emission is observed when H_2O_2 is present. This is linked to the ability of other metallic impurities to replace iron as a catalyzer of the reaction. However, the origin, magnitude, and location of metal impurities have to be identified.

A model based on a system of 14 reactions was developed to simulate ex-situ and in-situ environments. Temperatures above 80 °C as well as low current operation is highly unfavorable in terms of membrane degradation, as the fluoride emission increases non-linearly for both. Furthermore, the simulation revealed high dependence of fluoride emission on reactive end-group concentration, which is a parameter of high uncertainty. Considering the high amount of uncertainties among the developed model, the results are satisfactory for the in-situ simulations for temperatures up to 80 °C when compared to experimental data, but underestimate the effect of temperature above that. This is due to the lack of data for the temperature dependence of oxygen permeation.

Acknowledgement

The authors would like to acknowledge the support by Innovation Fund Denmark through the e-STORE project, Grant 4106-00025B.

References

[1] P. Trinke, B. Bensmann, S. Reichstein, R. Hanke-Rauschenbach, K. Sundmacher, Hydrogen Permeation in PEM Electrolyzer Cells Operated at Asymmetric Pressure Conditions, Journal of The Electrochemical Society 163 (11) (2016) F3164–F3170. doi:10.1149/2.0221611jes.
URL http://jes.ecsdl.org/lookup/doi/10.1149/2.0221611jes

[2] Q. Feng, X. Yuan, G. Liu, B. Wei, Z. Zhang, H. Li, H. Wang, A review of proton exchange membrane water electrolysis on degradation mechanisms and mitigation strategies, Journal of Power Sources 366 (2017) 33–55. doi:10.1016/j.jpowsour.2017.09.006.
URL http://dx.doi.org/10.1016/j.jpowsour.2017.09.006

[3] P. S. Ruvinskiy, A. Bonnefont, C. Pham-Huu, E. R. Savinova, Using ordered carbon nanomaterials for shedding light on the mechanism of the cathodic oxygen reduction reaction, Langmuir 27 (14) (2011) 9018–9027. doi:10.1021/la2006343.

[4] K. Barbusinski, Fenton reaction - Controversy concerning the chemistry, Ecological chemistry and engineering S/Chemia i in{·}zynieria ekologiczna S 16 (3) (2009) 347–358.

[5] A. Pozio, R. F. Silva, M. De Francesco, L. Giorgi, Nafion degradation in PEFCs from end plate iron contamination, Electrochimica Acta 48 (11) (2003) 1543–1549. doi:10.1016/S0013-4686(03)00026-4.

[6] R. Borup, J. Meyers, B. Pivovar, Y. S. Kim, R. Mukundan, N. Garland, D. Myers, M. Wilson, F. Garzon, D. Wood, P. Zelenay, K. More, K. Stroh,

T. Zawodzinski, X. J. Boncella, J. E. Mcgrath, O. M. Inaba, K. Miyatake, M. Hori, K. Ota, Z. Ogumi, S. Miyata, A. Nishikata, Z. Siroma, Y. Uchimoto, K. Yasuda, K.-i. Kimijima, N. Iwashita, Scientific Aspects of Polymer Electrolyte Fuel Cell Durability and Degradation, Chemical Reviews (2007) 3904–3951.

[7] V. O. Mittal, H. Russell Kunz, J. M. Fenton, Is H[sub 2]O[sub 2] Involved in the Membrane Degradation Mechanism in PEMFC?, Electrochemical and Solid-State Letters 9 (6) (2006) A299. doi:10.1149/1.2192696.
URL http://esl.ecsdl.org/cgi/doi/10.1149/1.2192696

[8] A. A. Shah, T. R. Ralph, F. C. Walsh, Modeling and Simulation of the Degradation of Perfluorinated Ion-Exchange Membranes in PEM Fuel Cells, Journal of The Electrochemical Society 156 (4) (2009) B465. doi:10.1149/1.3077573.
URL http://jes.ecsdl.org/cgi/doi/10.1149/1.3077573

[9] L. Gubler, S. M. Dockheer, W. H. Koppenol, Radical (HO, H and HOO) Formation and Ionomer Degradation in Polymer Electrolyte Fuel Cells, Journal of The Electrochemical Society 158 (7) (2011) B755. doi:10.1149/1.3581040.
URL http://jes.ecsdl.org/cgi/doi/10.1149/1.3581040

[10] M. Ghelichi, P. E. A. Melchy, M. H. Eikerling, Radically coarse-grained approach to the modeling of chemical degradation in fuel cell ionomers, Journal of Physical Chemistry B 118 (38) (2014) 11375–11386. doi:10.1021/jp506333p.

[11] M. Chandesris, R. Vincent, L. Guetaz, J.-S. Roch, D. Thoby, M. Quinaud, Membrane degradation in PEM fuel cells: From experimental results to semi-empirical degradation laws, International Journal of Hydrogen Energy 42 (12) (2017) 8139–8149. doi:10.1016/j.ijhydene.2017.02.116.
URL http://linkinghub.elsevier.com/retrieve/pii/S0360319917306249

[12] M. Chandesris, V. Médeau, N. Guillet, S. Chelghoum, D. Thoby, F. Fouda-Onana, Membrane degradation in PEM water electrolyzer: Numerical modeling and experimental evidence of the influence of temperature and current density, International Journal of Hydrogen Energy 40 (3) (2015) 1353–1366. doi:10.1016/j.ijhydene.2014.11.111.

[13] H. Liu, F. D. Coms, J. Zhang, H. A. Gasteiger, A. B. Laconti, Chemical degradation: Correlations between electrolyzer and fuel cell findings, in: Polymer Electrolyte Fuel Cell Durability, Springer, 2009, pp. 71–118. doi:10.1007/978-0-387-85536-3_5.

[14] F. Fouda-Onana, M. Chandesris, V. Médeau, S. Chelghoum, D. Thoby, N. Guillet, Investigation on the degradation of MEAs for PEM water electrolysers part I: Effects of testing conditions on MEA performances and membrane properties, International Journal of Hydrogen Energy 41 (2016) 16627–16636. doi:10.1016/j.ijhydene.2016.07.125.

[15] T. Sugawara, N. Kawashima, T. N. Murakami, Kinetic study of Nafion degradation by Fenton reaction, Journal of Power Sources 196 (5) (2011) 2615–2620. doi:10.1016/j.jpowsour.2010.10.043.
URL http://dx.doi.org/10.1016/j.jpowsour.2010.10.043

[16] V. A. Sethuraman, J. W. Weidner, A. T. Haug, S. Motupally, L. V. Protsailo, Hydrogen Peroxide Formation Rates in a PEMFC Anode and Cathode, Journal of The Electrochemical Society 155 (1) (2008) B50. doi:10.1149/1.2801980.
URL http://jes.ecsdl.org/cgi/doi/10.1149/1.2801980

[17] K. H. Wong, E. Kjeang, Macroscopic In-Situ Modeling of Chemical Membrane Degradation in Polymer Electrolyte Fuel Cells, Journal of the Electrochemical Society 161 (9) (2014) F823–F832. doi:10.1149/2.0031409jes.
URL http://jes.ecsdl.org/cgi/doi/10.1149/2.0031409jes

[18] T. Xie, C. A. Hayden, A kinetic model for the chemical degradation of perfluorinated sulfonic acid ionomers: Weak end groups versus side chain cleavage, Polymer 48 (19) (2007) 5497–5506. doi:10.1016/j.polymer.2007.07.043.
URL http://dx.doi.org/10.1016/j.polymer.2007.07.043

[19] C. Zhou, M. A. Guerra, Z. M. Qiu, T. A. Zawodzinski, D. A. Schiraldi, Chemical durability studies of perfluorinated sulfonic acid polymers and model compounds under mimic fuel cell conditions, Macromolecules 40 (24) (2007) 8695–8707. doi:10.1021/ma071603z.

[20] M. Bodner, B. Marius, A. Schenk, V. Hacker, Determining the Total Fluorine Emission Rate in Polymer Electrolyte Fuel Cell Effluent Water, ECS Transactions 80 (8) (2017) 559–563.

[21] F. M. Collette, C. Lorentz, G. Gebel, F. Thominette, Hygrothermal ag-

ing of Nafion®, Journal of Membrane Science 330 (1-2) (2009) 21–29. doi:10.1016/j.memsci.2008.11.048.

[22] A. B. LaConti, M. Hamdan, R. C. McDonald, Mechanisms of membrane degradation, in: Handbook of Fuel Cells: Fundamentals, Technology, and Applications, John Wiley and Sons, 2003, pp. 647–663.

[23] M. Inaba, Degradation Mechanism of Polymer Electrolyte Fuel Cells, 14th International Conference on the Properties of Water and Steam in Kyoto (2004) 395–402.

[24] S. GOLDSTEIN, D. MEYERSTEIN, G. CZAPSKI, THE FENTON REAGENTS, Free Radical Biology & Medicine 15 (Ii) (1993) 435–445.

[25] Z. Liu, T. Wang, X. Yu, Z. Geng, Y. Sang, H. Liu, In situ alternative switching between Ti ⁴⁺ and Ti ³⁺ driven by H ₂ O ₂ in TiO ₂ nanostructures: mechanism of pseudo-Fenton reaction, Materials Chemistry Frontiers 1 (10) (2017) 1989–1994. doi:10.1039/C7QM00163K.
URL http://xlink.rsc.org/?DOI=C7QM00163K

[26] P. Trinke, B. Bensmann, R. Hanke-Rauschenbach, Experimental evidence of increasing oxygen crossover with increasing current density during PEM water electrolysis, Electrochemistry Communications 82 (June) (2017) 98–102. doi:10.1016/j.elecom.2017.07.018.
URL http://dx.doi.org/10.1016/j.elecom.2017.07.018

[27] P. Olivier, C. Bourasseau, P. B. Bouamama, Low-temperature electrolysis

system modelling: A review, Renewable and Sustainable Energy Reviews 78 (March) (2017) 280–300. doi:10.1016/j.rser.2017.03.099.

[28] S. H. Frensch, F. Fouda-Onana, G. Serre, D. Thoby, S. S. Araya, S. K. Kær, Influence of the Operation Mode on PEM Water Electrolysis Degradation. Manuscript submitted for publication (2018).

ISSN (online): 2446-1636
ISBN (online): 978-87-7210-354-9

AALBORG UNIVERSITY PRESS